ΕΛΛΗΝΙΚΗ ΔΗΜΟΚΡΑΤΙΑ
ΠΑΝΕΠΙΣΤΗΜΙΟ ΙΩΑΝΝΙΝΩΝ
ΠΟΛΥΤΕΧΝΙΚΗ ΣΧΟΛΗ
ΤΜΗΜΑ ΜΗΧΑΝΙΚΩΝ ΕΠΙΣΤΗΜΗΣ ΥΛΙΚΩΝ
ΠΡΟΓΡΑΜΜΑ ΜΕΤΑΠΤΥΧΙΑΚΩΝ ΣΠΟΥΔΩΝ
«ΠΡΟΗΓΜΕΝΑ ΥΛΙΚΑ»

ΜΕΤΑΠΤΥΧΙΑΚΗ ΔΙΑΤΡΙΒΗ

ΑΜΑΛΙΑ ΝΤΕΜΟΥ

ΜΟΝΤΕΛΟΠΟΙΗΣΗ ΛΕΙΤΟΥΡΓΙΚΩΝ ΔΙΕΡΓΑΣΙΩΝ ΤΟΥ ΕΓΚΕΦΑΛΙΚΟΥ ΙΣΤΟΥ

ΙΩΑΝΝΙΝΑ, 2018

Εσώφυλλο:

Η παρούσα Μεταπτυχιακή Διατριβή εκπονήθηκε στο πλαίσιο των σπουδών για την απόκτηση του Μεταπτυχιακού Διπλώματος Ειδίκευσης στην εξειδίκευση:

Βϊουλικά και βιοϊατρική τεχνολογία

που απονέμει το Τμήμα Μηχανικών Επιστήμης Υλικών του Πανεπιστημίου Ιωαννίνων.

Εγκρίθηκε την ……..από την εξεταστική επιτροπή:

ΟΝΟΜΑΤΕΠΩΝΥΜΟ	**ΒΑΘΜΙΔΑ**
1. Δημήτριος Φωτιάδης, Επιβλέπων	Καθηγητής του ΤΜΕΥ της Πολυτεχνικής Σχολής του Παν/μίου Ιωαννίνων.
2. Λεωνίδας Γεργίδης	Επίκουρος Καθηγητής του ΤΜΕΥ της Πολυτεχνικής Σχολής του Παν/μίου Ιωαννίνων.
3. Μαρία Αργυροπούλου	Καθηγήτρια Ακτινολογίας της Ιατρικής Σχολής του Παν/μίου Ιωαννίνων.

ΥΠΕΥΘΥΝΗ ΔΗΛΩΣΗ

"Δηλώνω υπεύθυνα ότι η παρούσα διατριβή εκπονήθηκε κάτω από τους διεθνείς ηθικούς και ακαδημαϊκούς κανόνες δεοντολογίας και προστασίας της πνευματικής ιδιοκτησίας. Σύμφωνα με τους κανόνες αυτούς, δεν έχω προβεί σε ιδιοποίηση ξένου επιστημονικού έργου και έχω πλήρως αναφέρει τις πηγές που χρησιμοποίησα στην εργασία αυτή."
(Υπογραφή υποψηφίου)

Περίληψη

Η παρούσα μεταπτυχιακή διπλωματική εργασία παρουσιάζει μια αναλυτική προσέγγιση την συνεκτικότητας των εγκεφαλικών περιοχών, χρησιμοποιώντας δεδομένα λειτουργικής μαγνητικής τομογραφίας ασθενών με σύνδρομο ανήσυχων ποδιών, μια νευρολογική διαταραχή που προσβάλει σημαντικό ποσοστό του πληθυσμού παγκοσμίως.

Εξετάζοντας προηγούμενες μελέτες για τη περιγραφή του συνδρόμου ανήσυχων ποδιών με τη χρήση fMRI παρατηρήθηκε ότι οι μελέτες περιορίζονται σε συγκεκριμένες υπολογιστικές μεθόδους, γεγονός που πιθανά περιορίζει την παροχή απαντήσεων σε ερωτήματα που σχετίζονται με την πάθηση. Πραγματοποιήθηκε μια αναλυτική περιγραφή των τύπων της εγκεφαλικής συνεκτικότητας και των μεθόδων εξαγωγής της με σκοπό τη μοντελοποίηση του εγκεφαλικού ιστού.

Στο πρώτο κεφάλαιο της παρούσας διατριβής, γίνεται αναφορά στις διαταραχές ύπνου, την κατηγοροποίηση τους ανάλογα με τα χαρακτηριστικά τους και την επίδραση τους στην υγεία και την ποιότητα ζωής των ασθενών. Στη συνέχεια περιγράφονται αναλυτικά για την υπό μελέτη διαταραχή ύπνου, το σύνδρομο ανήσυχων ποδιών, στοιχεία επιδημιολογίας, παθοφυσιολογίας, διάγνωσης και θεραπείας, καθώς και κριτήρια κλινικής εμφάνισης.

Στο επόμενο κεφάλαιο περιγράφονται οι αρχές λειτουργίας της ευρέως διαδεδομένης διαγνωστικής μεθόδου fMRI κάνοντας αναφορά στην αντίδραση BOLD, τους τύπους πειραματικού σχεδιασμού, την λήψη εκόνων, τις χρονοσειρές fMRI, τις κλινικές εφαρμογές καθώς επίσης και τα πλεονεκτήματα και τα μειονεκτήματα της μεθόδου.

Στη συνέχεια γίνεται μια αναλυτική περιγραφή πρόσφατων απεικονιστικών μεθόδων σχετικά με το συγκεκριμένο σύνδρομο, παραθέτοντας τις μεθόδους και τα ευρήματα που προέκυψαν. Περιγράφονται μελέτες που χρησιμοποίησαν PET, SPECT, δομικό MRI, ηλεκτροεγκεφαλογράφημα, λειτουργικό MRI κ.α.. Οι περισσότερες μελέτες που περιγράφονται χρησιμοποιούν λειτουργικό MRI σε κατάσταση ηρεμίας έχοντας ως στόχο να συγκριθούν με την παρούσα μελέτη.

Στο τέταρτο κεφάλαιο πραγματοποιείται μια εκτενής παρουσίαση των τριών τύπων της εγκεφαλικής συνεκτικότητας (δομικής, λειτουργικής και αιτιώδους), καθώς επίσης και των μεθόδων που προτείνονται για την ανάλυση τους.

Το πέμπτο κεφάλαιο περιλαμβάνει τα αποτελέσματα του πειραματικού μέρους της παρούσας διπλωματικής εργασίας. Συγκεκριμένα παρουσιάζονται και αναλύονται τα αποτελέσματα από την επικύρωση της προτεινόμενης μεθοδολογίας ακολουθώντας διαφορετικές προσεγγίσεις από τις ήδη υπάρχουσες μελέτες αναδεικνύοντας έτσι την καινοτομία της εργασίας.

Το έκτο κεφάλαιο αποτελεί συζήτηση στα αποτελέσματα των μεθοδολογιών που ακολουθήθηκαν, καταγράφονται τα συμπεράσματα και προτείνονται κατευθύνσεις για μελλοντική έρευνα.

HELLENIC REBUBLIC

UNIVERSITY OF IOANNINA

TECHNICAL SCHOOL

DEPARTMENT OF MATERIALS SCIENCE AND ENGINEERING

MASTER OF SCIENCE

«ADVANCED MATERIALS»

MSc THESIS

AMALIA NTEMOU

MODELLING FUNCTIONAL PROCESSES OF BRAIN TISSUE

IOANNINA, 2018

Dedication

To my family

Abstract

The current master thesis presents a detailed study of Brain Connectivity with the use of functional Magnetic Resonance Imaging (fMRI) data for the Restless Legs Syndrome (RLS), a neurological sleep disorder which affects a large number of people worldwide.

After studying prior literature recordings regarding brain connectivity analysis of RLS, relying on fMRI, it was observed that these studies are constrained to certain computation methods, a fact which possibly leads to limited inferences concerning the disease. An analytical description of brain connectivity types and their extraction methods are presented aiming to the modeling of the brain tissue.

In the first chapter of the current thesis, the sleep disorders and their classification are described, depending on their special characteristics and their effect on subjects' health and quality of life. A detailed description regarding the sleep disorder phenomenon is presented, including epidemiological and pathophysiological elements, diagnostic and treatment criteria as well as the clinical presentation of the disease.

The next chapter involves the operation principles of the popular diagnostic method fMRI, reporting the BOLD mechanism, the types of experimental design, the image acquisition, the fMRI time-series, the clinical applications as well as its advantages and disadvantages.

A state-of-the-art analysis on imaging methods for RLS was conducted and methodologies and results of various studies are presented in the next chapter. They include PET, SPECT, structural MRI, EEG and resting state fMRI, focusing on the conclusions of the latter because of the need for their comparison with our current study findings.

In the fourth chapter an extensive presentation of the tree types of brain connectivity (structural, functional and effective connectivity) is given, in parallel with the proposed methods for their analysis.

The fifth chapter includes the results of the experimental part of the current thesis. In particular, the results coming from the establishment of the proposed methodology are presented and analyzed, following alternative approaches compared to the existing studies to emphasize the novelty of our work.

The sixth chapter includes further discussion and conclusions on the results of the methodology followed and new trends are proposed for further future investigation.

List of Abbreviations

Acronym	*Meaning*
REM	Rapid Eye Movement
EoG	Electro-oculographic
EEG	Electro-encephalogram
PLM	Periodic Limb Movement
RLS	Restless Legs Syndrome
PLMD	Periodic Limb Movement Disorder
EMG	Electromyography
ENG	Electroneuronography
IRLSSG	Restless Legs Syndrome Study Group
NIH	National Institute of Health
MEG	Magnetoencephalography
fMRI	functional Magnetic Resonance Imaging
PET	Positron Emission Tomography
BOLD	Blood Oxygen Level Dependent
EPI	Echo Planar Imaging
CBF	Cerebral Blood Flow
CBV	Cerebral Brain Volume
HDR	Hemodynamic response
ERPs	Event-related potentials
VBM	Voxel-based morphometry
MRS	Magnetic Resonance Spectroscopy
QSM	Quantitative Susceptibility Mapping

ANOVA	Analysis of variance
GLM	General Linear Model
SPM	Statistical Parametric Mapping
rTMS	repetitive Transcranial Magnetic Stimulation
ALFF	Amplitute of low-frequency fluctuations
DTI	Diffusion Tensor Imaging
ReHo	Regional homogeneity
MNI	Montreal Neurological Institute
FWHM	full width half maximum
DICOM	Digital Imaging and Communications in Medicine
CCA	Cross-correlation analysis
PCA	Principal Component Analysis
SVD	Singular Value Decomposition
ICA	Independent Component Analysis
FCA	Fuzzy Clustering Analysis
HCA	Hierarchical Clustering Analysis
FPR	False Positive Rate
DCM	Dynamic Causal Modeling
SEM	Structural Equation Modeling
PPI	Psychophysiological interactions
BA	Brodmann area
ROI	Region of interest
WM	White matter
GM	Gray matter

Table of Contents

List of Figures

List of Tables

Chapter 1. Introduction

1.1 Sleep disorders

In 1953, a study conducted by Nathaniel Kleitman and Eugene Aserinsky which concerned the eyelid movement during sleep, led to the discovery of REM (rapid eye movement) sleep, a unique stage of sleep [1]. REM sleep and Non-REM sleep are two different stages during sleep, which present differences with regards to the findings of electro-oculographic (EoG) and electro-encephalogram (EEG). The discovery of the similarities the brain presented during awake state and REM sleep are amazingly interesting. The characteristics of REM sleep state are associated with side-to-side movement of the closed eyes and the brain neurons are highly active as in the case of dreaming vividly. This stage of sleep results in short range and high frequency waves in EEG. Its duration lasts 90-110 min and the non-REM stages about 3 to 6 times during the night.

Most brain regions are active during the three phases, that is the state of vigilance, REM state and non-REM state. Sleep studies on animals were really supportive

regarding the understanding of the human brain allowing for in depth knowledge regarding diagnosis and treatment. Furthermore, the findings from sleep studies performed in humans led to important conclusions about sleep and its disorders [1, 2].

Officially, there are about a hundred recognized sleep disorders. Most of them are categorized into insomnias, sleep-related breathing disorders, hypersomnias of central origin, circadian rhythm sleep disorders, parasomnias and sleep related movement disorders.

Insomnia is characterized by difficulty initiating or maintaining sleep and contains large periods of nocturnal wakefulness and/or insufficient amount of nocturnal sleep. To fully examine insomnia, further criteria apart from initiating, maintaining sleep, waking too early and sleep of poor quality is needed, as the feeling of sleepiness arises from sleep difficulty at night, although there are suitable conditions to allow sleep. According to the diagnostic criteria that have arisen, insomnias can be categorized as primary insomnia, insomnia due to a mental disorder, psychophysiological insomnia, paradoxical insomnia, idiopathic insomnia, insomnia related to periodic limb movement disorder, insomnia related to sleep apnea, insomnia due to a medical condition and insomnia due to drugs or substances. There are two main types of insomnia, the primary and secondary.

The cause of primary insomnia includes both intrinsic and extrinsic factors. The secondary type of insomnia contains symptoms related to a medical or psychiatric illness, another sleep disorder or substance abuse [3].

The main characteristic of sleep-related breathing disorders includes in sufficient ventilation during sleep. There are central apnea syndromes that cause limitation in respiratory process or absence in an interrupted or cyclical way (which is reflected from the dysfunction of central nervous system) or others which are related to underlying pathologic or environmental causes, such as Cheyne-Stokes breathing pattern and high altitude periodic breathing. The first form of the primary central sleep apnea disorder, is not due to a specific cause and its feature is repeated episodes of absent breathing during sleep. The second form known as secondary central sleep apnea occurs due to drug or substances. In the case of an airway obstruction causing difficulty in the breathing process and inadequate ventilation, the syndrome is characterized as obstructive sleep apnea. The features concerning this disorder are often associated with reduced blood oxygen saturation. Hypoventilation or hypoxemia are also characteristics of disordered sleep which include five more disorders. Sleep-related

nonobstructive alveolar hypoventilation, idiopathic, refers to reduced dental hypoventilation which in turn causes sleep-related arterial oxygen desaturation in patients with normal mechanical lung function.

When it comes to hypersomnia disorders we refer to daytime sleepiness, which provoke unwanted lapses into sleep without primary disturbance in nocturnal sleep or circadian rhythms. Relevant syndromes that are included in this category are also the following: narcolepsy, recurrent hypersomnia (Kleine-Levin Syndrome and menstrual-related hypersomnia), idiopathic hypersomnia with long sleep time, behavioral-included insufficient sleep syndrome and hypersomnia due to a medical condition.

A persistent or recurrent misalignment between the patient's sleep pattern and the pattern that is desired or regarded as the societal norm and is the main feature of the circadian rhythm sleep disorders. The problem that emerges from these disorders is that the patient's sleep cannot be achieved in an appropriate or certain time. The requirement needed so as for a patient to be diagnosed with circadian rhythm sleep disorder, is whether the main cause of sleep is specific sleep period or if it is not related to societal norm.

Parasomnias are disrupted sleep disorders that may occur during arousals from REM sleep or partial arousals from non-REM sleep. The parasomnias include abnormal sleep-related movements, behaviors, emotions, perceptions, dreaming and autonomic nervous system functioning. Furthermore, this type of sleep disorder includes sleep-related dissociative disorders, sleep-related hallucinations as well as sleep-related eating disorders.

Periodic limb movements (PLM) and restless legs syndrome (RLS) are also abnormal reactions associated with sleep-related movement disorders and feature simple, stereotyped movements that disrupt sleep and they are presented in detail below [3].

The Diagnostic and Statistical Manual of Mental Disorders, the International Classification of Sleep Disorders and the International Statistical Classification of Diseases and Related Health Problems are systems which aim to put sleep disorders into specific categories. The identification of sleep disorder is accomplished by having the patient and his/her partner write down their experiences as well as the poly-nystagmography (PSG) and actigraphy findings.

Over 40% of people worldwide, have experienced abnormal movement behavior during sleep that leads to lessened sleep duration and increased sleepiness during

daytime. Consequently, both physical and mental health are afflicted resulting in social and economic effects in addition to poor quality of life [2].

1.2 Restless Legs Syndrome (RLS)

This study attempts to approach RLS which was first reported in the seventeenth century by the English physician and anatomist Sir Thomas Willis [4]. This is why RLS is usually referred as Willis-Ekbom disease [5]. Despite the fact that the symptoms that are associated with RLS were identified by Boissier de Sauvages, Magnus Huss and Gilles de la Tourette in 1763, 1849 and 1898 respectively, the Swedish neurologist Karl Axel Ekbom in 1945 first introduced the notion of 'Restless Legs Syndrome' with its clinical and epidemiological features. Fifty years later, the diagnostic criteria of the disease were clarified by the International Restless Legs Syndrome Study Group (with updated notes in 2003) [4].

Plethora of knowledge regarding the pathophysiology of this disease while on the other hand little is known about its neuroanatomic basis [6, 7].

1.2.1 Epidemiology of RLS

Through current epidemiologic analysis which was conducted in different countries all over the world, it has been deduced that the prevalence rate of the general population varies between 3.9% and 15%. This element should not be considered as a standard since these numbers indicatively differ among Caucasians and Asian populations. The numbers range between 7-10% in the former and are obviously lower 0.1-12% in the latter. RLS symptoms of greater frequency are usually more evident in western countries. Research has revealed that 10% of the population of United States is affected by RLS, 10-15% in Canada and Europe 5.5%, in comparison to the Indian, Japanese or Chinese population which is 2.9%, 0.96% and 1.4%, respectively. The genetic background, ethnicity, geography that differ across the various ethnic populations as well as their natural environment and dietary are the main reason for the existence of these variations [8].

Neurodegenerative process is known to play a crucial role in the disease occurrence and the severity of RLS, that is, its frequency and severity are higher in older ages and this is why RLS is considered to be a neurologic disease. Forty to fifty year age group are the most common ages that RLS symptoms become present, but there is a significant percentage (38-45% of patients) that experience symptoms before the age of 20. Furthermore, hormones such as estrogen and progesterone favor the RLS presence,

which shows that it affects more women than men and it is very frequent during pregnancy [4, 8, 9].

1.2.2 Clinical presentations and diagnostic criteria

RLS is characterized by four substantial criteria which are common in all patients. These are the irresistible urge to move legs or sometimes also arms, the needed movement in order to reduce sensations, the appearance of symptoms in evening or night hours primarily when resting, sitting, or sleeping and last the imbalance of circadian rhythm [9, 10]. The following descriptions concern personal perception of patients and they include "creeping, crawling tingling, tingling, pulling or pain" deep inside the limbs, involving one or both knees, ankles or even the whole lower limbs. Insomnia affects patients in their daily and their Health-Related Quality of Life (HRQoL) which ranges depending on the different degree and severity of symptoms [8].

It is necessary to mention the high circadian rhythm that appears in the sensory and motor symptoms in RLS which are highest at night. It has been shown that increased melatonin possibly influences the symptoms because of its impact in dopamine secretion in the central nervous system. An intex that relates to circadian rhythm, the core body temperature and shows variations in the intensity of RLS symptoms. When core body temperature is falling the symptoms are increased and vice versa.

Similar symptom features can be observed in Periodic Limb Movement Disorder (PLMD) a usual occurrence that affects the 80% of RLS patients. The opposite phenomenon does not necessarily occur, that is PLM patients do not experience necessarily RLS. The PLMD involves unwanted movements of limbs or torso in waking or sleeping state that patients ignore and are not the same as in RLS when patients provoke their movement in order to ease themselves. The PLMD was primarily named as nocturnal myoclonus and supportive diagnostic tools as PSG, actigraphy or electromyography (EMG) indicate muscle spasm which occurs continuously with a duration of 0.5-10s which is repeated every 5-90s provoking regular awaking which can affect sleep. In order to estimate PLMs during wakefulness immobilization tests are suggested which require the patients to remain completely still. The severity of RLS, the follow up period of the patient and the monitor treatment response can be evaluated with the use of PSG which records the time of the immobilization of the patient and the limb movements within an hour [8, 10].

The investigation concerning RLS provided diagnostic criteria that were established by National Institute of Health (NIH) and International Restless Legs Syndrome Study Group (IRLSSG) fifteen years ago. This research shed light on the main characteristic of RLS, which is the uncomfortable feeling in legs that leads to the urge to move them, while presenting exacerbation when the subject is at rest or generally when they are less active during the evening or night hours. Walking or stretching are beneficial factors which lessen symptoms. Later research, which was based on a large number of worldwide RLS clinicals using interdisciplinary, international and evidence-based approach for the disease, stresses that discrimination of RLS symptoms with other diseases as myalgia, venous stasis or leg edema is required. This renewed and accurate approximation of RLS also includes the great contribution of specifiers for clinical significance in the syndrome. They are able to recognize and record the functional consequences that RLS carries such as social, behavioral, educational or occupational. They can categorize the clinical course of patients and their clinical significance giving important feedback to physicians a fact that supports the illumination of RLS. However, the subjective character of these criteria disturbs their reliability. For this reason, the need for further diagnosis and classification of RLS is necessary. Indicatively, it could be achieved with biological markers, genetic characteristics, PLMs estimating, PSG or actigraphy changes [8, 11]. The following table (Table 1.1) includes all essential diagnostic criteria that have to be met so that RLS is accurately diagnosed and confirmed.

Table 1.1: The diagnostic criteria of 2012 revised version of IRLSSG [8, 11].

1	The need to move the limbs, mainly the legs, without the existence of upsetting feelings.
2	The need to move the legs as a result of uncomfortable feelings occurring during resting state.
3	The need to move the legs during the episode, in order to reduce symptoms by walking or stretching.
4	The need to move the legs during evening or night hours, rather than daytime, when being in a resting state.
5	The existence of these symptoms should not be the result of other medical or behavioral conditions (e.g. myalgia, venous stasis, leg edema, arthritis, leg cramps, positional discomfort, habitual foot tapping).

There are two basic RLS discriminations concerning its cause and these are the primary and secondary RLS. The first one refers to idiopathic syndrome that does not indicate the cause. It is worth emphasizing the fact that a high percentage (reaching 92%) of the patients with idiopathic RLS have a family history of RLS. This has been taken into account in RLS studies inferencing the significance of genetic factors in the disease [8].

Patients with other neurological disorders, iron deficiency, pregnancy or chronic renal failure might develop RLS and because of the fact that it is caused by those points characterized as secondary RLS. There are studies which found a low ferritin level in RLS patients. Additionally, diabetic peripheral neuropathy, painful neuropathies, attention-deficit/hyperactivity disorder (ADHD), migraine, ankylosing spondylitis (AS), leprosy, inflammatory chronic demyelinating neuropathies like multiple sclerosis and Guillain–Barré syndrome, thyroid disease, poliomyelitis, chronic venous disorder, autoimmune disease including Sjögren's syndrome, rheumatoid arthritis, inflammatory bowel disease and Crohn's disease are conditions which increase the possibility of RLS existence. This disease should not only be attributed to the nature of each disease but also as the side effects of certain drug taking. Furthermore, when a stroke affects the pyramidal tract and the basal gaglia-brainstem axis the likelihood of RLS development is increased as this particular brain region is responsible for motion.

Another classification of RLS is determined according to the age of onset of the symptoms. When symptoms appear before the age of 45 the disease is referred as early-onset RLS and late-onset RLS when this occurs at an older age. Family history seems to be more closely related to early-onset RLS [8].

In order to diminish secondary causes of the RLS, a detailed medical check is required including neurologic and vascular examination, electromyography (EMG), electroneuronography (ENG) and PSG control as well as hematological and biochemical check [2].

1.2.3 Deferential diagnosis

Differential diagnosis plays a crucial role in RLS patients and their treatment, so additional questionnaires have been created supporting the improvement of diagnosis. Some of them are the RLS-NHI, the RLS-EXP and the CH-RLSq [8]. The usual conditions that have to be differentiated from RLS are legs cramps, positional discomfort, local leg injury, arthritis, leg edema, venous stasis, peripheral neuropathy,

radiculopathy, radiculopathy, habitual foot tapping/leg rocking, anxiety, myalgia and drug-includes akathisia and less common are myelopathy, myopathy, vascular or neurogenic claudication, hypotensive akathisia, orthostatic tremor and painful legs and moving toes [11].

1.2.4 Secondary RLS

The first hypothesis about the cause of RLS, that arose in the middle of 20th century, concerned the low iron levels found in a significant number of patients. This was also supported by pharmacological studies which indicated improved clinical features in RLS subjects after being administered iron supplements. The developed investigation in recent research of this undefined field, stressed that the iron levels in blood are not quite equivalent with iron in CSF. It can be proven from MRI studies most of which have revealed reduced iron levels in the substantia nigra and putamen in addition to low iron levels in red nucleus, thalamus or pallidum.

RLS symptoms are also experience in 15-25% of women during pregnancy (usually in 3rd trimester and later). The possible reasons why pregnant women suffer from RLS might be their low ferritin levels, hormonal status, folate deficiency and stretch or compression of nerves because of the fetal growth.

Recording the characteristics of RLS in the general population, it is also important to mention hemodialysis which can be correlated with RLS at 3.9-15% of the general population. The symptoms are extended in patients with end-stage renal disease. In a thorough study it was found that the prevalence of RLS is associated with their body mass index (BMI). For this reason, a possible cause might be the dopamine receptors in obese people's brains. In summary, it is very frequent that patients with end-stage renal disease suffer from RLS as well as the emergence of muscle atrophy in hemodialysis patients with RLS [8].

1.2.5 Pathophysiology

The determination of pathophysiology of RLS is achieved focusing on different approaches. These refer to changes in iron metabolism, abnormalities in dopaminergic system, genetic variation and disturbances in nervous system structures.

The endothelial cells in the interface of blood brain barrier (BBB) are responsible for iron production. A possible disturbance in the interface of BBB has a direct relationship with iron deficiency. Specifically, lower iron indexes in endothelial cells are the result of a dysfunction of iron regulatory protein in the microvasculature that

affects the transportation across BBB. The inadequacy of iron could cause cellular damage by oxidation and modification of cellular compounds. The pathophysiology of RLS is formed directly from these relations between the neurons that present disturbances of iron and neuromelanin-containing and dopamine-producing cells. Consequently, the brain dopaminergic transmission is influenced by the extracellular dopamine, DAT, D1 and D2 receptors when they have low values.

Pharmacological studies have demonstrated that the dopaminergic system in the central nervous system has a negative impact on the pathophysiology of RLS. It is based on the idea that dopaminergic medications provide a rapid suppression of symptoms in contrast with dopamine antagonists which are not able to cross the BBB, a fact that should be overcome. Thus following the same tactic in treating effectively Parkinson's disease, which is another relative movement disorder. Iron is a co-factor of tyrosine hydroxylase which reduces the speed process of the conversion of levodopa into dopamine, so its inadequacy could cause disturbances in dopaminergic system in brain. The production of dopamine occurs midbrain and close to hypothalamus from the dopaminergic A11 cells which reach the dorsal horn and then continue until they arrive at the motoneuronal site. There exists the prevailing view that the long projections to the spinal cord are afflicted as a natural procedure of aging. The appearance of RLS symptoms is inevitable due to this process of degradation, which negatively influences the function of spinal sensory and motor systems. Studies have emphasized on the significance of A11 cells as the stereotaxic bilateral 6-hydroxydopamine into the A11 nucleus implies enhanced standing episodes. Proton magnetic resonance spectroscopy, fMRI and PET have recently indicated the contribution of medial thalamus nuclei in RLS pathophysiology. Additionally, another consequence of the reduction of iron could prompt cell death in the dopaminergic cells in the substantia nigra, suggesting opioids as an appropriate treatment due to the neurotransmitter systems which contain endorphins and enkephalins [8, 12, 13].

It was obvious even from the 20th century by the first RLS researchers that there is familial accumulation in the RLS cases, leading Ekbom to conclude that one out of three cases have to do with inheritance [14]. Subsequent genetic association studies have found that more than half of RLS patients (60%) have a positive historic background indicating 5 genes and 10 different risk alleles for RLS [13, 15]. The inherited aspect of the syndrome affects mostly late-onset RLS and secondary RLS patients [8]. Genome-wide association studies (GWASs) has recorded the BTB domain

containing 9 (BTBD9), MEIS homeobox 1, receptor type D (PTPRD), mitogen-activated protein kinase 5/SKI family transcriptional corepressor 1 (MAP2K5/SCOR1) and less commonly TOX3 the related with RLS single nucleotide polymorphisms (SNPs), whose main function is associated with embryonic neuronal development and limb movement [8, 16, 17]. BTBD9 is contained in synaptic plasticity and learning while it is inextricably connected with RLS and PLM patients. Important studies have compared the RLS symptoms to mice and flies' behavior in which there is an absence of BTBD9 (accompanied by reduced dopamine levels in the whole brain), illuminating the common sleep fragmentation and motor restlessness. Additionally, a supporting finding that could be correlated with RLS symptoms is the overexpression of BTBD9 in embryonic kidney cell line which demonstrates enhanced ferritin levels. The normal development of limbs and motor neuron connectivity is driven by the homeobox gene. Furthermore, the cells that are characterized by the expression of MEIS1 participate in the procedure concerning nigrostriatal projection formation. Half cases of RLS occur due to the existence of the MEIS1 risk allele, which causes to RLS patients limited MEIS1 mRNA and protein in lymphoblastoid cell lines. MEIS1 is associated with the iron system and an evidence of its influence in iron homeostasis can be seen in Caenorhabditis elegans [16]. The receptor type tyrosine phosphatase D (PTPRD) gene is responsible for the encoding of a cell adhesion molecule which possibly affects the formation and connections, addiction-, locomotion- and sleep-related brain circuit in which it is expressed [18]. Its character acting as a homodimer, possibly illuminates the way PTPRD differences affect RLS-vulnerability-altering variations in dopaminergic connectome [19].

The additional genes MAP2K5 and SKOR1 (LBXCOR1) might be the source of RLS symptoms. The expression of SKOR1 mainly exists in a subset of dorsal horn interneurons in the developing spinal cord which correlates with pain and touch. The SKOR1/Lbx1 pathway is a factor contributing to the production of GABAergic versus glutamatergic phenotype in these cells altering the phenotype that relates to sensory and pain. TOX3 (a gene related to breast cancer) and BC034767 have recently been regarded as probable elements connected with RLS development, however, their accurate influence in the disease is still unclear [20].

According to a recent study attempting to classify the effect of the aforementioned SNPs in RLS and PLM, it was found that the stronger in RLS is MEIS1, then follows BTBD9, MAP2K1/SCOR1, TOX3 and the last gene is PTPRD. Respectively, in PLM,

BTBD9 is in first place, next in the hierarchy is TOX3, then MEIS1 and finally PTPRD and MAP2K1/SCOR1 [21].

1.2.6 Treatment

Lifestyle changes, meditation effects and iron levels are necessary to be checked, before any treatment is given. Limited sleep, alcohol or tobacco use, the absence of exercise or medication are reasons that could intensify the RLS symptoms leading to the need of personal patient control. As in many other disorders there are non-pharmacological as well as pharmacological approaches for treatment.

Improving sleep quality is helpful following the first approach which excludes drug taking. Alcohol, caffeine and eating heavy meals before sleep should be avoided. Patients should follow a regular rate of sleep hours. In a study which lasted for 3 months it was suggested that exercise can work efficiently in patients with RLS, however it might have negative effects if it performed late in evening or more generally before sleep time. Additionally, a progress concerning the reduction of symptoms was noticed after cognitive behavioral therapy. Furthermore, secondary factors such as iron or magnesium deficiency should be clarified as their treatment with iron or magnesium complements can diminish RLS symptoms. A more glaring but relative case is that of kidney transplant, which helps patients with renal failure to almost achieve complete recession of symptoms [2, 8, 12].

According to pharmacological approach of RLS treatment, the main factors concerning the dopaminergic agents including pramipexole and ropinirole, indicating an improvement of 70-90% of symptoms in RLS patients. In order to avoid side effects, dopamine agonists (which function as dopamine in the dopamine receptors of the brain) are much preferable to L-dopa. On the other hand, pergolide and cabergoline are not suggested since they are related to valvular heart disease. Additionally, the side effects of ergot-derived drugs may be avoided with the administration of nonergota-mine derivatives like ropinirole and pramipexole. The stimulation of D2 and D3 receptors is accomplished by dopamine agonists. Another drug, rotigotine which is used in Europe but disapproved by the FDA in US, can provide an around the clock treatment through transdermal patches. Alpha-dihydroergocryptine (Almirid) and piribedil are other non-promising dopamine agonists [8, 13, 15].

Unfortunately, the administration of dopamine agonists (ropinirole, pramipexole, pergolide) is accompanied with some unwanted symptoms which may be nausea,

congestion, insomnia, fluid retention and behavioral symptoms, such as hallucinations. Augmentation that is connected to more severe symptoms during daytime comes from long-term L-dopa and dopamine agonist administration and as soon as it is detected, its treatment should be altered by other medication [13].

Furthermore, the oral iron treatment has been found from a recent double-blinded placebo-controlled study, as an appropriate method to limit symptoms. Also, an alternative method suggests the treatment including large doses of iron dextran leading to a good determination of long-lasting symptoms.

If patients do not respond adequately to dopaminergic medication (usually in severe RLS), opioids may provide more efficient treatment. Hydrocodone, oxycodone and codeine which are short-acting agents can relieve patients suffering from recurrent symptoms or night legs activation. In contrast, oxycodone, methadone or fentanyl patches belong to long-acting opiates and are beneficial agents in severe RLS cases. Despite the reduction of RLS symptoms and the improvement of sleep quality using opioids, their administration also carries undesirable effects which include exacerbation of sleep apnea, limited REM, slow wave sleep, sedation, fatigue, constipation, addiction and Q-T interval prolongation and torsades de pointes.

Despite the fact that pregabalin which is a modulator of the alpha-2 delta receptor is considered an appropriate treatment for epilepsy, neuropathic pain, generalized anxiety and fibromyalgia, the contribution of alpha-2-delta anticonvulsants in RLS make it a novel treatment. There are studies that demonstrate their significance in improving sleep quality of patients and they also stress the alternative medication that works efficiently in RLS indicating new approaches for treatment [15].

Taking into consideration the depression that appears in RLS patients and the antidepressants (selective serotonin reuptake inhibitors (SSRIs) and tricyclic antidepressants (TCAs)) that make worse the symptoms, scientists suggests bupropion which has been proven to fight depression and avoiding RLS development.

RLS treatment during pregnancy and lactation should be attentively performed with primary preference in non-pharmacological treatment. Four years ago, IRLSSG recorded guidelines that pregnant women should follow in order to treat annoying symptoms of RLS. In short, relieving symptoms may be achieved through light exercising and iron deficiency treatment avoiding long-term immobility serotonergic antidepressants intake [8].

Chapter 2. Functional Magnetic Resonance Imaging

2.1 History

In the field of neuroscience and specifically in brain functional connectivity analysis, there are two fundamental non-invasive methods that have been developed over the past years that aim to map the brain's functional connectivity. In the first category the methods used locate the underlying neural electromagnetic activity of the brain and in the second reflect the local neuronal signaling by mapping the local physiological or metabolic consequences of the altered brain electrical activity. The most common technique belonging to the first method which examine the electrical and magnetic activity of the brain providing high temporal but poor spatial resolution, are Electroencephalogaphy (EEG) and magnetoencephalography (MEG). The second category involves modern in-vivo imaging techniques such as magnetic resonance imaging (MRI), positron emission tomography (PET), functional magnetic resonance imaging (fMRI), etc. In this study we emphasize on fMRI, a non-invasive powerful approach that is based on the increase in blood flow or blood oxygenation to the local

vasculature that accompanies neural activity in the brain and provides excellent spatial resolution with limited temporal resolution [22].

The scientific developments which have led to modern fMRI is described through the following main phases. As early as the 1930s, the American chemist and Nobel laureate Linus Pauling and his student Charles Coryell had indicated that the magnetic properties of oxyhemoglobin (bound oxygen molecule with hemoglobin) differ from the magnetic properties of deoxyhemoglobins' (hemoglobin without oxygen). Paramagnetic deoxyhemoglobin (both unpaired electrons and a significant magnetic moment) produces local field inhomogeneities in the measurable range of MRI resulting in signal decrease in susceptibility-weighted MR-sequences (T2*), whereas diamagnetic oxyhemoglobin (no unpaired electrons and zero magnetic moment) does not interfere with the external magnetic field.

At the end of 1980s, researchers at Bells laboratory, investigated the physiology of the brain with magnetic resonance methods. More specifically, anesthetic rats were studied in 7 Tesla magnetic field in special conditions (100% O_2 and 100% CO). The images, which were acquired through gradient echo sequences, had a different signal from that which had been collected from rats breathing fresh air (oxygen content 21%). Specifically, in the last ones there were visible small black lines on the surface of the brain that scientists attributed to the blood vessels and reflected the differences of the magnetic susceptibility of hemoglobin [2, 23-25]. However, it was Ogawa's and his collaborators' fundamental observations which showed, that the blood oxygenation level was able to control these distortions, a fact that later led to the development of the well-known Blood Oxygen Level Dependent (BOLD) contrast mechanism [26]. Functional Magnetic Resonance Imaging (fMRI) is a rapidly evolving application allowing visualization neuronal activation *in vivo.*

The first studies were recorded in 1992 from three individual research groups. Among the former, was Kenneth Kwong's and his collaborator's team, followed by Owaga's and Bandetti's works. The research team in which Kenneth Kwong was leading used a sequence of visual stimuli with Echo Planar Imaging (EPI) in 1.5 Tesla magnetic field to measure the activity of the visual cortex. It was a block design fMRI paradigm in which a visual stimulus (lighting LED light) was presented and absent (darkness) in turn with equal time periods of 60s, resulting in the revealing of the visual cortex activation. The next year, Ogawa presented the biophysical background of the BOLD contrast in the Biophysical Journal. In 1995, Bandettini published a chapter

where the quantitative determination of the functional activation maps was presented. Ever since functional MRI was first described, rapid progress has been made in this field, and the technique is now widespread and extensively used for clinical and research purposes [2].

One of the most challenging processes in the field of neuroscience is to comprehend the relationship between the BOLD signal and the neural activation. The measurement of the increased neuronal activity is achieved indirectly via a change in the local magnetic field (in)homogeneity, which is caused by an oversupply of oxygenated blood. The change in the local HbO_2/Hb ratio acts as an endogenous marker of neural activity. The BOLD signal does not correlate perfectly with neuronal action potentials but measures a mix of continuous membrane potentials and action potentials. This offers an opportunity to consider whether our understanding of neural information processing might extend beyond action potentials and include a range of signals that are an important part of neural computation [24, 27].

Figure 2.1: fMRI scanner which is located in University Hospital of Ioannina.[1]

Functional Brain Studies

A functional connectivity study using fMRI (fcMRI) has drawn increasing attention in the field of neuroscience and computer science, since it is one of the most important techniques used for understanding the activity of the human brain [25, 28]. Nowadays, it has been established that fMRI has been used in a large number of studies with an

[1] Adapted from: *https://www.snf.org/en/grants/grantees/u/university-hospital-of-ioannina/radiology-department-equipment/.*

increasing number of papers that mention the technique in the PubMed database of biomedical literature, as shown in Fig. 2.2 [29].

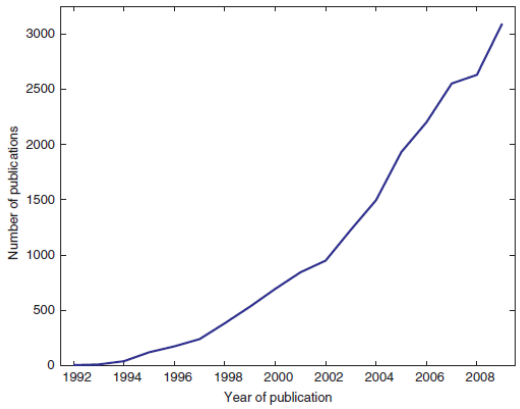

Figure 2.2: A plot of the number of citations in PubMed databases for every year since 1992 [29].

Functional Magnetic Resonance Imaging studies of the brain compose one of the most recent applications of magnetic resonance imaging. There are techniques that are used in these studies which provide important information for the fundamental brain functions, rendering it unique. Apart from the morphological representation of anatomical structure, these techniques are able to reveal activation areas during stimulation or during a task [30]. Because of the fact that fMRI has great advantages compared to other methods of brain mapping in cognitive and neuroscience systems, there has also been great interest in using fMRI to assist in clinical diagnosis and management, with promising demonstrations of effectiveness in a number of applications [31].

The functional imaging techniques include three main study categories. These are brain activation, blood flow in microscopic level and diffusion [30].

2.2 Brain activation

The most important application of fMRI is the direct observation of the activation of the cerebrum cortex with no associated radiation exposure. The brain activity reflects local changes of metabolism and hemoglobin conditions. The first contrast mechanism, that defines the effect that there is increasing signal where the cortex areas are activated, is related to the changes in the local oxygenation of the blood and is represented by the techniques that called BOLD. The second one is associated with inflow effects [30].

2.2.1 The BOLD contrast mechanism

fMRI is a technique which measures the changes in the blood oxygenation levels (BOLD signal) and gives us an indirect measure of the neuronal activity in the brain [26]. Under normal conditions local oxygen concentrations are relatively low, so blood contains a high concentration of paramagnetic deoxyhemoglobin, whereas the brain tissue is diamagnetic. This means that at the interfaces of vessels and brain tissue there are magnetic field inhomogeneities that shorten T2* and give rise to a signal reduction in T2*-weighted gradient echo images [32]. When the human brain receives a stimulus, an increase in neuronal activation take place. During neuronal activation, more oxygen is transported to the site of activation at a percentage of 20-40%, while the oxygen consumption is only at 5%, which means a washout of deoxyhemoglobin and an increased concentration of oxyhemoglobin [30]. This disproportion leads to the increase in the percentage of oxygen in the activated area. Due to the increasing magnetic susceptibility of the oxygenated blood, the activation area is characterized by great T2* constant in comparison to the non-activated brain regions. As a result, if the T2* sequence is chosen, the activated areas produce a more intense signal.

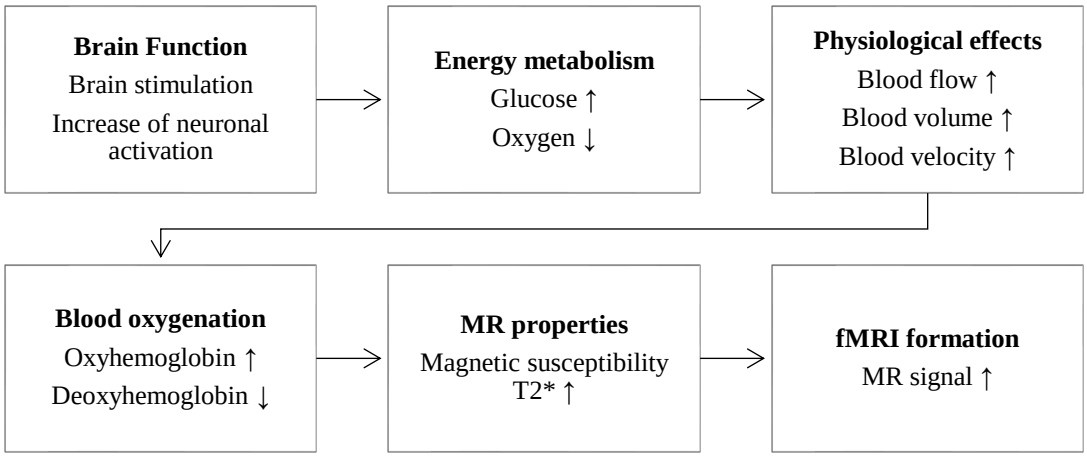

Figure 2.3: Schematic representation of the fMRI formation [33].

The previous representation in Fig 2.3 is called BOLD and the magnitude of this effect is increased with the square of the strength of the static magnetic field. When the field strength is low (i.e., less than 0.5 T), the difference between the transverse relaxation values for oxygenated and deoxygenated blood is small, but in higher fields (i.e., 1.5 T or greater), these values have significant differences. If the sequence applied

is controlled in a such a way that minimizes the inference of inflow effects involving the brain activation areas, the T1 contrast is minimized as well [25, 30].

2.2.2 BOLD response

In summary, BOLD imaging is based on the aforementioned magnetic differences between the oxygenated and deoxygenated hemoglobin which result in the generation of local gradients in the magnetic field whose strength depends on the HbO_2 concentration.

Overall, the balance between oxyhemoglobin and deoxyhemoglobin within some voxels of interest depends on the local self-regulation of arteries and vasodilation. The increasing of some features such as Cerebral Blood Flow (CBF), cerebral brain volume (CBV) and oxygen transport, are associated with the neuronal activation. If the CBF represents a greater increase than CBV, the blood flow exceeds the small increases in the local need for oxygen due to the brain activation. Thus, the venous and capillary network fill with a greater amount of diamagnetic oxyhemoglobin, than those in a resting state condition, because of the oxygen transportation. This increased amount leads to a bigger T2* and a greater signal in T2*-weighted images. The range of the increasing signal is 1-10% [30].

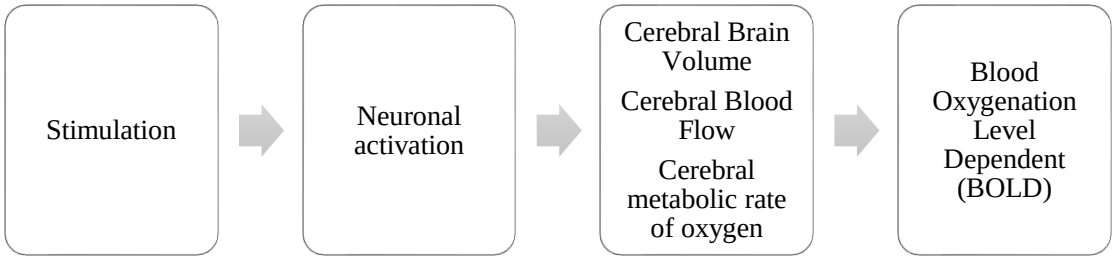

Figure 2.4: Transformation of stimulation in BOLD response [30].

The change in the MR signal triggered by neuronal activity is known as the hemodynamic response (HDR) [25]. The Fig. 2.5 shows the hemodynamic response for a typical signal time course following neuronal activation associated with an external stimulus (task) or spontaneous brain activity.

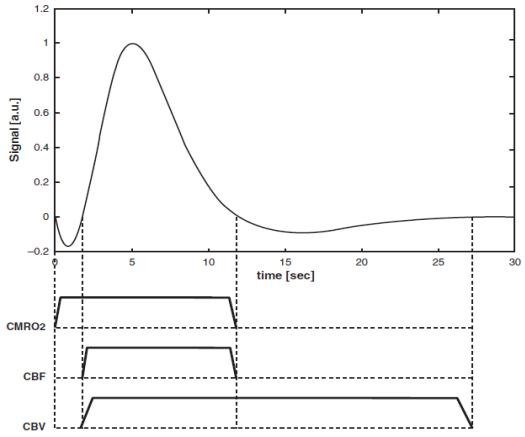

Figure 2.5: The time courses of the physiological parameters, metabolic rate of oxygen consumption ($CMRO_2$), the CBF, and the cerebral blood volume (CBV), after activation [32].

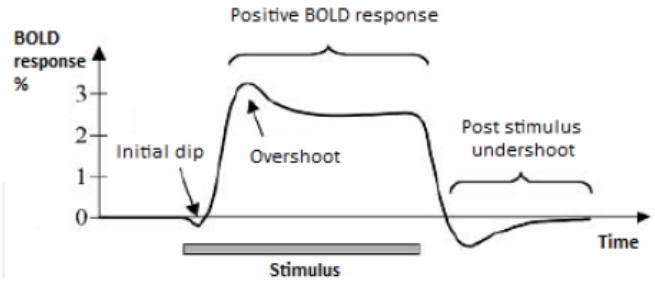

Figure 2.6: Schematic representation of the BOLD response [33].

The common features of the fMRI BOLD response to a period of neural stimulation is given in Fig. 2.6 and the three epochs are: a) initial dip, b) positive BOLD response, and c) post stimulus undershoot. If we focus on an active voxel's activity using BOLD fMRI, it has been noted that its signal increases above the baseline at about 2s following the onset of neuronal activity, growing to a maximum value (peak) of about 5s from a shot duration stimulus. Provided that the neuronal activity is extended across a block of time, the peak could be similarly extended into a plateau. After reaching its peak, the BOLD signal decreases in amplitude to a blow-baseline level and remains below baseline for an extended interval. This effect is known as the post stimulus undershoot [25, 33].

2.3 Image acquisition process-Types of fMRI experimental design

For anatomical images of the brain contrast is more important than the speed of acquisition, since structural parameters, such as size and shape, change a little over the course of a single scanning session. However, understanding the function of the brain requires images to be acquired very rapidly, at approximately the same rate as the

physiological changes of interest. The development of gradient technology has made EPI the most common fast imaging method for functional MRI [25] which is fast and sensitive in BOLD contrast.

The data acquisition includes the following steps. During the fMRI experiment the subject is positioned in the scanner and asked to alternatively perform several tasks or is stimulated so that different processes or emotions are triggered. The stimuli are usually audio or visual and stimulations involve the motor cortex, as well as, more cognitive demand functions such as the function of memory and thought. Each one of the aforementioned experimental conditions are repeated at different periods of time and can be alternated by inactive and relaxing periods [33].

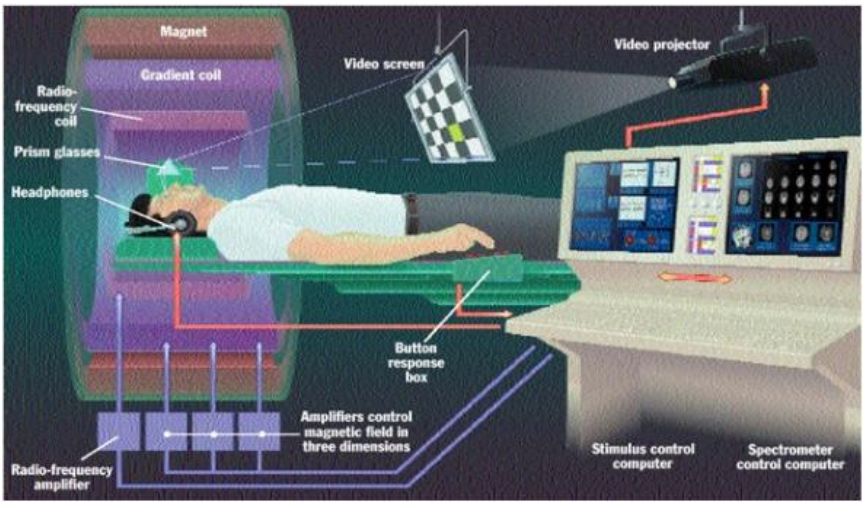

Figure 2.7: The equipment needed for carrying out a fMRI experiment.[2]

The majority of functional neuroscience studies have focused on the brain's response to a task or stimulus. However, the brain remains extremely active even in the case when stimuli are absent [34]. The topic or the medical problem which is under being examined determines the way in which the experiment is organized [30]. The experimental design for fMRI, is distinguished in task related designs and those that are carried out during resting state conditions (task-free fMRI). Frequently, the combination of both methods is worthy, because of the importance of the findings that are derived.

2.3.1 Task-based fMRI

The most common types of task-based fMRI are the following: "Block design" and "Event-related design". "Mixed design" is also possible (combining aspects of block

[2] Adapted from*: http://fmri.ucsd.edu/Research/whatisfmri.html*.

and event-related designs), however it is much more complicated to design and analyze. In each case, the difference in BOLD contrast between two states infers the effect size [35].

The most time-efficient approach for comparing brain responses to different tasks during the experiment is the block design. According to this method, the stimulus is presented continuously for a long period (e.g. 30s) that is called block. Activation blocks are alternated with the baselines or resting blocks when the patient is in a resting state or no stimulus is presented. Activation block may consist of one type of stimulus that lasts for a long time or many different types of stimuli that alternate at a fast pace. It is also appropriate that scientists incorporate different types of block in the same study, as it is feasible to study different types of stimulus each processing their own block. There are benefits and drawbacks of block experimental design. First of all, due to the vast amount of data it requires for the computation of the average of responses, this design provides a good signal to noise ratio. This is what makes the detection of the activated areas in the cerebral cortex more effective. On the other hand, there are many interpretive problems that arise. The presentation of a simple stimulus is fast, so the responses are overlapped. As a result, this design does not allow a good estimation of the hemodynamic response. Specifically, the what makes the estimation of the shape of hemodynamic response difficult is the non-linearity of the overlapping responses. Because block design paradigms are less demanding, they are well suited for many experimental cases. Complex cognitive tasks, (for example, 'oddball' paradigm, in which the reaction is detected by an unexpected stimulus), may not be amenable to a block design. Because of the fact that the responses are studied using average, phenomena, as possible inaccuracies involved in magnet synchronization with the stimulus-delivery equipment, stimulus timing or stimulus randomness, are less important than event-related designs [23, 30].

The second major type of task-based fMRI experiments is "event-related" design in which the stimulus is presented randomly. Event-related, or trial-based, measurement is already standard testing in the field of electrophysiology, and is related to stimulus-locked, event-related potentials (ERPs) [36]. In order to achieve a sufficient signal to noise ratio, event-related fMRI demands longer acquisition times than the block design [22].

A crucial advantage of event-related design over block design is the cognitive behavior of the subject. It is possible, in a block design experiment, for cognitive

behavior to interrupt the patient response, as a patient might wonder when the next stimulus is going to be presented or what kind of stimulus this is. In the event-related design the familiarization of the patient with the experiment is avoided, due to the randomization of the stimulus presentation and the fact that some of them can be given unpredictably. The trials can be individually categorized or parametrized depending on the subject's performance, regarding the accuracy of the reaction time, for example. In addition, some experiments involve events that cannot be blocked, such as 'Oddball' paradigms, in which the stimulus that is presented disrupts the prevailing context [30, 36].

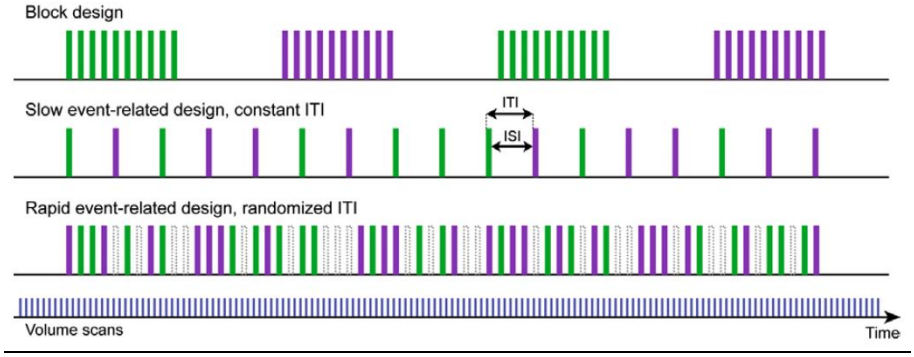

Figure 2.8: Types of fMRI experiments [24][3].

2.3.2 Resting-state fMRI

During the last decade, there has been an increase interest in the application of the technique at rest, as there is a set of brain regions which are very active even in the absence of stimuli. Subjects lay in the scanner under "resting state" conditions, being for instance in an eyes-closed or an eyes-open condition with or without a fixation target. This resting-state fMRI focuses on spontaneous low frequency fluctuations (<0.1 Hz) in the BOLD signal and reveals spontaneous neuronal activity.

There are several strong advantages regarding the use of the resting-state fMRI with respect to the task-based fMRI. First of all, the complex set-up for stimulus presentation, the response recording and the task timing control, is often expensive and is avoided in the resting state fMRI. Another issue that should be taken into consideration, is the fact that most of the patients are not able to respond to a task-based fMRI experiment effectively. As a result, the absence of stimulus might work efficiently. Third, the signal to noise ratio in resting state studies is better than task-

[3] ITI: inter-trial interval, ISI: inter-stimulus interval.

based approaches. Finally, because of the task-free nature of resting-state fMRI the parameters that may cause problems in the interpretation of the task can be ignored.

On the other hand, a limitation of this modality is the fact that when a certain brain network should be examined, a task-based method is the only way to achieve it. Secondly, for multi subject analyses, an issue that should be kept in mind is the subject's mental state that relates to the brain energy. For instance, for the study of specific diseases, such as schizophrenia, working memory tasks are preferable in order to distinguish baseline period and stimulus presentation stimulus. Last but not least, controlling the subjects' memory is impossible due to the resting state condition of the subject [34, 37-39].

2.3 Advantages and Disadvantages of fMRI

There are at least three reasons why functional Magnetic Resonance Imaging makes the future of functional brain imaging particularly interesting. First, fMRI does not involve ionizing radiation, and therefore it can be used repeatedly on a single subject and even on children, allowing long-term studies. Second, technical improvements in fMRI (due to more powerful magnets, more sophisticated imaging hardware, and the development of new methods of experimental design and data analysis) promise to ameliorate spatial and temporal resolution. Third, there is an increasing attempt to integrate the findings based on fMRI with those from other complementing techniques, such as electroencephalography (EEG) and magnetoencephalography (MEG), which have much greater temporal resolution. The high cost and the state in which the patient has to stay motionless during the examination in order to capture clear functional images, are some crucial disadvantages of fMRI [27, 33, 40].

2.4 Spatial and temporal resolution

The good spatial and temporal resolution are the issues that made the fMRI a popular technique [33]. By using the phrase "spatial resolution" we refer to the ability to distinguish the changes in an image (or map) across different spatial locations, while temporal resolution describes the ability to distinguish changes concerning activity at a single location over time [25]. Spatial resolution is basically restricted by limited imaging time and by signal to noise ratio (SNR). Smaller voxels recommend smaller SNR but also enhance spatial resolution by making possible the detection of smaller structures and smaller activated areas [33]. It provides important information about the gray and white matter with a relatively high spatial resolution in the order of millimeters

but with a temporal resolution of a few seconds which is limited by the hemodynamic response itself. Because of the short acquisition time, high temporal resolution of fMRI is possible, but it is limited by the blurred intrinsic hemodynamic response and a finite SNR [23, 33].

fMRI can be compared to other imaging methods, such as Positron Emission Tomography (PET), Near Infrared Spectroscopy (NIRS), EEG and MEG which are primary alternatives, used to obtain functional evaluation of brain metabolism in terms of spatial and temporal resolution and availability. The spatial resolution of EEG and MEG is limited to 10-20mm. This is because the scalp-based measurements of electrical and magnetic distributions are not able to provide unique dipole reconstruction. The spatial resolution of EEG is smaller than MEG due to the fact that EEG might be spatially distorted by electrical conduction. On the other hand, EEG and MEG can easily capture the dynamics of brain activity and thus offer excellent temporal resolution, in the order of milliseconds. BOLD fMRI provides excellent spatial resolution however small temporal resolution which is mainly related to the hemodynamic activity. If higher field magnets (7T) are used, a fMRI pixel size of 500 microns or less may be easily reached, although the typical pixel size is 3-4 mm. Both Near Infrared Spectroscopy (NIRS) and EEG offer similar spatial resolution (close to 5 mm) which however is limited by the problem of reconstructing HbO_2 3D maps from scalp recordings, in addition to the scattering and attenuation of the infrared photons which hinder deeper brain penetration. Temporal resolution of NIRS is very much alike to fMRI because of the temporal limitations of blood oxygenation. The spatial resolution of Positron Emission Tomography (PET) ranges between 5 and 20 mm as the size of gamma ray detectors and the positron-electron annihilation range limit it. Of all the methods PET has the greatest temporal resolution due to the low count rates of the injected nuclide, thus requiring further scans [41].

fMRI's spatiotemporal resolution can be mainly enhanced by: (i) optimizing the MRI pulse sequences, (ii) improving resonators, (iii) using higher magnetic fields, (iv) developing intelligent strategies for parallel imaging. fMRI is expected to supply images of a fraction of a millimeter (e.g., $300 \times 300\ \mu m^2$ with slice thickness of a couple of millimeters) regularly, which amounts to ~2–3 orders of magnitude smaller voxel-volumes than those that are nowadays used in brain imaging. The aforementioned resolution may be achieved in whole-head imaging protocols, by an increasing number

of acquisition channels, producing superior maps of distributed brain activity in great regional detail and with reasonable temporal resolution of a couple of seconds [42].

2.4.1 fMRI time-series

The functional images, are T2* weighted images with lower spatial resolution than anatomical images. The way that anatomical images are considered and examined differs from functional images. Their accumulation takes place in a certain time rate and constitutes a set of images. Each voxel's intensity value in each image of the set is called time-series of the specific voxel (Fig. 2.9) [33].

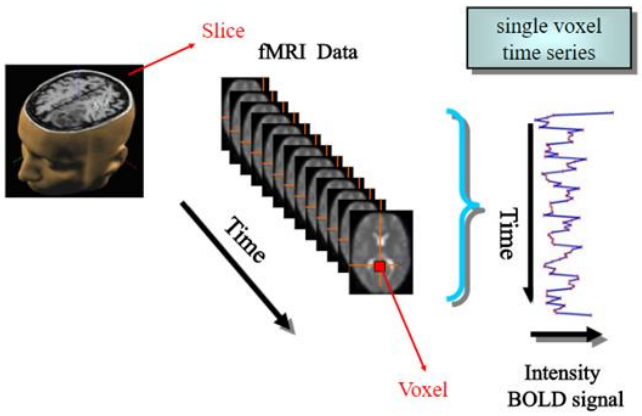

Figure 2.9: fMRI time-series.[4]

2.4.2 Source of noise in fMRI

Structure and random noise are also included in fMRI time-series, as well as the activity evoked by the experiment (effects of interest). The sources that may produce noise in fMRI are the following: a) thermal noise arising from the subject, the receiver coil and the amplifiers, b) systematic noise arising from subject motion, c) systematic noise arising from tissue pulsation related to cardiac and respiratory cycles, and d) noise due to slow fluctuations in blood oxygenation [33].

2.5 Applications of fMRI

Functional neuroimaging has greatly assisted the way that cognitive neuroscientists study the relationship between brain and behavior. The use of fMRI is constantly increasing and has become the standard modality to visualize regional brain activation. The variety of applications can be distinguished in two categories: the cognitive neuroscience applications and the clinical applications. The first category includes

[4] Adapted from: *http://slideplayer.com/slide/9047889/*.

those that are used to detect brain regions which are responsible for a variety of human brain functions and those that study how the brain areas react according to the stimulus they receive. Moreover, understanding the learning mechanism, locating networks that are accountable for cognitive functions, as well as the combination of fMRI with electrophysiological techniques. The clinical applications involve the imaging of activated brain areas which have been injured, the monitoring of rehabilitation or reorganization after an injury and the providing biomarkers or patterns for diagnosis [23, 33].

2.5.1 Cognitive neuroscience

A main purpose of neurophysiological studies is the brain function detection. Brain regions that are associated with specific perceptual, cognitive, emotional and behavioral functions, such as sensorimotor, visual, language and memory can be detected [33]. An important contribution of fMRI is also understanding the way in which an activated brain area influences another one. For example, it is widely accepted that a visual stimulus can configure the brain response at the touch of an object or a face. In cognitive neuroscience applications, it has been successfully used to study brain systems that involve learning and demonstrate the plasticity of brain systems. In other words, the correlations in activity among areas change as a function of time and learned performance [23].

BOLD and EEG signals are differently generated and exhibit different temporal and spatial properties. For this reason, the combination of fMRI with other electrophysiological techniques such as Electroencephalography (EEG) has given the opportunity to scientists to extract important information about brain function [32].

2.5.2 Clinical applications

In order to study patients with neurodegenerative diseases, the fMRI can be applied in different ways showing that this technology can also be used for other neurological disorders [43].

To manage an individual's medical problem, in clinical studies, single subject results are demanded, whereas in research studies the result is taken from a group of studied subjects, in a highly controlled environment. In clinical applications there are several aspects of the fMRI that should be taken into consideration in order to ensure successful and high quality clinical studies. These are: a) the quantitative and qualitative sufficiency of the personnel, b) the necessity of effective patient cooperation, c) the

good patient preparation, d) the patient safety, e) the correct organization of the paradigms, f) the scanner capability, g) the analysis and the presentation of the data. By ensuring these aspects, neuroscientists use the applications of fMRI in pre-surgical planning, the diagnosis of diseases like epilepsy and Alzheimer Disease and the treatment of arteriovenous malformations.

Pre-surgical fMRI is used to enable function preserving and safe treatment in patients with brain tumors and epilepsies by noninvasively localizing and lateralizing specific brain functions or epileptic activity. The surgical resection of selected malignancies requires the accurate localization and the histological gradation to achieve complete removal. However, the proximity with the surrounding cortex regions is required to ensure that the removal of the selected malignancies will be safe and will not harm other vital brain functions. The morphological brain imaging or invasive measures prior to treatment can't give this diagnostic information [23, 24, 30].

In summary, the diagnostic aims of pre-surgical functional neuroimaging are the following: a) the localization of sensitive brain areas with respect to the envisaged site of surgery, b) the determination of the dominant hemisphere for specific brain functions, c) the localization of epileptic zones and lateralization of epileptic activity and d) the delineation of neuroplastic changes in brain activity.

Patients after an acute and subacute phase of stroke show variable recovery which can be investigated with fMRI [23]. Specifically, fMRI has been used due to the spatial imaging of the recording motor cortex and language function and it has proven that the function in those areas is associated with the plasticity of the brain that is very supportive to the stoke treatment [30].

Scientists have used fMRI to identify abnormal functional brain activity during task performance in a variety of patient populations, including those with neurodegenerative, demyelinating, cerebrovascular, and other neurological disorders that highlight the potential utility of fMRI in both basic and clinical fields of research [43]. The importance of fMRI lays not only in its usage for diagnosis of diseases such as Dementia, Parkinson Disease, Autism, Restless Legs Syndrome etc., but also in its ability to distinguish the characteristics of each disease in healthy and pathological subjects. In chapter 3 there is an external description about the use of fMRI in Restless Legs Syndrome.

Chapter 3. Imaging technique used for Restless Legs Syndrome

There is a great body of literature on studies that provide useful information about neurological disorders, such as Restless Legs Syndrome (RLS), using various imaging techniques to investigate different cases involved in the pathophysiology of RLS. In this chapter, studies that have been carried out in recent years, including positron emission tomography (PET) and single positron emission computed tomography (SPECT) studies, mainly focusing on the dopaminergic pathway, magnetic resonance imaging (MRI) studies, employing various techniques such as iron-sensitive MRI methods, voxel-based morphometry (VBM), magnetic resonance spectroscopy (MRS), diffusion weighted sequences and task based or resting state functional magnetic resonance imaging (fMRI), which are presented in detail. It is worth noting that there are discrepancies between the findings [44]. More emphasis will be placed on resting state fMRI methods as the dataset that has been used in our analysis is acquisitioned through this method.

3.1 Brain imaging in Resting Legs Syndrome

PET and SPECT

PET and SPECT use tracers which are labeled by radioactive isotopes to study the density of particular receptors or the metabolism and the regional cerebral blood flow (rCBF) in specific areas [45].

The study of Chun-Chieh Lin *et al.* [46] supports that the dopaminergic dysfunction can be associated with the pathophysiology of RLS. They tried to determine the diagnostic accuracy and potential of SPECT-TRODAT imaging so as to make a distinction between patients with RLS and normal individuals. All subjects were injected with a single dose of 740 MBp (20 mCi) of ^{99m}Tc-TODAT-1 and the brain images were acquired 3 to 4 hours after injection using a Hawk Eye dua-head γ-camera. The values that were taken into consideration included age in both groups, the Beck Depression Inventory (BDI) score which measures symptoms of depression and specific uptake ratio in the striatum, caudate and putamen. T-test was used to compare the mean values of uptake ratio in the striatum, caudate and putamen among RLS patients and healthy controls. The SPSS 13.0 software was used for all analysis and the scientists found that the root of the symptoms of RLS is the dysfunction of the striatum of the brain dopaminergic system.

Iron-sensitive MRI methods

There are also several MRI techniques that are used currently in use to measure non-heme iron content in brain tissue. Some of these iron-sensitive MRI methods are relaxometry methods measuring R1, R2, R2* or R', mapping of field-dependent transverse relaxation rate increase (FDRI), magnetic field correlation (MFC), phase imaging, susceptibility weighted imaging (SWI), direct saturation imaging, and the recently developed quantitative susceptibility mapping (QSM) [45].

Clinical studies reveal that there are low brain iron levels in substania nigra in patients with early onset RLS, probably due to a gene variant (btbd9) in the midbrain [47, 48]. Following the same line of thought, Hye-Jin Moon *et al.* [49] studied the iron content in several brain regions and particularly in the substantia nigra (SN) in early- and late-onset RLS patients which had been measured by T2 relaxometry using MRI. The authors tried to clarify the conflicting results of previous studies especially pertaining to the iron content in this brain region. They used strong magnet at 3.0 Tesla to obtain the iron index, as it is more sensitive to brain iron levels. A high resolution

three-dimensional spoiled gradient echo sequence, a spin-echo sequence and a gradient echo sampling of free induction decay and echo sequence were used to obtain structural imaging (T1-weighted images), T2 relaxometry and T2* relaxometry, respectively. The software that used was the ImageJ and the Medical Image Processing Analysis and Visualization. The first one was used to process and produce T2, T2*, R2 and R2* maps and the second to outline the regions of interest on the spin echo image. Because of the higher iron-related specificity of the R2' map, it was used as the 'iron index'. The statistical analysis included the Kolmogorov-Simon test to study the normality of distribution of the parameters, Analysis of covariance (ANCOVA) to compare the age-adjusted iron indexes of both groups (patients and control subjects) and partial correlation coefficient to explore the correlation between disease severity and iron index. The Pearson product-moment correlation coefficient was used to assess the intraobserver and interobserver variabilities on relaxation rate measurements. After the aforementioned stages of research, the disease duration was found to be significantly longer in the early-onset group than in the late-onset group. As for the mean iron index of the SN, scientists note that it was significantly lower in the late-onset RLS group than in the control group.

Recent research conducted by Xu Li *et al.* [50] suggests the use of quantitative susceptibility mapping (QSM) in order to determine regional brain iron concentrations in RLS and test the possible correlation between measured brain tissue magnetic susceptibility and RLS clinical features. It has been stated that previous studies which used relaxometry methods presented conflicting findings and a possible reason could be the different techniques used for measuring tissue iron contents with different sensitivities and methodological limitations. This is why they use the quantitative measurement of tissue magnetic susceptibility as a more accurate and specific measure of tissue iron content, especially in gray matter. More specifically, a group of thirty-nine patients with idiopathic RLS and another one with 29 age- and gender-matched healthy control subjects were scanned at 7 Tesla in order to qualify the magnetic susceptibilities in SN, thalamus, striatum and several iron-rich gray matter regions and compare them with related clinical measures. The first stage of the statistical analysis was a two-tailed t-test with unequal variance or Chi-Square as appropriate, which was used to test group differences in the clinical measurements between healthy controls and RLS patients. Subsequently, ANCOVA was used to determine possible differences in the brain iron content between groups and to conduct exploratory tests in the

secondary ROIs. Automated and fixed shape tracing were the tracing methods that were used to obtain the Pearson correlation between the susceptibility values in SN. The two tracing methods were tested on SWI high-pass filtered phase in order to suggest possible group difference between RLS and control and correlation between values. The last method of the statistical analysis was to determine Pearson partial correlations controlling on the subjects age and ROIs volume for the SN and then all other ROIs between quantitative magnetic susceptibility and other clinical measures. After this detailed analysis, the scientists assessed the possible existence of iron insufficiency in the dentate, as also in the thalamus, something that had not been noticed in previous studies. Compared to healthy controls, RLS patients did not show significant difference in the SN but the correlation between magnetic susceptibility in SN and the periodic limb movement during sleep measure was noteworthy.

MRS

Another noninvasive method that has been used in the investigation of RLS is the Proton Magnetic Resonance Spectroscopy (^{1}H-MRS) that permits measurement of the concentration of specific biochemical compounds in the brain. There is the possibility, as this is a method that provides a spectrum rather than an image, to quantify spectra of many biologically important metabolites [44].

Proton magnetic resonance spectroscopy (^{1}H-MRS) has revealed 50% greater thalamic glutamate and reduced neuronal marker N-acetyl aspartate (NAA) in the thalamus. Wickermann *et al.* [51] focused on the quantification of gamma-aminobutyric acid (GABA) levels which are the major central nervous system (CNS) inhibitory neurotransmitter, as well as on the levels of glutamate and NAA in the anterior cingulate cortex (ACC), thalamus and cerebellum concerning patients with RLS and matched controls. These transmitters/metabolites levels correlated to RLS severity and to objective measures of sleep and leg movement activity. This study differs from previous studies as there were no other reports assessing, levels of GABA in RLS patients. All the subjects underwent various medical examinations and tests involving questionnaires all of which took place two days before the actual examination, in order to be considered as a reliable dataset. In order to assess Periodic limb movements during sleep (PLMS), Actigraphy was performed on the night before scans. Imaging and spectroscopy were conducted on a 4 Tesla MRI scanner at McLean Hospital in Belmont, MA, USA. Analysis of variance (ANOVA) with groups and brain

regions as independent factors was the main statistical analysis. In order to examine differences and similarities between groups uncorrected post hoc t-test were used. Unpaired *t*-tests (two-sided) were performed as a means to compare voxel tissue composition, demographics, psychometric scores, and diary/actigraphic data between groups. GABA levels with the IRLSSG severity scale for the five days before scanning, RLS discomfort scores during the MRI, PSG-related sleep measures, sleep and RLS diaries for the two days before MRS scans, and PSG and actigraphy-related leg movement measures were correlated and constituted the secondary analysis. Statistical analysis was realised through the use of SPSS (Version 21) software. Levels of GABA, glutamate and NAA showed similarities between RLS and control subjects in the three voxels of interest. On the other hand, GABA levels present a positive correlation with both PLM indices and RLS severity in the thalamus and negative correlation with both of these measures in the cerebellum in RLS subjects. Moreover, the values of NAA of the ACC were higher in RLS than in controls groups. The study concluded that their preliminary data indicates that known cerebellar–thalamic interactions may modulate the intensity of RLS sensory and motor symptoms. Furthermore, anterior cingulate cortex may be related to affected components of the painful symptoms of RLS.

Volumetric MRI

A number of methods using high-resolution 3D T1-weighted MRI scans, have been developed in the last decade in order to measure progressive brain atrophy as it is an important feature of many central nervous system (CNS) disorders, including not only neurodegenerative diseases but also inflammatory conditions. Voxel based morphometry (VBM) has the ability to find subtle volume changes in the human brain by comparing the regional attenuation of brain gray matter and white matter intensity across groups of subjects, voxel-by-voxel. The reliability and reproducibility of the results, as well as time saving, are among the advantages of VBM in comparison to older approaches. Moreover, VBM allows for the exploration of the entire brain as a whole, as there is no requirement of a priori hypothesis of the location of group differences [44]. The work of Yongmin Chang *et al.* [7] was based on the demonstration of whether or not restless legs syndrome is associated with any morphological change in gray matter. Equal numbers of RLS and controls were scanned in a 3.0 T MRI scanner and three-dimensional anatomical MRI were acquired using a T1-weighted 3D spoiled gradient recalled sequence, because of the high

resolution and good contrast between gray and white matter structure that this sequence provides for the VBM. The existence of structural changes of gray matter throughout the whole brain was examined with the use of the general linear model (GLM). They extracted their conclusions using a whole brain-based statistical approach instead of a region of interest (ROI)-based method. This approach outweighs in comparison to ROIs-method as it is free from any a priori hypotheses and the pathology of RLS cannot be hypothesized to certain brain regions. The comparison of brain morphology for age- and gender-matched pair from two groups was achieved by an independent t-test. Partial correlation analysis controlling age and gender was used to investigate the relation of any significantly reduced volume in ROIs to clinical variables and assess the association between the RLS patient's voxel-based volumes of the entire brain and clinical variables. After the comparison between RLS and controls subjects, significant regional decreases of GM volume in the left hippocampal gyrus, both parietal lobes, medial frontal areas, lateral temporal areas and cerebellum were found. It was also found that the disease duration and severity of symptoms could be related to the alternation of the brain structure, a fact that requires further investigation.

Diffusion tensor MRI and structural connectivity

The neuroscientists stress that a great challenge is to understand brain function in terms of connectional anatomy and the dynamic flow of information across neuron networks. Unique biological and clinical information can be provided from the MR measurement of an effective diffusion tensor of water in tissues, a fact that is not achievable by other imaging modalities. Diffusion tensor imaging is an MRI modality which is a strong method for white matter architecture research [52]. Diffusion is the random thermal movement of water molecules (Brownian motion) in neural tissue and DTI has the ability to determine quantitative measures of brain microstructure. The diffusion characteristics that can be measured using the tensor model, by means of diffusivity (MD) and degree of anisotropy are shown by fractional anisotropy. The linear structure of WM tracts, which enables the free diffuse of water molecules along the axons but prevents their diffusion perpendicularly to the axonal main direction due to the myelin existence, features an anisotropic diffusion. Various methods that have been used to analyze DTI data utilized region of interest (ROI)-based approaches or voxel-wise a priori hypothesis free approaches which is currently using tract-based spatial statistics (TBSS) as a procedure method. Additionally, reconstruction of WM tracts, which

physically connect the different brain regions can be considered as another method in order to study DTI data. The DTI tractography algorithms have a supporting role in those studies.

In their attempt to explore the possible alternation of the reliability of brain white matter in RLS patients, Yongmin Chang *et al.* [53] used 22 RLS patients and 22 age-matched healthy control subjects. An eight-channel phased-array head coil in a 3.0 T MR imaging system was used to acquire the data. Fractional anisotropy (FA), axial and radial diffusivities (AD and RD) were calculated using the Statistical Parametric Mapping (SPM5) software. This software package was also used for the preprocessing of the images. A two-sample t-test was used to examine group differences in FA, AD, and RD for each voxel across the WM of the whole brain between RLS and control subjects. Correlation analysis was implemented in RLS subjects between FA, AD, and RD at each ROI of an individual patient and by using the simple regression function in SPM5 in order to quantify clinical measures that included disease severity assessed with K-IRLS scores and illness duration. The whole brain voxel-based DTI analysis indicated significantly decreased FA in the genu of the corpus callosum, putamen and the frontal gyrus in RLS subjects compared with the control group. Focusing on the regions that had shown the lower FA, it was pointed out that there were higher AD and RD in RLS patients. A conclusion was the positive correlation of the frontal WM adjacent to the inferior frontal gyrus with the K-IRLS score.

fMRI and functional connectivity

fMRI uses either T2* in a gradient echo sequence, or T2 in a spin echo sequence to measure neuronal activity modifications of the transverse magnetization time associated to the BOLD mechanism. Resting state fMRI is the most common technique to investigate functional connectivity by MRI. Functional connectivity can be assessed by measuring the level of co-activation of resting state fMRI time-series between brain regions. There are model-dependent and model free methods that are used to the data processing in order to extract the functional connectivity of the brain. These methods will be presented in detail below through recent medical studies.

The study of Chunyan Liu *et al.* [54] had two main objectives. First, they tried to compare the brain activity between normal people and idiopathic RLS patients during asymptomatic periods; and second to estimate the effect of the repetitive transcranial magnetic stimulation (rTMS) in specific cortical regions concerning the reverse of any

observed differences in brain activity and the alleviation of patients' symptoms. Fifteen idiopathic RLS patients and fourteen age- and gender-matched healthy controls participated in the study, after they had undergone medical examination and clinical interviews. Functional MRI images were acquired from a Siemens Trio 3.0 T scanner, during the daytime, axially, using an echo-planar imaging (EPI) sequence and also three-dimensional T1-weighted magnetization-prepared rapid gradient echo (MPRAGE) sagittal images were collected. Statistical Parametric Mapping (SPM8) and Data Processing Assistant for Resting-State fMRI (DPARSF) were used for image preprocessing. The Resting-State fMRI Analysis Toolkit (REST) was used in order to calculate the amplitude of low-frequency fluctuations (ALFF). Voxelwise general linear model (GLM) analysis was performed in order to study between-group differences in ALFF, with age and gender as covariates. Using SPM8 the generation of a GM mask by thresholding an a priori gray matter probability map was achieved and the AFNI Alpha Sim program supports the Monte Carlo simulations performing. This GM mask generation included of the correction for multiple comparisons. Regarding the examination of within-group differences for the effect of rTMS, a paired t-test was conducted in order to find changes in the ALFF before and after rTMS treatment. The comparisons that were examined in the current study involved the ALFF between RLS patients and control groups, the ALFF between the drug-naïve RLS patient and control groups, the ALFF between RLS patients before rTMS treatment and healthy controls, the ALFF values between RLS patients after rTMS treatment and healthy controls, as well as the changes in ALFF values after rTMS treatment and the changes in IRLSSG score after rTMS treatment. The ALFF values were found to be lower in the sensorimotor system, including the paracentral lobule, precuneus, superior parietal gyrus, supplementary motor area (SMA), right precentral gyrus and right post-central gyrus, as well as in the visual processing system, including middle occipital gyrus, calcarine sulcus, cuneus, fusiform gyrus and right inferior temporal gyrus. The ALFF was found to be higher in the insula, parahippocampal and hippocampal gyri, inferior frontal gyrus, rectus, left inferior parietal gyrus, left superior parietal gyrus left angular gyrus and brainstem. These results were maintained only when drug-naive patients were considered. The values of ALFF in several sensorimotor and visual regions were increased after rTMS treatment and the IRLSSG Rating Scale had lower values presenting improved RLS symptoms. These results supply innovate knowledge

into RLS pathophysiology and propose a potential mechanism for rTMS therapy in idiopathic RLS patients.

The objective of the research of Jeonghun Ku *et al.* [6] was to examine the intrinsic changes in the thalamocortical circuit in RLS patients through a resting-state fMRI study. The MRI data was obtained using a 3T MRI Signa Excite scanner with an 8-channel high-resolution brain coil. The anatomical image series of each participant was acquired with the use of 3D spoiled gradient-echo sequence and a gradient echo planar imaging sequence was used to collect functional images. A seed-based method was used to measure the resting-state connectivity. Analysis of Functional Neuroimages (AFNI) and FMRIB Software Library (FSL) were both used for the preprocessing of fMRI data. The preprocessing included slice-timing correction, despiking, 3D motion correction, temporal normalizing, linear and quadratic detrending, spatial normalization, spatial smoothing and temporal filtering. The target region of interest was assumed as the bilateral ventroposterolateral nuclei (VPLN) in the thalamus. EdDeconvole (AFNI) was used for each subject, to derive whole-brain voxel-wise corrections associated with the mean time-series for the left and right VPLN. Each subject's correlation maps were converted to z score maps and they were included in the group analysis. T-tests were used to compare the connectivity strength of controls and patients and obtain the contrast map. The K-IRLS severity scale as measure of disease burden was taken into consideration in order to carry out a correlation analysis for the examination of the networks that are related with subjective symptom severity. The research led to several important results regarding the functional connectivity of the brain. During the asymptomatic period, the RLS group confirmed reduced thalamic connectivity in the right parahippocampal gyrus, right precuneus, right precentral gyrus, and bilateral lingual gyri. On the other hand, an increase in thalamic connectivity of the right superior temporal gyrus, bilateral middle temporal gyrus, and right medial frontal gyrus were indicated. Additionally, the connectivity between the thalamus and right parahippocampal gyrus in relation to RLS severity score presented a negative correlation.

Another study that focused on the resting-state functional connectivity of the brain in the restless legs syndrome was conducted by another research team that Jeonhum Ku *et al.* [5] led two years later. They focused their attention on the investigation of changes in the default mode network in RLS subjects. An equal number of patients with drug-naive idiopathic RLS and age- and gender-matched healthy subjects

participated in the study. Resting-state fMRI data was collected by a 3T MRI Signa Excite scanner with an eight-channel high-resolution brain coil. 3D spoiled gradient-echo sequence was used to obtain anatomic image series and a gradient echo planar imaging (EPI) sequence to collect functional images. AFNI software was used in order to process resting-state fMRI data. For the purpose of extracting the DMN from the resting-state fMRI, several steps of seed-based resting-state connectivity analysis to reduce seed-selection bias were followed. The first seed region was marked within the posterior cingulate cortex and the second within the medial prefrontal cortex. The 3dDeconvolve (AFNI) was used to compute the whole brain voxel-wise correlations that are associated with the mean time-series for each seed region. Fisher's r-to-z transformation were used to convert correlation maps and two binary maps of the DMN were generated after the application of one-sample t-test across subjects. An independent t-test was used in order to find out group differences in the DMN for controls and RLS patients. With the use of Pearson correlation, an inter-regional correlation analysis was carried out with the averaged strength of connectivity from each brain region. The last step of statistical analysis was the comparison of the strength of connectivity from each brain region with the patient's characteristics of symptom duration, age of onset, K-IRLS total and subscores of K-IRLS. The results indicated abnormalities of the DMN in RLS subjects that affect the thalamic relay sensory-motor-associated circuit. More specifically, the reduced DNM connectivity was found in the left posterior cingulate cortex, the right orbito-frontal gyrus, the left precuneus, and the right subcallosal gyrus of the RLS subjects. The DMN connectivity was enhanced in sensory-motor-associated circuits including the right superior parietal lobule, the right supplementary motor area, and the left thalamus. Also, negative correlation was observed between DMN and thalamus and in the connectivity between the orbito-frontal gyrus and the subcallosal gyrus in the subject.

Connectomics

Based on the newest developments in MRI analysis techniques, the chance to investigate the total structure and function of the brain network by the use of graph analytical methods has emerged. Graph theory techniques can be employed not only on functional but also on structural MRI. First, the determination of the brain network nodes is required and the so-called edges constitute the connections between regions. The connectivity between each pair of nodes is determined as the correlation coefficient

of their BOLD fluctuations. Centrality, clustering, efficiency, hierarchy, hubs, modularity, robustness, small-worldness and synchronizability are several organizational and topological properties that can be studied through the graphs.

Based on the aforementioned method, Jeong Woo Choi *et al.* [55] tried in their study to find abnormal cortical activity during sleep in RLS patients and to clarify the role of treatment with a dopamine agonist. Specifically, a whole-brain electroencephalography was used in order to investigate alternations of functional networks, the spectral power of neural activity during sleep in RLS patients and to verify the involvement of pramipexole treatment on the reverse of changes. Twelve drug-naive RLS subjects and sixteen age-matched healthy controls were involved in the study. Overnight polysomnography was used in two stages. The first recording took place immediately before providing the first dose of pramipexole and the second recording took place 12–16 weeks after beginning pramipexole administration. The spectral power and interregional phase synchrony were assessed in 30-s epochs. Graph-theory measures were used to quantify the functional characteristics of the cortical network. The delta-band power was significantly enhanced and the small-world network characteristics in the delta band were interrupted in RLS patients in comparison to the healthy controls. Dopaminergic medication was applied for the successful treatment of these disturbances. The RLS severity score in the RLS patients before treatment presented a significant correlation with the delta-band power.

Combining imaging techniques

Except for the methods that were previously presented and that used individual imaging techniques in order to investigate the restless legs syndrome, important studies have been recorded that use a combination of imaging techniques and lead to a better understanding of the disease. Several of them have led to useful findings and are presented in detail below.

In research conducted by Yaoyao Zhuo *et al.* [56], a combination of diffusion tensor imaging (DTI) and regional homogeneity (ReHo) was achieved to examine the changes in the regional spontaneous brain activity changes for RLS patients and healthy controls subjects. The MR acquisition was carried out on a 3T GE Signa MR scanner with an eight-channel phased array head coil during evening hours. Echo planar imaging (EPI) sequence was used to obtain resting-state fMRI images and also craniocerebral routine sagittal T1-weighted imaging and axial T2-FLAIR scanning were performed. SPM8

was used to implement the preprocessing steps including slice-timing and head motion correction, spatial normalization, spatial smoothing and temporal bandbass filtering. The DPARSF software was used in order to analyse the ReHo between one voxel and its nearest time-series. Kendall's coefficient of concordance (ReHo value) measured the resemblance of a voxel and its nearest neighbors, which indicates the synchronicity of brain activity. FSL software was used to perform DTI data post-preprocessing and statistical analysis. The absence of non-brain tissue in DTI-EPI and the estimation of skull surface were achieved with the use of Brain Extraction Tool (BET). Eddy Current Correction in FMRIB's Diffusion Toolbox (FDT) was used for the correction of distortions due to the gradient directions. DTIFIT supports the local fitting of diffusion tensors and to extract parameter maps for FA and MD. Regarding the statistical analysis, Student's t-test was performed in order to compare the ages in the two groups and Chi-squared test to analyze groups' genders. Statistical analysis was achieved by the Statistical Analysis System (SAS) 8.0 software. Two sample t-test compared the ReHo values between RLS and normal control subjects and an intra-class one sample t-test to measure the reliability of ReHo values. AlphaSim program in AFNI was used for multiple comparison correction to control the false-positive rate. Tract-Based Spatial Statistics (TBSS) was the toolbox to analyze DTI data. After comparing RLS and normal controls group according to the morphological abnormalities in the conventional T1- and T2-weighted images, the results did not lead to their existence. Significant differences between groups regarding age or gender were not recorded. Considering the results that have emerged from the resting-state fMRI study and the one sample t-test, enhanced ReHo was found in the bilateral in the bilateral posterior cingulate/precuneus cortex compared to the groups' global means, showing that the default mode network was at rest. Cluster size in RLS group was found to be smaller than that of the control subjects group. The two-sample t-test led to increased ReHo in the RLS group in the bilateral middle frontal gyrus, anterior cingulate cortex, caudate nucleus, insula, thalamus, putamen and left posterior cingulate cortex compared to the normal controls group. No significant differences were found between groups according to the results of the DTI statistical analysis and likewise there were no differences observed in TBSS comparison in FA or mean diffusivity (MD) of any brain region.

Last but not the least, P. Margariti *et al.* [48] in their extensive study estimated the volume, iron content and activation of the brain during night-time episodes of sensory

leg discomfort and periodic limb movement in patients with early onset RLS. Imaging was carried out by the use of 1.5 T MRI scanner after 9.00 pm. According to the structural and functional imaging a T1-weighted high-resolution spoiled gradient echo sequence and a single-shot multisection gradient EPI were used respectively. T2 relaxometry was achieved by a multisection spin-echo T2-weighted sequence. The study included a self-evoked event related fMRI and the PLM episodes were monitored by a technologist. T1-weighted images were used for the voxel-based morphometry method using unified segmentation approach. An independent-samples t-test at the voxel level was used to evaluate morphological differences between eRLS patients and control subjects. Two different contrasts corresponding to increase or decrease of brain volume in the GM and WM compartments were the compared issues between patients and control subjects. The off-line processing of T2 relaxometry images was performed in Matlab 7.6 and the Levenberg-Marquardt optimization method was the mean to produce a T2 map by a pixel-by-pixel fitting procedure. The region-of-interest function of the previous method estimates the T2 relaxation time of the putamen, caudate nucleus, globus pallidus external and internal substantia nigra pars compacta and reticulata, STN, red nucleus and locus coeruleus. Statistical Parametric Mapping (SPM8) were used to utilize preprocessing of fMRI data including realignment, temporal and spatial correction, coregistration with high resolution anatomic image, normalization with the MNI template and smoothing by using a Gaussian Kernel. First-level analysis was performed to model monitored PLMs of each patient and second-level random-effect analysis to determine the activated areas within the group. The output of the analysis was an activation map and the parameters that were computed were the size, maximum z score of activated regions and corresponding P values. The evaluation of age determination on disease duration was conducted by Multiple linear regressors analysis. Regional brain volume change in patients did not exist but decreased T2 relaxation time was found in right globus pallidus internal and the STN, a fact that indicates enhanced iron content. The areas that reveal enhanced activation were in the left hemisphere, including the primary motor and somatosensory cortex, the thalamus, the pars opercularis, the ventral anterior cingulum and in the right hemisphere included the striatum, the inferior and superior parietal lobules and the dorsolateral prefrontal cortex. Also, bilateral activations were found in cerebellum, the midbrain and pons.

3.2 An overview on literature methods

An overview on literature methods is presented in the following table (Table 3.1).

Table 3.1: An overview on litearture methods.

Author	Dataset	Imaging technique	Statistical Analysis	Results
Chun-Chieh Lin *et al.* 2016 [46]	22 early-onset RLS 12 controls	^{99m}Tc-TRODAT-1 SPECT	SPSS 13.0 Voxel-based Analysis	Significantly reduced uptake in striatal dopamine transporter density and activity. Striatum dopamine transporter destiny was more impaired in patients with RLS disease.
Hye-Jin Moon *et al.* 2013 [49]	20 early-onset RLS 17 late-onset RLS 40 controls	T2 Relaxometry using 3.0 Tesla MRI	Analysis of covariance (ANCOVA) Partial correlation coefficient Pearson product-moment correlation coefficient	Lower iron index in the SN in patients with late-onset RLS.
Xu Li *et al.* 2016 [50]	39 RLS 29 controls	7.0 Tesla Quantitative Magnetic Susceptibility	Two tailed t-test Analysis of covariance (ANCOVA) Pearson correlations	Decreased magnetic susceptibility in the thalamus and dentate nucleus.
Wickermann *et al.* 2014 [51]	18 RLS 18 controls	4.0 Tesla proton magnetic resonance spectroscopy ^{1}H-MRS	SPSS 21.0 Analysis of variance (ANOVA) uncorrected post hoc t-tests unpaired two-sided t-test	Positive correlation between GABA levels and PLM and RLS severity. Higher NAA levels in the ACC in RLS.
Yongmin Chang *et al.* 2015 [7]	46 RLS 46 controls	3.0 Tesla MRI	SPM8 voxel-based morphometry analysis	Reduced volume in the left hippocampal gyrus, both parietal lobes, medial frontal areas, lateral temporal areas and cerebellum.
Yongmin Chang *et al.* 2014 [53]	22 RLS 22 controls	3.0 Tesla MRI DTI	SPM5 Voxel-based analysis Two sample t-test Correlation Analysis	Decreased FA in the genu of the corpus callosum and frontal WM adjacent to the inferior frontal gyrus Higher AD and RD in RLS in areas of decreases FA.

Author	Dataset	Imaging technique	Statistical Analysis	Results
Chunyan Liu *et al.* 2015 [54]	15 RLS (9 drug-naïve RLS) 14 controls	Resting-state fMRI	SPM8 Voxel wise general linear model (GLM) analysis Paired t-test	Lower ALFF in the sensorimotor and visual processing regions, and higher ALFF in the insula, parahippocampal and hippocampal gyri, left posterior parietal areas, and brainstem in RLS patients. Increased ALFF in several sensorimotor and visual regions and decreased IRLSSG Rating Scale scores, after rTMS treatment.
Jeonghun Ku *et al.* 2014 [6]	25 RLS 25 controls	Resting-state fMRI	AFNI Seed-based analysis t-tests Correlation analysis	Reduced thalamic connectivity with the right parahippocampal gyrus, right precuneus, right precentral gyrus, and bilateral lingual gyri. Enhanced thalamic connectivity with the right superior temporal gyrus, bilateral middle temporal gyrus, and right medial frontal gyrus.
Jeonhum Ku *et al.* 2016 [5]	16 drug-naïve RLS 16 controls	Resting-state fMRI	AFNI Seed-based analysis whole brain voxel-wise correlation analysis	Reduced DMN connectivity in the left posterior cingulate cortex, the right orbito-frontal gyrus, the left precuneus, and the right subcallosal gyrus of the RLS subjects. Increased DMN connectivity in sensory-motor-associated circuits including the right superior parietal lobule, the right supplementary motor area, and the left thalamus.
Jeong Woo Choi *et al.* 2017 [55]	12 drug-naïve RLS 16 controls	Polysomnography EEG	Graph-theory Analysis	Increased delta-band power and disrupted small-world network characteristics in the delta band in RLS patients. Significant correlation in delta-band power and RLS severity score in RLS patients before treatment.

Author	Dataset	Imaging technique	Statistical Analysis	Results
Yaoyao Zhuo *et al.* 2017 [56]	35 RLS 27 controls	DTI 3.0 Tesla MRI Resting-state fMRI	FSL and TBSS to measure FA or MD. SPM8 for data processing. DPARSF for ReHo calculation. AlphaSim program (AFNI) for multiple comparison correction and false-positive rate controlling.	Increased ReHo in the bilateral posterior ingulate/precuneus cortex compared to the groups' global means in both RLS and control groups. Increased ReHo in the bilateral middle frontal gyrus, anterior cingulate cortex, caudate nucleus, insula, thalamus, putamen and left posterior cingulate cortex in RLS group.
P. Margariti *et al.* 2012 [48]	11 unmedicated early-onset RLS 11 controls	1.5 Tesla MRI for Voxel-based Morphometry, T2 Relaxometry and Resting-state fMRI	Unified segmentation approach for voxel-based morphometry. Levenberg-Marquardt optimization method for T2 map production and unpaired two-tailed Student t-test for T2 relaxation time differences between groups. First level Analysis, Second level Analysis and Multiple linear regressor analysis in SPM5 for resting-state fMRI analysis.	Decreased T2 relaxation time in the right globus pallidus internal and the STN, indicating increased iron content. Activated areas in RLS patients: In the left hemisphere, the primary motor and somatosensory cortex, the thalamus, the pars opercularis, and the ventral anterior cingulum; and in the right hemisphere, the striatum, the inferior and superior parietal lobules, and the dorsolateral prefrontal cortex. Bilateral activation in the cerebellum, the midbrain, and the pons.

Chapter 4. Proposed methodology

4.1 Preprocessing of fMRI data

The raw data that is generated from MRI scanner does not remind one of a real image, but instead is 'k-space' data, which is a spatial frequency transformation of real-space. Fourier transformation is required in order to reconstruct the k-space data into real space and in this way the image may be viewed and analyzed [23]. As described in previous chapters, it is assumed that fMRI data consists of a three-dimensional matrix of volume elements (voxels) that should be repeatedly sampled over time, as efficient sampling of k-space is important [25]. So, a single experiment might give a brain volume of 64×64×22 (i.e. 90,112 voxels) where the BOLD signals are collected at T separate time points throughout the recording time, where T ranges between 100-2000 [57]. A straightforward way of analyzing such a dataset would allow for the extraction of the raw time course of each voxel and the evaluation of differences of each of these time courses to some hypothesis with the use of a test of significance. One of the assumptions resulting from this approach, claim that each voxel represents a unique and

fixed brain location and that a regular known rate is demanded for the sampling of the voxel to take place. Although these assumptions may seem reliable they aren't always accurate. However, subjects head motion, physiological oscillations like heart beats and respiration, inhomogeneities in the static field, and/or differences in the timing of image acquisition lead to spatial and temporal inaccuracy of all fMRI data. Their correction may reduce the detection power of an experiment.

For this reason, a series of computational procedures the so-called preprocessing steps are used to operate on fMRI data following image reconstruction before the statistical analysis. The major goals of preprocessing procedures are to measure and/or remove unwanted variability in fMRI data in order to improve experimental analyses as well as to prepare the data for statistical analysis [25].

To ensure an efficient fMRI paradigm the evoked neural activity produced by the stimulus or task should constitute a signal which can undergo all transformations which are essential for the preprocessing and statistical analysis stages. There are six preprocessing steps needed for the removal of the confounding effects of artifacts and the enhanchment of signal-to-noise ratio (SNR). These are the following: motion correction (realignment), slice-timing correction, coregistration, intensity normalization, spatial normalization and spatial smoothing [33].

4.1.1 Motion correction (Realignment)

The most severe artifacts, that realignment preprocessing step aims to correct the artifacts that are related to the movement. In several cases the movement is large and this is something that confounds the effects, so it is necessary to be discarded from the study. Due to the fact that head movement in the scanner cannot fully be eliminated, the mathematical transformations contribute effectively in the movement correction. The statistical results are affected by movement. There is a decrease in the estimation efficiency caused by the adding of the residual variation that causes various activation between adjacent voxels. Another way the movement may affect the results is if activations are correlated to the stimuli [58].

The best possible alignment between the input image and the target image is the first step in motion correction [57]. As a target image the first or the intermediate image volume is used. There is an assumption that only rigid body movement occurs according to the registration [33], so rigid body transformation involving 6 variable parameters is used. In order to achieve target image matching the input image is

translated (shifted in the *x*, *y* and *z* directions) and rotated (altered roll, pitch and yaw) [57]. The use of a cost function is necessary in order to determine the optimal value of parameters. Both its choice and optimization strategies affect the differences between registration algorithms.

Mathematically, a position $x=[x_1, x_2, x_3, 1]^T$ in image f is mapped to a position $y=[y_1, y_2, y_3, 1]^T$ in image g by rigid body transformation and is expressed by the following equation:

$$y=M*x, \tag{4.1}$$

where $M=M_f^{-1}M_tM_\theta M_\varphi M_\omega M_g$ is the transformation matrix.

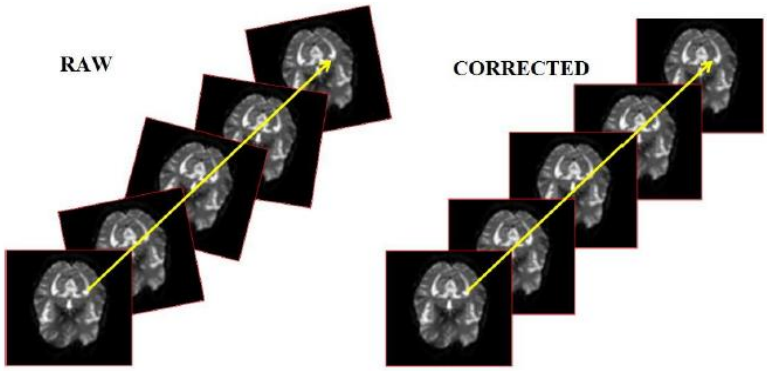

Figure 4.1: Motion correction [30].

Specifically, M_t is the matrix that implements the translations and the matrices $M_\theta, M_\varphi, M_\omega$ are the matrices that implement the rotations about the x, y, z axes, respectively. The M_f and M_g are the transformation matrices into Euclidian space for images f and g that are to be registered together. The matrices are given below:

$$M_t=\begin{bmatrix}1 & 0 & 0 & x_t\\ 0 & 1 & 0 & y_t\\ 0 & 0 & 1 & z_t\\ 0 & 0 & 0 & 1\end{bmatrix}, M_\theta=\begin{bmatrix}1 & 0 & 0 & 0\\ 0 & cos\,\theta & sin\,\theta & 0\\ 0 & -sin\,\theta & cos\,\theta & 0\\ 0 & 0 & 0 & 1\end{bmatrix},$$

$$M_\varphi=\begin{bmatrix}cos\,\omega & 0 & sin\,\omega & 0\\ -sin\,\omega & 0 & cos\,\omega & 0\\ 0 & 0 & 1 & 0\\ 0 & 0 & 0 & 1\end{bmatrix}, M_f=M_g=\begin{bmatrix}x_{mm} & 0 & 0 & -\frac{a}{2}x_{mm}\\ 0 & y_{mm} & & -\frac{b}{2}y_{mm}\\ 0 & 0 & z_{mm} & -\frac{c}{2}z_{mm}\\ 0 & 0 & 0 & 1\end{bmatrix}. \tag{4.2), (4.3), (4.4), (4.5}$$

Where x_{mm}, y_{mm}, z_{mm} are the voxel's dimensions and a, b, c the image's dimensions. The best possible fit for all j voxels between the two images f and g is obtained by minimizing the following equation and solving the parameters p:

$$l(p)=\sum_j (Mx_v - sy_v)^2, \tag{4.6}$$

where $p=[x_t, y_t, z_t, \theta, \varphi, \omega]^T$ is the parameter vector, v is the voxel and s the parameter that is used to offset the differences in voxel intensity of the two images [30, 58].

4.1.2 Slice-timing correction

Slice-timing is the second problem that causes inaccuracies in time-series and is related to the sequential collection of slices within each volume [59]. Two-dimensional pulse sequences are commonly used in most fMRI data acquisition that collect one slice a time, because of the spatial gradients existence that limit the influence of an excitation pulse to a single slice within the brain [25]. The acquisition order determines the scan time of an individual slice [33]. Interleaved slice acquisition is used by the most pulse sequences, avoiding cross-slice excitation by collecting all of the odd slices at first and secondly all of the even slices. For the less common ascending or descending sequential acquisitions, in which the slices are collected consecutively, the last slice is collected almost one TR after the first slice. On the other hand, in interleaved acquisitions, adjacent slices are collected a full TR/2 apart [25].

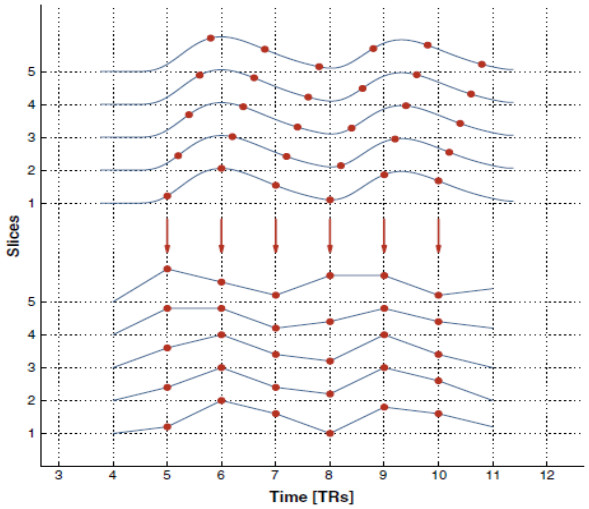

Figure 4.2: Illustration of slice-timing problem [60].

A problem that emerges is that the statistical analysis assumes that every voxel is sampled simultaneously. Thus, the goal of slice-timing correction is to shift each voxel's time course in order to be assumed as they were measured at exactly the same time point. For this reason, phase shifting of the sines that comprise of the signal should be performed. Also, each time-series of the voxels is transformed into the frequency domain, the data is performed to phase shifting and the inverse Fourier transform is used in order to achieve the corrected time-series recovery [33].

For each image volume that has q slices with m×n pixels (m is the number of the rows and n the number of columns), the following matrix is shaped:

$$A_{cq}=\begin{bmatrix} a_{11} & a_{12} & \dots \\ \vdots & \ddots & \vdots \\ a_{k1} & a_{k2} & \dots \end{bmatrix}. \quad (4.7)$$

Where c ranges between 1 and n (c=1,…,n) and the k expresses the time points. The element a_{ij} represents the intensity value of the voxel that is localized in slice q, specifically in line j, in column c, at a time point i. Therefore, the first column of the matrix expresses the time-series of the voxel (c, 1, q). The convolution is performed for each column of the matrix in frequency domain by using a shifting vector which depends on the TR, TA the number of slices and the acquisition order (ascending, descending or interleaved) [30].

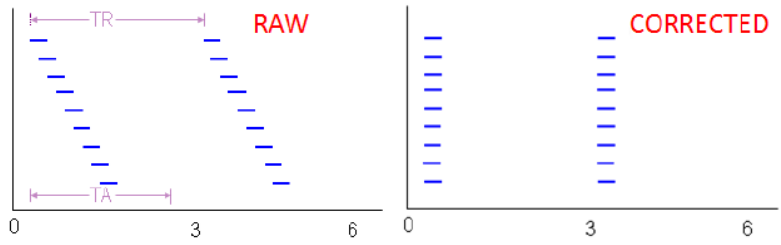

Figure 4.3: Slice-timing correction [30].

For data acquired using interleaved sequence at a long TR, slice-timing correction should be performed before the motion correction. On the other hand, if the data acquisition order is ascending or descending or with a short TR, the slice-timing correction should be performed after motion correction [25].

4.1.3 Co-registration

The brain activity causes changes in the fMRI signal which can be detected by fMRI's fast imaging methods, such as EPI, which however limits the quality and spatial resolution of the image. In order to estimate activated areas of functional images, their superimposing onto high-resolution image is required. The co-registration achieves the functional EPI volumes and the high-resolution anatomical image realignment, so that the anatomical structures match. This preprocessing step uses mutual information that measures the statistical dependence between two random variables or the amount of information that one variable contains about the other. Mutual information I (A, B) of the random variables A and B is defined in terms of entropy as shown below:

$$I\ (A,B)\ =\ h(A)+\ h(B)-\ h\ (A,B), \tag{4.8}$$

where h(A) and h(B) are the entropies of A and B respectively, and h (A, B) the joint entropy.

The geometric alignment of the images A and B is achieved when the I (A, B) is maximal and it is the mutual information criterion [58].

4.1.4 Intensity normalization

There is an additional scan-to-scan variance that emerges during fMRI experiment at very low spatial frequencies that can be possibly attributed to the scanner itself (scanner drift). This variation can be modeled and controlled by several global normalization approaches. This intensity normalization concerns the rescaling of all intensities in an fMRI volume by the same amount and is applied at each volume individually. In a common approach for intensity normalization, the first step is the calculation of the mean intensity across all voxels, for each fMRI volume, which have been at an intensity above a predetermined threshold. The rescaling of all intensity values by a constant value follows and the result is that the new mean intensity becomes a preset value. According to another approach, the usage of mean intensity value of each volume as confounding variables is demanded in order to be used in further statistical analysis. These methods include a drawback. In the case of strong activation, the result is the increase of the mean intensity, resulting in the negative correlation of the "non-activated" parts of the volume with the stimulation after normalization, which means that in the final statistical image it will be presented as "deactivation" [33].

4.1.5 Spatial normalization

The first reason why the spatial normalization is performed as a preprocessing step is because it enables the report of the activated locations according to well-known coordinates within a standard space. The most commonly used stereotactic spaces, in the field of neuroscience, that mention the locations of activations, are Talairach and Tournoux space or a space determined by Montreal Neurological Institute (MNI space). A large group of normal MRI scans are used in the MNI space definition, a fact that makes it more representative of the population in comparison with the Talairach and Tournoux atlas whose determination is based only on one person's brain. However, both atlases show similarities [58].

The ability to perform group analysis is the second reason why normalization is used. Each human brain is slightly different according to size, shape and in location of functional areas. It is necessary that every subject's brain be standardized into a same space so that functional areas of the subjects are located [33].

The determination of the optimum 12-parameter affine registration between the template and the image to be normalized, is the first step of the spatial normalization. The second one is the estimation of the nonlinear deformations determined by a linear combination of three-dimensional discrete cosine transform (DCT) basis functions [58]. A maximum a posteriori (MAP) approach is used for the determination of the optimum affine transformation. The affine transformation is expressed by:

$$y=M*x, \tag{4.9}$$

where $M=M_f^{-1}M_tM_\theta M_\varphi M_\omega M_z M_s M_g$. The M_z is the focus matrix and M_s is the shearing matrix. They are expressed as follows:

$$M_z=\begin{bmatrix} x_z & 0 & 0 & 0 \\ 0 & y_z & 0 & 0 \\ 0 & 0 & z_z & 0 \\ 0 & 0 & 0 & 1 \end{bmatrix},\ M_\theta=\begin{bmatrix} 1 & x_s & y_s & 0 \\ 0 & 1 & z_s & 0 \\ 0 & 0 & 1 & 0 \\ 0 & 0 & 0 & 1 \end{bmatrix}. \tag{4.10), (4.11}$$

The nonlinear deformations that emerge during the normalization preprocessing step are required to be estimated. A linear combination of basic functions, which are the lowest-frequency components of discrete cosine transform, is used so that distortion modeling be achieved. A linear combination of basic functions is given below:

$$y_i=x_i-\sum_j t_j\, b_j(x_i). \tag{4.12}$$

Where t_j is the jth coefficient describing translation for each three dimensions and $b_j(x_i)$ is the jth basic function at spatial position a_i [58].

4.1.6 Spatial smoothing

The increasing of SNR or in other words the reduction of noise without affecting the signal of interest, and the ensuring of reliable results from the statistical analysis, are the two fundamental reasons of spatial smoothing applying. The convolution of each volume with a Gaussian kernel is the most common approach for spatial smoothing [30, 33]. The amount of the image spatial smoothing depends on the full width half maximum (FWHM) (Fig. 4.4) [29]. The discrete convolution is described by the following equation:

$$t_i=\sum_{u=-d}^{d} h_{i-u}\, f_u, \tag{4.13}$$

where d is the kernel length, h is the kernel and f the image that undergoes spatial smoothing. The kernel amplitude A, at u units away from the center is defined by:

$A_u = \frac{e^{-\frac{u^2}{2rl^2}}}{\sqrt{2\pi rl^2}}$, where $rl = \frac{FWHM}{\sqrt{8 \ln 2}}$ and the FWHM is the full width at half maimum of the gaussian kernel. The most suggested FWHM for fMRI data is 2-3 times the voxel size of the functional images.

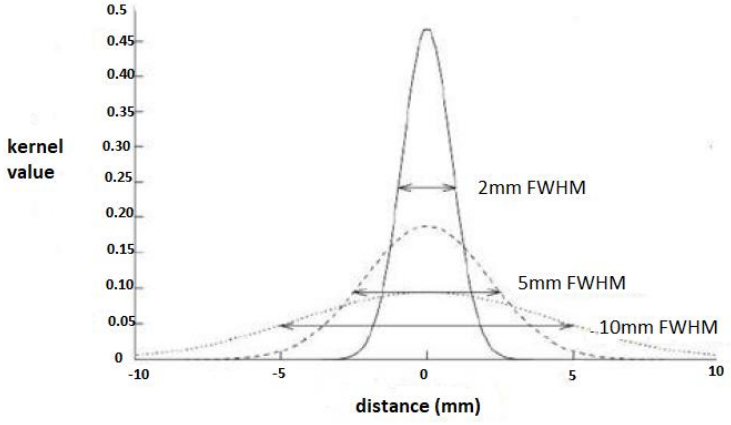

Figure 4.4: Width of Gaussian kernel [30].

4.2 Brain Connectivity

4.2.1 Functional organization and brain connectivity

A long-lasting debate in the field of neuroscience focuses on the localization of brain function. More specifically, it relates to whether specific mental functions are localized to specific brain regions or they rely more diffusely upon the entire brain instead. Frank Gall and the phrenologists were the first to study the concept of localization and focused on the shape of the skull in order to localize mental functions in specific brain regions. Gall's assumptions about how the skull relates to the brain were discarded by phrenology, despite being an outstanding neuroscientist. In the early twentieth century, research revealing that cortical lesions in rats affected their behavior globally led to an argument against localization of function. Later, during the twentieth century most neuroscientists agreed that localization of mental function exist to some point. Moreover, in order to achieve coherent mental function and behavior, the function of each of these regions must be integrated [29]. These fundamental approaches which are related to the brain organization are known as functional segregation and functional integration [61]. The first notion implies that a certain cortical area is responsible for some aspects of perceptual or motor processing. While the latter notion supports that many specialized areas are functionally integrated [62]. Nowadays, most neuroimaging

studies concentrate on functional localization, which is a more general concept than functional segregation. On the other hand, functional integration should be taken into account, so that brain function can be fully explained [29]. The integration within and between functionally specialized areas is described by functional or effective connectivity [61].

Brain connectivity defines the relationship between brain regions which may be anatomically different, spatially close or distant and are connected either structurally via neuronal axons or functionally via spontaneous intrinsic synchronization [63]. There are three different though related forms of connectivity that are related to brain connectivity analysis. These are anatomical or structural, functional and effective connectivity, which are described in detail below [64].

4.2.2 Structural connectivity

Concerning the first type of brain connectivity, anatomical or structural connectivity forms the connectome through synaptic contacts between neighboring neurons or fiber tracks connecting neuron pools in spatially distant brain regions. These fiber tracks in the brain compose of the so-called white matter. Anatomical connections present persistence and stability on short time scales. While substantial plasticity may be observed for longer time scales [64].

Advanced diffusion magnetic resonance imaging schemes can in detail depict in vivo the complex structural organization of the white matter of the brain [65]. The characterization of microscopic tissue properties and rendering the local direction can be accomplished by DTI, which measures the water diffusion tensor with the use of diffusion weighted pulse sequences as they are sensitive to the random water motion in microscopic level [63, 66]. Water molecules in the brain are continually moving and this motion is the so-called Brownian motion, as a result of unpredictable, thermally driven molecular collisions [67, 68]. Based on the criterion of whether motion is constrained or not, we are led to two characterizations of the diffusion. Deep in brain, in vertices, which are large spaces filled with fluid, motion is not restricted and this characterizes the diffusion as isotropic which means that it occurs in all directions in equal and random rate. In contrast, in white matter tracts where motion is constrained, that is the motion prevails towards one direction than another, the diffusion is anisotropic [67]. A severe limitation of these methods, however, is their low spatial resolution [64]. This phenomenon is portrayed below in Fig. 4.5.

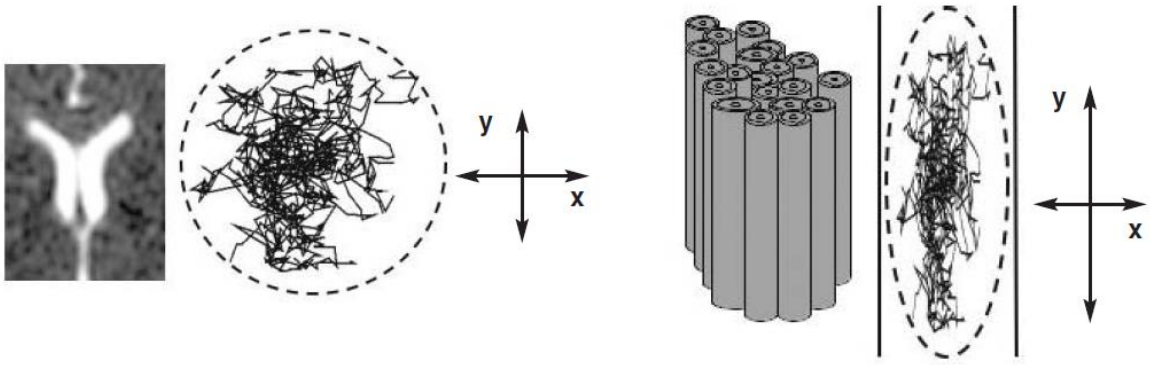

Figure 4.5: Isotropic and anisotropic diffusion [67].

The pattern of water diffusion occurring in a given voxel can be effectively described by a three-dimensional shape reconstructed by estimating the distance in which water diffuses in a given voxel, in a certain amount of time, for at least six noncollinear directions. The pattern of diffusion is usually modeled with the shape of an ellipsoid that makes available information concerning the diffusion properties and as a result the brain tissue microstructure.

Fractional anisotropy (FA), mean diffusivity (MD) and Mode are three of the most frequent diffusivity indicators, that have been studied in the DTI literature. FA is a measure of the sphericity of the diffusion ellipsoid. FA can diversify between value of zero which reflects a perfect spherical diffusion and the value of one which reflects a complete aspherical (linear) diffusion. In the event of a reduced FA in the WM there is probably damage to the axon membrane and reduction in axonal myelination, axonal packing density and/or axonal coherence. On the other hand, an increased value of FA is likely to show supranormal levels of myelination or axonal sprouting. The average displacement of water molecules because of diffusion in a given amount of time which is described by the diffusion ellipsoid volume, determines the MD. In tissues where there are few impediments to water diffusion (e.g., CSF) the MD value is highest, while in tissues where diffusion is constrained in at least one direction the MD value is lowest. The third index, Mode, provides more information in terms of the 3D shape of the diffusion ellipsoid in comparison to that given by FA. In other words, Mode shows if the diffusion ellipsoid is shaped like a cylinder (having high "tubular" anisotropy) or like a disk (having high "planar" anisotropy), for a certain FA value [68].

DTI fiber tracking

The aim of DTI fiber tracking is to define intervoxel connectivity based on the anisotropic diffusion of water. The diffusion tensor of each voxel is used by fiber tracking in order to follow an axonal tract in three-dimensions from voxel to voxel through the human brain. DTI provides only microstructural information at relatively low spatial resolution. This is the reason why DTI fiber tracking might be frequently applied in combination with functional and/or higher resolution anatomic information in order to clarify specific pathways. Consequently, 3D DTI tractography has opened a window to the noninvasive human neuroanatomy depiction [69].

The use of DTI has been recommended for a number of methods which aim to tract the fibers within the WM. There are two broad categories, the deterministic and the probabilistic which include methods of reconstruction WM tracts. Line propagation algorithms using local tensor information for each step of propagation are the characteristic of the first category [66]. A deterministic method which initiates fiber trajectories from user-defined voxel is Fiber Assignment by Continuous Tracking (FACT, Fig. 4.6) [69]. The main feature of the method in the second category is the global energy minimization which detects a path between two predetermined voxels with minimum energy violation. Probabilistic methods are effective in particular for tracking fibers in areas of lower anisotropy, not excepting gray matter [66].

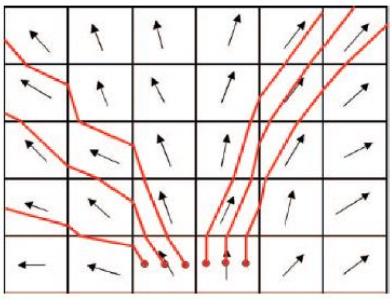

Figure 4.6: Schematic representation of the FACT algorithm. Arrows symbolize eigenvectors in each voxel and red lines the FACT trajectories [69].

4.2.3 Functional connectivity

In neuroimaging time-series analysis, functional connectivity is defined as the temporal correlations between spatially remote neurophysiological events. This definition gives a simple description of functional interactions. Functional connectivity only provides information about the observed correlation without explaining how these correlations are mediated [23].

Therefore, the notion of functional connectivity is in essence statistical as it depends on statistical measures as correlation, covariance, spectral coherence, or phase locking. Statistical dependencies greatly rely on time and vary between a range of milliseconds and seconds. As a result, the correlated activities within brain networks can be concluded with the use of neuroimaging modalities like fMRI, EEG, MEG, PET and SPECT which are some of the most commonly used techniques. The fMRI is the most important modality which studies the blood oxygen-level-dependent (BOLD) signal of the fMRI data. In this sense, functional connectivity concerns the temporal correlation between fluctuations in the BOLD signal of individual brain areas [64].

As it was aforementioned, functional connectivity analysis of fMRI data aims to estimate measures of similarities between the BOLD signals generated from different anatomy regions in order to assess the level of their synchronization [70]. The correlation of activity in brain regions which are not necessarily close to one another, can be caused by different reasons, so the results from functional connectivity analyses should carefully be studied. A description of different ways in which correlated activity between two regions A and B can occur is presented in Fig. 4.7.

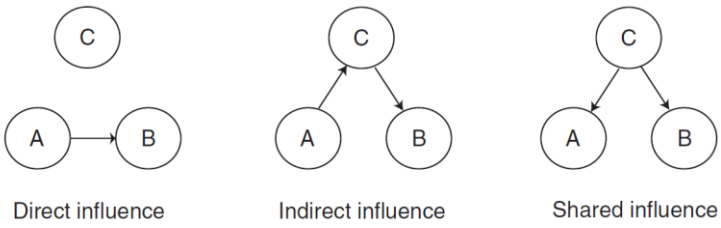

Figure 4.7: Direct influence (left panel), indirect influence through different area (center panel) and shared influence of a common input region (right panel) [29].

First, a misunderstanding could emerge, in the occurrence of a direct influence of one region on another as this does not refer to functional connectivity but to effective connectivity which is described in detail in the next chapter. In other words, the signal along connection between two regions one of which sends efferent connections to the other one can be interpreted as correlated activity. The inference of another region that is mediated by a third region or a common input to both regions could also cause the same problem. Here the problem of stimulus-driven transients is implied. Specifically, in the case of common input reception by two different regions from the visual cortex, the presentation of visual stimuli can cause correlated activity between them, even if they do not directly influence one another. To be noticed, only in the first case does functional connectivity reflect a direct causal influence between regions [29].

There is a basic discrimination between the two methods used for fMRI functional connectivity analysis. The first category includes model-based methods and the second one data-driven methods [70].

4.2.3.1 Model-based functional connectivity analysis

These model-based methods include the definition of some regions of interest (ROIs) which are usually named "seeds" and the hypothesis whether other regions are connected to these seeds by defining certain metrics, leading to the generation of the connectivity map of the human brain. These methods are based on prior neuroscience knowledge or experience as they require a priori selection of a voxel, cluster or atlas region from which the extraction of time-series can be accomplished. Subsequently, this data is assumed as a regressor in a linear correlation analysis or in a general linear model (GLM) analysis, in order to calculate whole-brain, voxel-wise functional connectivity maps of covariance with the seed region. The data in each voxel is regressed against the 'model' separately from every other voxel and this is included in univariate analysis methods [28, 71].

Connectivity measurements metrics determine the discrimination among model-based functional connectivity methods in cross-correlation analysis, coherence analysis and statistical parametric mapping [28].

Cross-correlation analysis

Cross-correlation analysis has been used in a wide range of studies as well as in fMRI data analysis [28]. Simultaneous linear coupling relationship between two time-series are measured by zero-order correlation. In the case of high positive correlation existence between time courses, emerges the inference that the two regions are simultaneously more or less active on average. As a result, when one region is more active than another this indicates that there is a high negative correlation between them. The usage of zero-order correlation measures inter-regional relationships in fMRI [72]. Inherently, a possible correlation of BOLD time courses implies that this part of the brain, involving these time courses, is functionally connected. For example, for the time course of a fMRI BOLD $F_x(k)$ and a seed $F_y(k)$, CCA evaluates the correlation at lag μ as:

$$Corr_{x,y} = \frac{cov_{x,y}(\mu)}{\sqrt{Var(x) \times Var(y)}}, \tag{4.16}$$

where Var(x) and Var(y) are the variances of $F_x(k)$ and $F_y(k)$, respectively and $cov_{x,y}(\mu)$ is the cross variance of $F_x(k)$ and $F_y(k)$ at lag μ:

$$cov_{x,y}(\mu) = E\{(F_x(k)-E(F_x)) \times (F_y(k)-E(F_y))\}, \quad (4.17)$$

and E means the expected value, and $E(F_x)$ and $E(F_y)$ are the expectation or the mean of $F_x(k)$ and $F_y(k)$, respectively. In the case of a higher value of $cov_{x,y}(\mu)$ than a certain threshold, it is assumed that the two BOLD time courses $F_x(k)$ and $F_y(k)$ are functionally connected.

The full-lag-space calculation of cross-correlation of the hemodynamic response of blood is not required and this is a good point because there is high computational cost for the full calculation of cross-correlation at all lags. The duration of HRF is restricted, individual subjects. It emerges that in a short time (few seconds) the HRF will return to the baseline and this requires the computation of correlation to be achieved in this time period which depends on the TR of fMRI scans. It is frequent that in many cross-correlation studies, only the correlation with zero lag is computed [28].

Coherence analysis

CCA is widely applied to many task-based or resting state fMRI studies. The use of correlation at zero lag as the connectivity measurement is debatable. The correlation presents sensitivity to the HRF shape which reveals differences across subjects or brain regions. In addition, it is possible that high correlation be noticed between regions with no blood flow fluctuations or because of distortions caused by noises such as cardiac activity or blood vessel activity.

In order to overcome the aforesaid misunderstandings, a proposed metric, the so-called coherence, is described below [28]. Coherence measures belong to the frequency domain in comparison with correlation measures which belong to the time domain. The first is responsible for time delays involving the effects of one region on another and it has great usage as statistic for the functional connectivity studies. In the case of similarity existing in time-series between two different regions which appeared with a time delay, the effect on zero-order correlation and coherence appear to be different. The first shows moderate or low values as compared with the coherence which appeared to have higher value in the bandwidth of the curve [72].

For the same time courses $F_x(k)$ and $F_y(k)$ defined in Eq. (1), the coherence is expressed as:

$$coh_{x,y}(\lambda)=\frac{|F_{x,y}(\lambda)|^2}{F_{x,y}(\lambda)F_{y,y}(\lambda)}, \tag{4.18}$$

where $F_{x,y}(\lambda)$ is the cross spectrum, defined by the Fourier transform of the cross covariance as follows:

$$F_{x,y}(\lambda)=\sum_u Cov_{x,y}(u) \times e^{-j\lambda u}, \tag{4.19}$$

and $F_{x,x}(\lambda)$ is the power spectrum, so is $F_{y,y}(\lambda)$.

They are defined as:

$$F_{x,x}(\lambda)=\sum_u Cov_{x,x}(u) \times e^{-j\lambda u}, \tag{4.20}$$

$$F_{y,y}(\lambda)=\sum_u Cov_{y,y}(u) \times e^{-j\lambda u}. \tag{4.21}$$

A more efficient approach to study time course relationships can be achieved with the expression of correlation in frequency domain. For example, at low frequency below 0.1 Hz the coherence can be related to functional connectivity, while at higher frequency values around 1.25 Hz the coherence may result from cardiac activity rather than functional connectivity [28].

Statistical parametric mapping

Statistical Parametric Mapping is the most commonly used method in order to feature functional anatomy, functionally specialized responses of the brain and define disease-related changes. From the perspective of functional integration, the relationship among activity changes in one region to another is investigated by multivariate approaches. SPM is a voxel-based approach which utilizes classical inference aiming to the annotation of particular regional responses related to experimental factors. Recently, statistical parametric maps (SPMs) are the means of analyzing and making classical inferences about spatially extended data in the combined use of general linear model (GLM) and Gaussian random field (GRF) theory. The parameters estimation which describes the spatially continuous data with great similarity to conventional analysis of discrete data is accomplished by GLM. On the other hand, GLF theory dealing with the resolution of the multiple comparison problem which generates from making inferences over a volume of the brain. GRF theory makes available a method in order to correct p values for the search volume of a SPM and its contribution is similar to

those on continuous data (images) as the Bonferonni correction for the number of discontinuous or discrete statistical tests [73].

Although SPM methodology is commonly referred as a method for task-based fMRI experiments, it can also be applied to resting-state fMRI investigations. The first processing step requires scaling and filtering across all brain voxels. The average of the voxels in certain seed is taken into account and assumed as a covariate of interest in the first-level SPM analysis. Subsequently, the contrast images that belong to this regressor are defined for each subject separately. Finally, these images are imported to a second-level random effect analysis, aiming to the determination of the brain areas which are significantly functionally connected across subjects [28].

Advantages-disadvantages of model-based methods

The prevailing point of SCA in comparison with others methods is the fact that it directly clarifies the network of the region that implies high level of functional connectivity with the seed voxel or ROI. Scientists find this straightforward interpretability of SCA interesting. According to a recent evaluation of SCA test-retest reliability, it has emerged that SCA is able to detect resting state networks (RSN) connectivity relationships with high reliability.

However, it should be taken into account that the nature of the univariate method to correlate time-series of single voxel with other voxels in a brain image, ignores the available information within the statistical relationships between multiple data points. The correlation and the evaluation of the activity of a prior selected time-series in a sub-region and the whole network places anatomical limitations on the measurement of network connectivity and as a result on interpretations of systems-level hypotheses. From the biological perspective, it is possible that the selection of the seed lead to connectivity results towards certain, smaller or overlapping sub-systems rather than larger, distinct networks [71].

4.2.3.2 Data-driven functional connectivity analysis

To eliminate the problems that emerge from model-based methods, that have direct dependency from prior knowledge or assumed model, alternative approaches for functional connectivity analysis, which are based on data, have been invented. There are two basic types included in these data-driven methods. The first refers to decomposition techniques such as principal component analysis (PCA), singular value decomposition (SVD) and independent component analysis (ICA) and the second

includes clustering analyses such as fuzzy clustering analysis (FCA) or hierarchical clustering analysis (HCA). The discrimination is achieved according to the way the data is analyzed. Decomposition techniques aim to express the dataset as a linear combination of basic vectors (PCA/SVD) or statistically independent components (ICA). In contrast, clustering techniques are addressed on fMRI dataset in clustering analysis methods. Both methods support the investigation of functional connectivity of human brain as a whole [28].

Decomposition-based methods

Principal component analysis (and singular value decomposition)

Two commonly used techniques for data analysis are the PCA and SVD. They are regarded as one type of analysis because of the fact that they have a close relationship. One of the most popular methods for matrix decomposition is PCA which is able to re-express the dataset in a set of uncorrelated or orthogonal to one other components [29]. Each contributor consists of a temporal pattern (a principal component) multiplied with a spatial pattern (an eigen map). Mathematically, the SVD of X (T time points × N voxels) is:

$$X = USV^T = \sum_{i=1}^{p} S_i U_i V_i^T, \tag{4.22}$$

where the S_i is the singular value of X, U_i is the j^{th} principal component, V_i is the corresponding eigen map and p is the number of chosen components. The brain regions connectivity is extracted by the produced eigen maps, where a high absolute value (either positive or negative) indicates a correlation [28].

As shown in Fig. 4.8, the PCA is able to find the orthogonal component of a set of data. The direction in which data present the highest amount of variable corresponds to the first principal component and the direction that presents the next greatest amount of variance corresponds to the second principal component which is not correlated with the first one, and so on.

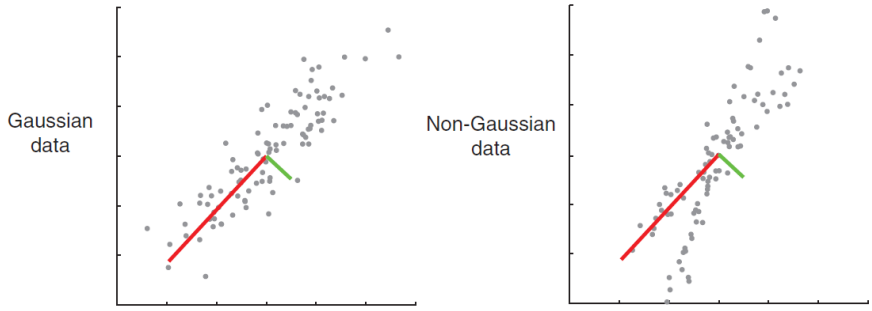

Figure 4.8: On Gaussian data, PCA finds the first component in the direction which carries the greatest variance and the second orthogonal component (left). On mixture data of two different signals, PCA is not able to find these non-orthogonal sources (right) [29].

The minimum of the number of dimensions or observations can produce the number of components. In the case of fMRI data, the number of dimensions (voxels) is different from the number of observations (timepoints or subjects). Another use of PCA is to reduce data. It is easier to analyze data from the first few principal components that represent the majority of the variance in the data, instead of analyzing the data from the huge number of all voxels. In order to implement PCA on fMRI data, it is necessary that data be expressed in a two-dimensional matrix, where the columns represent the voxels and rows the timepoints/subjects. PCA is able to find a set of components with a given value in each timepoint, reflecting the combination of voxels which represent the greatest variation. It is also feasible to estimate the level of contribution of the voxels in each component.

Due to the simple and easy implementation of PCA, it has been used in many studies as a method for functional connectivity analysis. However, its sensitivity only on Gaussian distributed data constitutes an important disadvantage. Several fMRI data follow Gaussian distribution, so PCA can be effectively performed, but in the case of non-Gaussian fMRI data, PCA can confuse the signal of interest. To overcome these undesirable effects, the ICA is a proposed method as it is more appropriate. Because of its effectiveness on fMRI data analysis, ICA has supplanted PCA on functional connectivity characterization [29].

Independent component analysis

A recent and widely used method for functional connectivity analysis with fMRI is Independent Component Analysis (ICA) which is well suited not only on task-based

fMRI experiments but also on resting-state fMRI investigations as it does not require any prior information about spatial of temporal patterns of source signals. For this reason, the use of ICA algorithm has been really attractive to scientists in order to find functional connectivity using resting-state fMRI [28].

Unlike general linear model (GLM) which sets as condition the parametrizing of the data by the user and PCA which takes into account the notion of uncorrelatedness and normality, ICA is based on the assumption of statistical independence [74, 75].

The fundamental purpose of ICA is the solution of the blind source separation problem. For this reason, a set of random variables (observations) is expressed as a linear combination of statistically maximally independent latent components variables (source signals) . Blind signal separation is an explorative technique which is used in the field of image and sound analysis. The definition blind was given due to the fact that the tools used in this technique try to detect mixed signals coming from unknown sources. For instance, in the cocktail party problem, signals from multiple sources with different relative amplitudes, are recorded by several microphones. ICA is based on the assumed statistical independence of the source signals and is a method used for blind signal separation. Because of the fact that signals are of various types on fMRI recordings, blind signal separation techniques are suitable to isolate and distinguish the source of these signals separately [76].

This ability of ICA to separate individual sources of different signals is presented in the following figure (Fig. 4.9).

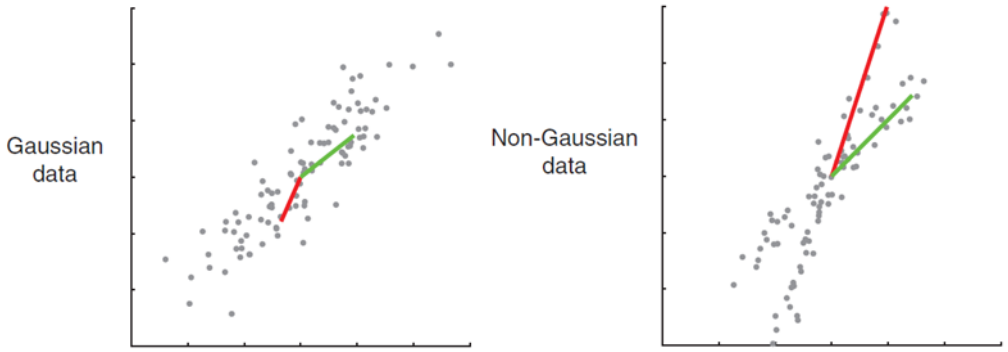

Figure 4.9: ICA can distinguish the two signals with accuracy in mixture (non-Gaussian) data (right panel), in comparison with its implementation on Gaussian data, which might fit to the noise since there is no signal after whitening [29].

For fMRI data X (T time points × N voxels), the ICA model can be expressed as:

$$X = AC = \sum_{i=1}^{N} A_i \, C_i, \tag{4.23}$$

where C_i is the j^{th} underlying signal source (IC component), A is the mixing matrix with a dimension of T×N. Different sources are independent from each other:

$$P(C_1, C_2, \dots, C_N) = \prod_{i=1}^{N} P(C_1). \tag{4.24}$$

Here, $P(C_1)$ is the probability of the i^{th} underlying signal source. Denoting W as the pseudo reverse of A (W also called unmixing matrix), we can obtain the independent components (ICs) simply by [28]:

$$C = WX. \tag{4.25}$$

The statistical information needed for ICA accomplishment is higher than second order, so one way that it be produced is by nonlinear functions or be fully estimated. Algorithms that use non-linear functions and are based on maximum likelihood estimation, maximization of information transfer, mutual information minimization, and maximization of non-Gaussianity can be used in order to produce higher-order statistics [74].

The most common algorithms that are used in order to solve ICA are Infomax and Fixed-Point. Both of them are based on minimization of mutual information of components C_i. Using adaptively minimization of the output entropy of neural network with as many outputs as the number of ICs to be estimated Infomax manages to accomplish this aim, while Fixed-Point is based on the notion of negentropy [28]. There are studies that reveal the conjoint efficiency and accuracy of the findings after implementing both algorithms. In addition, they carry their separate own advantages. Fixed-Point algorithm prevails over Infomax according to spatial and temporal accuracy in comparison with Infomax which is more powerful in global model estimation and the decrease of noise [76].

After performing ICA on a dataset, the original time sources are decomposed into independent components which are characterized by statistical independency and correspond to IC maps which include correlation measures. The connectivity maps with the corresponding underlying sources can be acquired after applying a threshold to IC maps [28].

During the performance of ICA, two different assumptions are possible to be made which lead to different findings. First, the reconstruction of the original 4D matrix into a 2D matrix is needed. Subsequently, the first assumption considers that the data

constitutes of T random variables (timepoints) each of which are measured in N voxels. From this perspective, T three-dimensional activation maps are generated. Hence, each 3D map is possible to be analyzed into an original N×T matrix. As a result, the mixing matrix A has T×T dimensions. In contrast, the second assumption includes the expression of the data as N random variables each of which are measured in T time points. Consequently, the output is N independent time-series the length of which is T. This leads to an original T×N matrix with X dimensions and a mixing matrix A with N×N dimensions.

The ICA can be distinguished in spatial ICA and temporal ICA depending on the way the data is decomposed. Spatial ICA based on the analysis of spatially independent components and spatially independent time course. In contrast, temporal ICA is referred to the data decomposition into temporarily independent components and temporarily independent time course.

Both methods are used in a variety of fMRI studies but the nature of the task determines the most suitable selection, as these methods have different results regarding the characteristics of the underlying signals that are to be assessed. Temporal ICA is the proposed method in the case that the underlying signals are spatially but not temporarily correlated. In contrast, when signals are temporarily but not spatially correlated, spatial ICA suits effectively on data [28].

The use of ICA algorithms in fMRI studies bas been to a large extent. However, there are some obstacles that should be taken into consideration. For example, a pitfall could be the violation of the assumption of spatially or temporarily independence of the components (signal sources) which might lead to the inefficiency of ICA. Also, a discussion might arise about the appropriate way of independent components selection as well as about thresholding the IC map in order to derive all the important information concerning functional connectivity. For example, in the case that the number of the signal of sources is bigger than the number of ICs, there is great dependency on the number of ICs. According to the second questioning, thresholding directly IC maps it has been confirmed that it is a difficult task. Practically, it is usual to transform an independent map with non-Gaussian distribution into a z-map with a Gaussian distribution, but it carries a dilemma, the overestimation of the false positive rate (FPR), although in many cases it could be disregarded, as it does not cause severe problems. Finally, ICA is a non-free generative model, that can express in detail the fMRI dataset

through source signals and the mixing matrix A. Hence, this does not allow the evaluation of the statistical significance of the source within the framework of null-hypothesis. The recently developed model, the so-called probabilistic ICA comes to overcome this problem. According to probabilistic ICA, a set of q (q<p) statistically independent non-Gaussian sources (spatial maps) produce the observed p dimensional time-series through a linear and instantaneous 'mixing' procedure violated by additive Gaussian noise η(t):

$$X_i = AS_i + \mu + \eta_i, \tag{4.26}$$

where X_i is the p-dimensional column vector of individual measurements at voxel location I, A is mixing matrix, S_i refers to the q-dimensional column vector of non-Gaussian source signals contained in the data, μ is constant part and η_i is the Gaussian noise $\eta_i \sim N(0, \sigma^2\Sigma_i)$ [28, 77].

In the perspective of making inferences about a group of subjects, in comparison with univariate methods, ICA is not able to naturally generalize to a method suitable to achieve this. For instance, in the case of applying GLM on a set of data, the specification of regressors of interest is determined by the investigator. This is why inferences about group data arise naturally as all subjects in the group use common regressors. On the other hand, during ICA implementation, different subjects in the group have different time courses, so they will be classified in a different way, a fact that does not clarify directly the way of making inferences about group data by the use of ICA.

However, there are some ICA multi-subject analysis approaches that have been recommended. These approaches are classified into five categories, combining single subject ICA, group ICA with temporal concatenation or spatial concatenation, pre-averaging and tensor ICA. Their discrimination is based on the way the data has been grouped before the analysis, what kinds of output are available and the way of the statistical inference process [74].

Several approaches, which are included in the first category, first perform single-subject ICA and afterwards use approaches such as self-organized clustering or spatial correlation of the components in order to combine the output into a group post hoc. This bears the benefit that it recognizes unique spatial and temporal features, in comparison with the fact that because of the nuisance of the data, the components are not certainly mixture similarly for each subject. The other four approaches include the

ICA computation on the whole group dataset. The advantage that has arisen after examining the temporal and spatial concatenation is the single performance of ICA, which afterwards is able to be separated into subject-specific parts, therefore it is simple to compare subject differences within a component. Temporal concatenation approach provides unique time courses for individual subjects but supposes common aggregate spatial maps. In contrast, spatial concatenation approach provides unique spatial maps but supposes common time-series. Despite their differences in data organization, it has been proven that temporal concatenation suits better on fMRI data due to the fact that ICA time courses are greater regarding temporal variations in comparison with the variation in the spatial maps at conventional field strengths of 3T and below [78].

Averaging the data before ICA is assumed as a less computationally demanding approach but allows possessing a common time course and a common spatial map. In order to evaluate group-specific temporal responses and common spatial maps in an extended group, the tensor model is suggested to be used. Last, the so-called as multidimensional or multi-way or N-way decompositions which represent the tensor decomposition approaches, have recently been considered with great interest. However, their effectiveness on group and multi-group fMRI data, has not yet been clarified. A representative approach uses three-dimensional tensor in order to assess a single spatial, temporal and subject-specific process for each component to recognize the multidimensional structure of the data in the estimation stage. This approach might have no reliable results without additional preprocessing, in the case of the existence of different time courses between subjects. This occurs in a resting state MRI study where it is clear that there is no synchronization of time courses between subjects, in comparison with task-based fMRI experiment which involves similar timing between subjects [78].

Clustering Analysis

The estimation of activity patterns in fMRI studies can be achieved by the commonly used clustering analysis methods. Fuzzy clustering analysis, vector quantization, self-organizing maps, and neural gas network are notions that are included in these methods. Implementing clustering analysis on fMRI data aims to classify the data into different clusters based on the intensity proximity of the time course. When time courses have high adjacency are assumed as one cluster. It is worth noting that clustering analysis which is based on intensity proximity provides low sufficiency regarding the detection

of functional connectivity. This is why the contribution of clustering analysis methods in fMRI studies relies on the similarity between time courses as the distance measurement, instead of the characterization of the distance by intensity proximity [28].

Fuzzy clustering analysis

Fuzzy clustering analysis (FCA) is an exploratory and paradigm independent method with high implementation on fMRI data analysis in order to estimate functional connectivity signals. Because of the fMRI data nature which includes a great amount of data as well as a wide range of noises, it is necessary that FCA undergo some restrictions on some fMRI applications. The typical FCA method based on the evaluation of the similarity between two single voxels using Euclidean distance or Pearson correlation coefficient, which are attractive for their sensitivity, simplicity and simple interpretation. Nevertheless, these univariate distance similarity measures carry several disadvantages. Specifically, the computational time of these fMRI data analysis is huge with many repetitions because of the slow speed of convergence. It is not possible that univariate based measures accomplish steady iterative state quickly. Furthermore, spatial random noise which is included in fMRI data should not be ignored. The high susceptibility of univariate analysis methods on noise could lead to blurred and obscure connectivity maps, even if smoothing decreases an amount of spatial noise.

In order to estimate efficiently the similarity between two sets of variables with the same number of sample observations, a multivariate statistic, the RV coefficient has been suggested [79].

A different way of hard clustering is proposed with the use of FCA. Its aim is to detect a division of a dataset X of n time courses that are assumed as points in t-dimensional space. They are to be given to one of the c cluster centers (representative time courses) which are assigned by a matrix V (c, t). The c-partition of X is determined by the matrix U (c, n) and the u_{ik} are the membership values of k-th voxel to i-th centroid.

$$0 \leq u_{ik} \leq 1 \,, \forall\, i, k \,, \tag{4.27}$$

$$0 < \sum_{k=1}^{n} u_{ik} \leq n \,, \forall\, i \,, \tag{4.28}$$

$$\sum_{i=1}^{c} u_{ik} = 1 \,, \forall\, k. \tag{4.29}$$

An increased developed version of fuzzy C means algorithm defines the matrices U and V and minimizes the functional J_m:

$$J_m(X, U, V) = \sum_{i=1}^{c} \sum_{k=1}^{n} u_{ik}^{m} d^2(x_k; v_i), \tag{4.30}$$

where d (x_k; v_i) is the distance between the k-th datum and the i-th centroid. The hyperbolic correlation coefficient (HCC) measure is related to single-voxel metric measure which is a contrast to the RV distance measure. It is expressed by a function of the correlation coefficient ρ_{ik} between each data vector x_k and the prototype v_i:

$$d(x_k;\ v_i) = (1 - \rho_{ik})/(1 + \rho_{ik}). \tag{4.31}$$

A two-stage iteration gives the solution of minimizing J_m:

$$v_{il} = \frac{\sum_{k=1}^{n} u_{ik}^{m} x_{kl}}{\sum_{k=1}^{n} u_{ik}^{m}}, \tag{4.32}$$

$$u_{ik} = \frac{1}{\sum_{j=1}^{c} \left(\frac{d(x_k; v_i)}{d(x_k; v_i)} \right)^{\frac{2}{m}-1}}. \tag{4.33}$$

Where v_{il} is the element of matrix V and m (m>1) is a parameter aiming to control the fuzziness of the clusters. When the algorithm fulfills the predetermined requirements, the iterations pause.

In order to examine the functional connectivity intensity between each location in the brain in a particular centroid, the search cube should be centered in a specific voxel. The centroid search cube is centered on the center of the cluster and datum search cube on the center of the voxel which is going to be classified. The multiple nearby voxels of the cube have their own shape and size and the next step is to move the datum search cube across all voxels on the whole brain. The multivariate similarity between the time courses of the voxels indicating the centroid search cube and the time courses of the voxels indicating the datum search cube are estimated at each location. By selecting the search cube of different sizes and shapes, the connectivity patterns mapping of different spatial scales can be obtained [79].

The multivariate statistics of RV coefficient estimates the similarity between two sets of time courses. The RV coefficient is expressed as follows:

$$RV(X, Y) = \frac{tr(XX^tYY^t)}{tr(XX^tXX^t)^{\frac{1}{2}} \times tr(YY^tYY^t)^{\frac{1}{2}}}, \tag{4.34}$$

where X and Y are n×p and n×q matrices from two data sets which include p and q numerical variables on the same sample of n time points, X_t is the transpose of matrix

X and tr (·) is the trace operator of square matrix. In the case of X dataset consisting of voxels classified into the datum search cube centered by x_k and Y dataset consisting of voxels classified into the centroid search cube by v_i, the distance can be expressed by:

$$d(x_k; v_i) = D(X, Y) = \sqrt{2(1 - RV(X, Y))}. \quad (4.35)$$

The RV coefficient value varies between 0 and 1. The value of 0 corresponds to two independent sets, a fact that reveals absence of correlation or similarity between datasets. The value 1 of RV coefficient indicates that the eigen components of dataset X can be extracted from Y across a homothetic transformation that presents a rotation matrix H and a scaling factor c such that cXH=Y. The RV calculation demands the centering of X and Y into columns [79].

Hierarchical clustering analysis

The hierarchical clustering analysis assumes each voxel as one cluster during the beginning and units the close clusters according to specific distance measurement, in opposition to FCA which demands an empirical selection of a number of initial clusters. This notion of closeness can be estimated through methods which separate single-linkage from complete-linkage and average-linkage clustering [28].

The newly developed single-linkage HCA algorithm measures the distance using the combination of correlation analysis and frequency decomposition. The decomposition of Pearson's correlation coefficient $CC_{x,y}$ between two time courses $F_x(k)$ and $F_y(k)$ is described as:

$$CC_{x,y} = \frac{N\sum_f Re(\omega_f)Re(\varphi_f)+Im(\omega_f)Im(\varphi_f)}{S} = \sum_f \frac{N(Re(\omega_f)Re(\varphi_f)+Im(\omega_f)Im(\varphi_f))}{S} = \sum_f CC_f(x, y). \quad (4.36)$$

Where ω_f and φ_f are complex frequency component of $F_x(k)$ and $F_y(k)$ respectively and Re (*) and Im (*) represent the real and imaginary component of signal*. S is described as:

$$S = \sqrt{\sum_{k=1}^{N-1} {F_x}^2(k) \sum_{k=0}^{N-1} {F_y}^2(k)}. \quad (4.37)$$

The distance D (x, y) between $F_x(k)$ and $F_y(k)$ is defined as:

$$D(x, y) = 1 - \sum_{f=0}^{0.1Hz} CC_f(x, y). \quad (4.38)$$

In summary, a low-pass filter to Pearson's correlation coefficient is implemented by this distance and then a reverse increase function is stored in order to map the output into distance. The information that demonstrates synchrony in cerebral blood flow and oxygenation between different brain regions is extracted from the correlation coefficient by the previous filtering process.

According to the experiments including simulated or human brain data, it has been proven that structured contaminations such as respiratory or cardiac noises can be effectively removed. Because of the high computational cost of HCA, when implemented on the whole brain, the enhancement of these methods is demanded [28].

Because of the poor scaling, high complexity and sensitivity to outliers, hierarchical clustering analysis does not have the ability to be applied with fluency as other methods do in resting-state fMRI analysis. But, what should not be ignored is the fact that this approach is fully deterministic and is able to express data as stratum through a hierarchical structure, not to re-mention its high computational cost [80].

Comparison between Model-based and data-driven analysis methods

The selection of model-based or data-driven methods for functional connectivity analysis has been a long-term debatable topic. Despite the attempt of researchers to suggest the most appropriate method, there is no evidence to prove the supremacy of one of them. One method does not reject the other as their selection depends on the nature of study. For example, when prior experience and knowledge already exists and methods may produce the same findings, disregarding them is not wise. Additionally, the use of ICA instead of CCA in studies that aim to find extensive regions of correlated voxels appear to be more efficient [28].

The following figure (Fig. 4.10) illustrates a schematic representation of functional connectivity analysis methods.

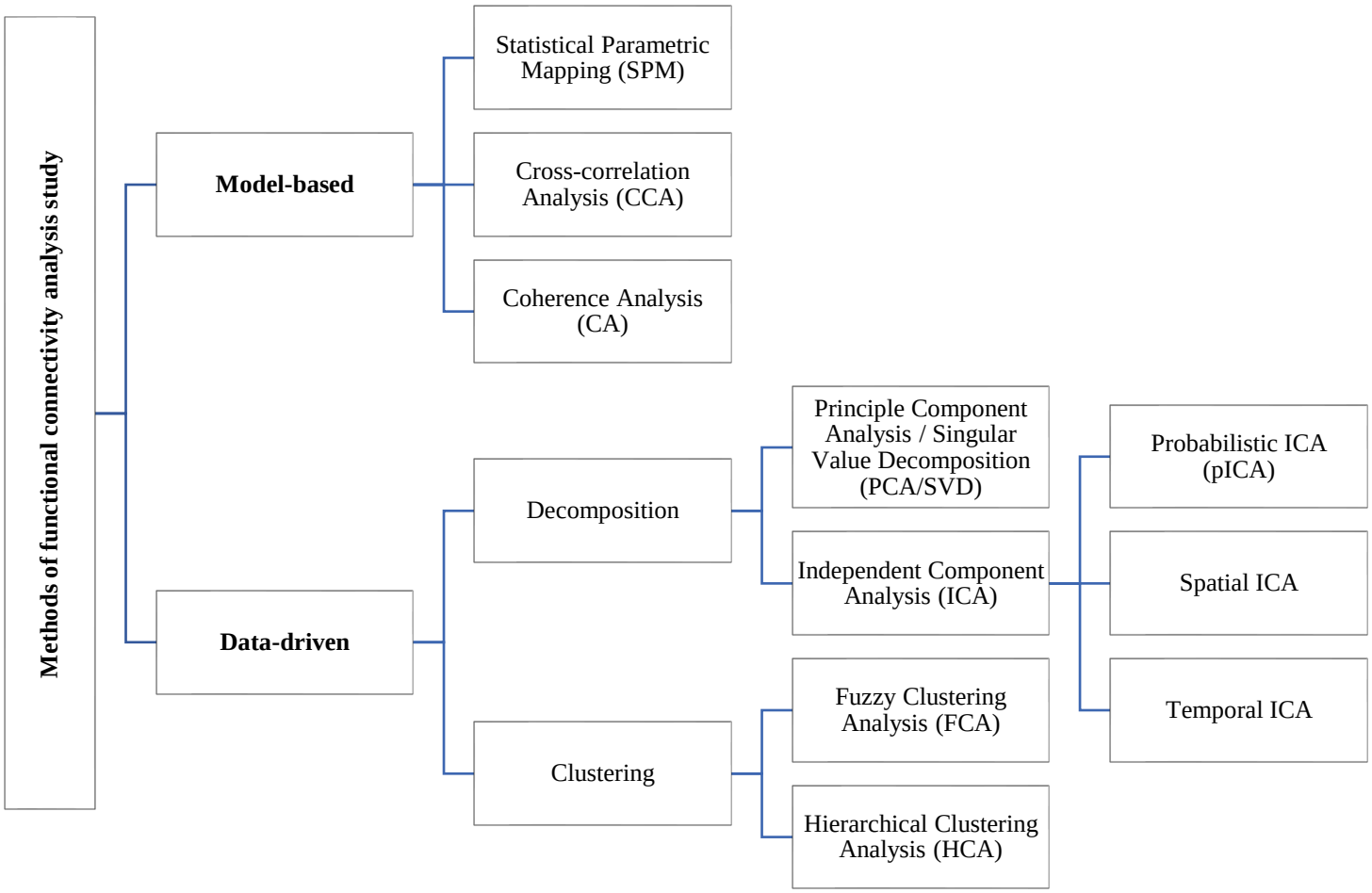

Figure 4.10: Schematic representation of functional connectivity analysis methods [28].

4.2.4 Effective connectivity

Effective connectivity describes the influence that one neural system exerts over another at a synaptic or cortical level, denoting causal interactions between activated brain areas [59, 81]. This definition refers to a more mechanistic way through which observed responses are explained and it might be interpreted as the experiment- and time-dependent, the simplest feasible circuit diagram which accurately represents the observed relationships of time between recorded neurons. As a result, effective connectivity tends to be dynamic (activity-dependent) and has great dependency on a model of directed interactions or coupling [82].

Based on the aforementioned case, temporal dynamics (dynamic functional connectivity) could be considered as an attractive assumption on the functional connectivity development, but it is limited regarding the causal explanation extraction which is achieved by effective connectivity methods. This is due to the fact that functional connectivity deals with the definition of second order data characteristics, preventing the interpretation of neurophysiological time-series under a mechanistic perspective [82]. Obviously, functional and effective connectivity show appreciable differences in practice, despite their common use in the fields of neuroimaging and electrophysiology. For example, the neurophysiological measurements do not have similarities according to the time-scale and their nature (seconds *vs.* milliseconds and hemodynamic *vs.* spike trains) in comparison with electrophysiological measurements. Furthermore, in order to detect the underlying connectivity in electrophysiology, the confounding effects of stimulus-locked transients, which present correlations by neural interactions (not causally mediated), should be discarded. In contrast, from the neuroimaging perspective, the previous problem is less important, as the promulgation of dynamics from primary sensory areas onwards is mediated by neuronal connections (usually reciprocal and interconnecting) [81]. Consequently, it is crucial to distinguish operationally the notions of functional and effective connectivity as it shapes the character of the inferences coming from functional integration and answers the questions that arise from intricate interrelationship between effective and functional connectivity [82].

The inference of causal relations is quite demanding due to the special features of fMRI data. First of all, the issue that requires attention concerns the size of the model space. Testing all possible graphs in order to find the most suitable for the data, could be a straightforward method to clarify how brain regions influence one another (which is the objective of effective connectivity). When the number of regions in the graph becomes bigger, the directed graphs that possibly exist, are also increased at super-exponential degree as a function of the number of the regions, a fact that cannot be controlled even with fast computers. Specification of a small set of models based on prior knowledge could be a solution to the problem, but the validity of the results can only be established by focusing on the tested models. However, this seems to be impossible. This is why the most suitable model fitting is rendered to be an important issue [29].

It is worth noting that the underlying neuronal signals refer to the causal interactions that are under investigation, despite the fact that effective connectivity analyses are implemented to fMRI data. So, it is necessary to evaluate the causal relations of variables from observed signals which also contain noise and systematic distortion of the signal (such as hemodynamic delays). A problem that might arise concerning the estimation of underlying causal interactions is that the recorded noise leads to the identification of fake causal relations which has not actual existence. Additionally, in the case of being based on temporal information to extract causal relations, the hemodynamic response differences across regions are also the reason for fake causal association.

Except for the information that effective connectivity analysis carries regarding the relations between activation across regions, it is noteworthy that the interest is turned towards the inferences concerning connectivity patterns that appear in larger groups of subjects instead of taking into consideration a certain set of sampled individuals. Furthermore, it is possible that characteristics like age, experience, genetics or other factors affect the true pattern of connectivity varying the connectivity parameters across subjects, even in the case of their sharing common causal structure. This emphasizes the need for the existence of appropriate methods for effective connectivity evaluation at population level. The straightforward approach that includes the combination of the data across subjects and the estimation of the model in the complex dataset is not suggested, as it could lead to an observed pattern of independence and conditional independence interactions that do not represent any subject in the group. As a result, random effect analysis is required to achieve accurate and effective evaluation of connectivity across subjects [29].

Because of the diverse nature of causal influences of effective connectivity and its various interpretations, which is differentiated from the notion of synchronization in functional connectivity analysis, it is necessary that different methods of effective connectivity analysis be applied [83].

Effective connectivity is described by two models (linear and non-linear) which explain the way brain areas are connected from the aspect of mathematics and which areas are connected from the aspect of neuroanatomy. According to experience, linear model can provide quite adequate results but attention should be paid to non-linear models for effective connectivity analysis. The base of this reasoning is that brain reacts at simple and well-organized experiments in a straightforward process, in

comparison with neurophysiological interactions that appear to be non-linear and put the efficiency of linear models in dispute [23].

A set of assumptions about the inherent data structure (time-series, correlation matrix or higher-order statistics) or underlying biophysics that are going to be modeled are employed at the beginning of approaches utilized in effective connectivity evaluation. Subsequently, maximum likelihoods or Bayesian inferences are some of the criteria that are taken into consideration in order to search the optimum models and lastly the conclusions of the causality or conditional dependences are emerged from the learned model parameters.

For a fMRI study, effective connectivity can be commonly applied using approaches such as dynamic causal modeling (DCM), Granger causality analysis, structural equation modeling (SEM), psychophysiological interactions (PPI), graphical causal modeling, dynamic Bayesian networks and switching linear dynamic system and have been widely used in clinical studies [35].

Structural Equation Modeling (SEM)

In the field of statistics, SEM describes a set of equations with *supporting* assumptions of the analyzed system, in which parameters are based on statistical observations. So, structural equations are described as equations utilizing parameters in the analysis of the observable or latent variables [84].

SEM is a suggested method for effective connectivity estimation on fMRI data. This is a multivariate linear statistical technique, that describes steady-state coupling between brain regions with the use of the covariance structure of the data, ignoring the temporal dynamics of the fMRI time-series [85, 86].

SEM, as a method testing hypotheses about causal inferences between variables, including regions and the directed connections between them [29, 57]. The path coefficients for each link are estimated reflecting the altered activity of a region having been influenced by a given unit change. They also denote the average influence across the time interval measured. A SEM model can be expressed in algebraic form as:

$$Y = MY + \varepsilon. \tag{4.39}$$

Where Y is the data matrix, M is a path coefficients matrix and ε is independent and identically distributed Gaussian noise.

Another representation of the previous form could be:

$$Y = (I - M)^{-1}\varepsilon, \quad (4.40)$$

where I is the identity matrix. The empirical covariance matrix of Y is utilized in order to acquire the solution of the unknown coefficients which are included in M [57]. SEM has the characteristic to minimize the difference between the observed or measured covariance matrix as well as in the structure of the model. The free parameters (path coefficient or connections strengths) are modified in order to minimize the difference between the measured and modeled covariance matrix [23]. Nested models and likelihood ratio test (LRT) are the basis of all inferences according to the assumption whether a path coefficient is reliably different from zero [57].

This technique is highly popular concerning the effective connectivity evaluation on neurocognitive systems, primary dealing with PET and fMRI data and then also on EEG data [87, 88]. This fact renders it a suitable model for diverse cognitive networks, including those mediating visual perception, motor control, language function, associative learning and pain processing [87].

The positive aspects of SEM include fast and robust computations as well as its implementation on large-scale simulations using neuroimaging data. SEM is not a recently developed method so there are many software packages and algorithmic variations accessible [88].

In contrast, there are some model assumptions that arise during SEM performance that should be taken into consideration. The assumption of normally distributed and independent from sample to sample data leads to SEM providing reduced temporal information. As a result, a weakness which emerges is the production of the same path coefficient as the original data on permuted data, because the assumed independence is disrupted in the analysis of a single subject [57]. The disadvantages also include the high dependency of the sample size on the absolute evaluation of the model, the primary estimation of the connection directions and the incapability of utilizing fully reciprocal models [88].

Granger causality modeling

Granger causality is a general methodological approach developed for the analysis of economic data, which studies the relation in time between variables in order to model causality. It is based on the concept of temporal precedence information [29]. It is one more method which examines effective connectivity analyzing dependencies in fMRI time-series. Granger causality is often framed in terms of a multivariate autoregressive

(MAR) model in order to capture interactions among brain regions, describing a causal and dynamic system of linear interactions, driven by stochastic innovations [88, 89]. In this method, priori specification of a structural model is not required, as past values of one brain region are taken into account so that current values of another can be predicted [57].

According to theory, a vector autoregressive (VAR) process of order p can be used in order to model the discrete zero-mean vector time-series $x[n] = (x_1[n], \dots, x_M[n])^T$ as follows:

$$x[n] = -\sum_{i=1}^{p} A[i]x[n-i] + u[n], \tag{4.41}$$

where u[n] is the (multivariate) white noise. Because of the fact that the matrices A[i] regress x[n] onto its own past, they are known as autoregression coefficients. As it has already been said, VAR model could be assumed as linear prediction model that tries to predict the present value of x[n] based on a linear combination of the most recent past p values. As a result, the current value of a component $x_i[n]$ is predicted based on a linear combination of its own past values and the past values of the other components. Thus, the importance of VAR concerning Granger causality evaluation across groups is verified. The direction of causality from information in the data is achieved by temporal precedence. If two time-series x[n] and y[n] are given, the influence from x to y and the influence in the reverse direction can be independently determined by suitable models. A measure of linear dependence $F_{x,y}$, between x[n] and y[n] can be described as a sum of three components:

$$F_{x,y} = F_{x\to y} + F_{y\to x} + F_{x\cdot y}\ . \tag{4.42}$$

$F_{x,y}$ will evaluate to zero, if no value at a given instant of one can be described by a linear model containing all the values (past, present and future) of the other. $F_{x\to y}$ is a measure of linear directed influence from x to y and $F_{y\to x}$ from y to x, respectively. The two directed components use the arrow of time to define the direction of influence. Nevertheless, it is not certain that these directed components will fully provide a total linear dependence between x and y. A great amount of the total linear dependence can be interpreted by the instantaneous influence $F_{x\cdot y}$ between them. $F_{x\cdot y}$ is a measure to quantify the progress of the prediction of the current value of x (or y) assuming the current value of y (or x) as a linear model already including the past values of x and y. Conclusively, it is obvious that there is no directional information included in $F_{x\cdot y}$ as it

represents residual correlations in the data. Practically, the directed influence between x and y can result from the nonzero values of $F_{x \cdot y}$. These useful and accurate characteristics of these measures support investigation adapted to evaluate effective connectivity in fMRI data [90].

Unlike SEM and DCM (dynamic causal modeling which is described in detail below), Granger causality has the benefit of utilizing time-series directly in order to study whole-brain effective connectivity avoiding the determination of an anatomical network. On the other hand, there are some drawbacks concerning Granger causality modeling which emerge due to the temporal features of the fMRI data. First, the impact of slice-timing is of primary importance, as Granger causality is based on the relative activity of region in time. It is possible that the differences in relative timing of acquisition across slices have a greater value than the relative timing effects due to neural processing. Second, Granger causality considers that hemodynamic response has the same time characteristics across the brain, a fact that will generate spurious causes in Granger causality analysis performing. Actually, there are many studies which give evidence that Granger causality on fMRI time-series does not generate accurate causal influences, compared with the simultaneous use of electrophysiological and fMRI recordings. Accurate extracts can be accomplished only if time-series are deconvolved (with the use of the hemodynamic model taken from DCM in combination with electrophysiological recordings). Third, a solution to the problem that arises when data are sampled at a rate slower than the causal process (considerable short TR is suggested to acquire robust time-series), could be the obtainment of residuals from a time-series analysis (e.g. Granger causality analysis) and then applying the graphical causal model search procedures (which are described below). Finally, if multivariate extension is needed, it should be done with great care, as when many regions are involved, the results denote instability [29, 88].

Dynamic causal modeling (DCM)

The development of effective connectivity investigations renders the dynamic causal modeling (DCM) a powerful tool in order to evaluate causal architecture of coupled or distributed systems [91]. Generally, the concept of DCM is to define the parameters of a logically realistic neuronal system model in order to achieve an as much as possible fitting of the predicted BOLD signal (that arises from the converting of the modeled neural dynamics into hemodynamic responses) and the observed BOLD time-series.

Because of the state-space nature of DCM, the clarification of its levels is needed. A simple model of neural dynamics in a system of k coupled brain areas, corresponding to the hidden level of DCM, which is not possible to be observed directly by using fMRI. A single state variable z_i is used for each system element i representation and the neural state vector over time is used for the dynamics system description. According to the neural state variables, it is important to clarify that they are not equivalent to common neurophysiological measurement (as spiking rates or local field potentials do) but correspond with a summary of indicators of neural population dynamics in the respective regions. Essentially, the DCM describes the way the neural dynamics react to external disturbances that come from experimentally controlled operations. These disturbances are explained through means of external inputs u that can enter the model either evoking responses through direct influences on specific regions or changing the strength of coupling regions.

The temporal evolution of the neural state vector is modeled by DCM as a function of the current state, the inputs u and some parameters that explain the functional architecture and relations among brain regions at a neuronal level:

$$\begin{pmatrix} \dot{z_1} \\ \dot{z_2} \\ \dots \\ \dot{z_k} \end{pmatrix} = \dot{z} = \frac{dz}{dt} = F(z, u, \theta^n). \tag{4.43}$$

The state z and the inputs u, in the previous neural state equation, are time-dependent while the parameters are time-invariant.

F has the bilinear form in DCM:

$$\dot{z} = Az + \sum_{j=1}^{m} u_j B_j z + Cu\ . \tag{4.44}$$

The parameters of this equation $\theta^n = \{A, B_1, \dots, B_m, C\}$, can be described as partial derivatives of F:

$$A = \frac{\partial F}{\partial z} = \frac{\partial \dot{z}}{\partial z}, \tag{4.45}$$

$$B_j = \frac{\partial^2 F}{\partial z \partial u_j} = \frac{\partial}{\partial u_j}\frac{\partial \dot{z}}{\partial z}, \tag{4.46}$$

$$C = \frac{\partial F}{\partial u}. \tag{4.47}$$

The modeled neural dynamics include three causal components, the nature of which is defined by the previous parameter matrices. These components are the context-independent effective connectivity among brain regions indicating anatomical connections (k×k matrix A), context-dependent changes in effective connectivity

included by the j^{th} input u_j (k×k matrices $B_1, \ldots, B_m$) and direct input into the system that drive regional activity (k×m matrix C). The effect that different mechanisms have on determining the dynamics of the model is related to the posterior distributions of the aforementioned parameters. It is very important to discriminate the relative notions of 'driving' and 'modulatory' from the neurobiological perspective, because they present an analogy of large neural population studies.

This model of neural dynamics is combined by DCM with a hemodynamic model, which is featured by biophysically plausibility and experimental validity, and can express the transformation of neuronal activity into a BOLD response. This commonly known as "Balloon model" is composed by equations that delineate the association between four hemodynamic state variables using five parameters (θ^h).

The full forward model arises from the combination of neural and hemodynamic states into a joint state vector x and the neural and hemodynamic parameters into a joint parameter vector $\theta = [\theta^n, \theta^h]^T$ and is described below:

$$\dot{x} = F(x, u, \theta), \tag{4.48}$$

$$y = \lambda(x). \tag{4.49}$$

Assuming a set of given parameters θ and inputs u, the predicted BOLD response h (u, θ) results from the integration of the joint state equation and its pass through the output nonlinearity λ. The observation model that contains observation error e and confounding effects X can be expressed as:

$$y = h(u, \theta) + X\beta + e. \tag{4.50}$$

A fully Bayesian approach with empirical priors for the hemodynamic parameters and conservative shrinkage priors for the neural coupling parameters are used from this equation in order to evaluate the neural and hemodynamic parameters from the measured BOLD data [92].

Spectral dynamic causal modeling

Studying connectivity of resting-state brain intrinsic networks has recently become a very popular technique [93]. An extension to the DCM (spectral DCM) intends to model intrinsic dynamics on resting-state fMRI data defining the effective connectivity among coupled populations of neurons, which enclose the observed functional connectivity in the frequency domain [92]. Spectral DCM shows differences from stochastic DCM, as it utilizes scale-free methods to parametrize the neural fluctuations

and as a result, the stochastic model of neural activity changes its nature and becomes deterministic [93].

The general concept of spectral DCM is the adding of a stochastic term to model endogenous neuronal fluctuations in the ordinary differential equations used in the standard DCM. Thus, the motion equations become stochastic and the stochastic model for the resting-state fMRI time-series consists of the Langevin form of evolution equation ($\dot{z}$) and the observation equation (y). The observation equation is a static non-linear mapping from the hidden physiological states to the observed BOLD activity. These two forms are expressed respectively below:

$$\dot{z} = f(z, u, \theta) + u, \tag{4.51}$$

$$y = h(z, u, \varphi) + e, \tag{4.52}$$

where $\dot{z}$ is the rate in change of the neural states z, θ are unknown parameters (e.g. effective connectivity) and v is the stochastic process (state noise) modeling the random neuronal fluctuations that concern resting state activity. The unknown parameters of the observation function are denoted by φ and u relates to any exogenous inputs (that are often absent in resting-state situation). The form of Langevin equation for resting state activity has the form:

$$\dot{z} = Az + Cu + u, \tag{4.53}$$

where A is the Jacobian describing effective connectivity of the system near its stationary point in the absence of the fluctuations v.

Spectral DCM evaluates the time-invariant parameters of their cross-spectra. Obviously, the observed BOLD time-series of each node which were modeled in the stochastic DCM are the observed functional connectivity between nodes which are modeled in spectral DCM. Practically, it can be accomplished if the original time-series are replaced by their second-order statistics (cross spectra) directed by stationary assumptions. This leads to covariance estimation of hidden states, instead of estimating their time varying, as they present no alternation over time. Consequently, it is necessary to define the covariance of the random fluctuations. A power law form for the observation noise can be expressed as:

$$g_v(\omega, \theta) = \alpha_v \omega^{-\beta_v}, \tag{4.54}$$

$$g_e(\omega, \theta) = \alpha_e \omega^{-\beta e}, \tag{4.55}$$

where $\{\alpha, \beta\} \subset \theta$ are the parameters, which control the amplitudes and exponents of the spectral density of the neural fluctuations. A generic $1/f^{\gamma}$, which features the

fluctuations in systems that are at nonequilibrium steady-state, is used to model neuronal noise. The expected cross-spectra are given with the use of parameters $\theta \supseteq \{A, C, \alpha, \beta\}$ as:

$$y = \kappa * v + e, \tag{4.56}$$

$$\kappa = \partial_z hexp(t\partial_z f), \tag{4.57}$$

$$g_y(\omega, \theta) = |K(\omega)|^2 g_v(\omega, \theta) + g_e(\omega, \theta), \tag{4.58}$$

where the Fourier transform of the system's Volterra kernels κ, which are the function of the Jacobian or effective connectivity, are denoted by K(ω). Standard Variational Laplace procedures are used to determine the unknown quantities $\psi = \{\varphi, \theta, \sigma\}$of this deterministic model. The predicted cross spectra are described by $g_y(\omega, \theta)$ and their estimation can be possibly achieved with the use of autoregressive model (AR) [92].

Despite the fact that DCM makes available the tight coupling to biophysical models giving the ability to explain the effective connectivity in the field of neurophysiology, it has on the other hand some limitations such as the high computational cost and the weakness to estimate effective connectivity in more than six regions. Furthermore, researchers dispute the accuracy and reliability of the parameter estimation because of the restrictions of the generative model [88].

The three aforementioned methods (SEM, Granger causality and DCM) are proposed as the most appropriate methods for effective connectivity estimation of fMRI data [57, 61, 86, 88, 89, 94, 95]. Briefly, SEM analyzes steady-state brain connectivity patterns, ignoring temporal dynamics of time-series, Granger causality infers causal interactions with the use of vector autoregressive model and DCM models the dynamic effective relationship dealing with fMRI time-series [86, 94]. However, as we have primarily mentioned, there are also some other approaches that have been used for effective connectivity analysis although they are not that common. Their brief description is presented below.

Graphical causal models

This modeling type includes the graphical causal models, the alternatively so-called 'causal Bayes nets', which describes the combination of directed graph with a joint probability distribution on the graph nodes that depict random variables. The graphical structure aims to express the compositional structure of the causal relations and the features of all probability distributions that factor according to that structure. In the case of absent cycles into graphs (DAGs), the Causal Markov Property characterizes

the property of a graphical causal model in a set of variables as described below. According to the Causal Markov Condition that assumes G as the causal graph with vertex set V and P the probability distribution over the vertices in V generated by the causal structure represented by G, the Condition is satisfied by G and P if and only for each W in V, W is independent of V\Descendants(W)∪Parents(W) given Parents(W). The factorization of the distribution is related to the Markov property that indicates the equation between joint distribution of the variables for any value assignment and the product over all variables of the probability of the values of each variable conditional on the values of its parent variables. A graphical causal model may be characterized by linearity or non-linearity, may organize time-series or present feedback relations. The graph features a non-parametric simultaneous representation of restricted conditional independence and qualitative effective connectivity relations. Directed graphs with cycles or time-series with acyclic graphs can illustrate the feedback relations. Markov condition is not satisfied by cyclic graphs for linear simultaneous equations with independent disturbances, but a Markov condition generalization is suggested to be performed in order to express linear systems allowing a factorization and computation of the vanishing partial correlations that are satisfied by all linear parameterizations of the graphs [96].

The first problem this method carries has statistical nature and concerns the search over a space of alternative models and is generated by the enormous size of the possible space of alternative causal models. The second one is related to the statistical consequences of indirect measurements and latent sources and the necessity of finding ways to resolve it. Furthermore, the accumulation of data from multiple subjects in order to shape a unified base for model search seems to be impossible even if there is a common causal structure shared by subjects. Problematic issues could also be the distinct but overlapping variables sets and the unknown time delays that result from the indirect measurement of the neural processes. Finally, the necessary reconstruction of activation influences, either with modeling joint time-sampled measurements of variables or modeling the as ‘equilibrium’ values resulting from an exogenous stimulation carries risks [96].

Dynamic Bayesian models

A temporal extension of Bayesian networks, the so-called dynamic Bayesian networks or dynamic probabilistic networks, which are class of graphical models, are also

proposed to address dynamic systems modeling [97, 98]. In comparison with Bayesian networks which indicate cumulative probability distribution over a set of random variables independent of time, dynamic Bayesian networks refer to a multi-dimensional expression of a random process [97]. Taken into account the dynamic nature of the process there are studies that use discrete dynamic Bayesian networks to clarify differences between healthy and control subjects or static Bayesian networks to model problems such as in speech recognition, target tracking and identification, genetics, probabilistic expert systems and medical diagnostic systems. A more recent apply of dynamic Bayesian networks is in modeling genomic regulation [98, 99].

Switching linear dynamic systems

The switching linear dynamic system for fMRI (SLDSf) has the ability to provide infinite variability over time in connectivity parameter values as well as instantaneous connectivity by probabilistically mixing a small number of static model regimes [100]. Basically, it models the task factor as a Markov random variable and its goal is the quantification of the overall quality and sufficiency of an identified model [101].

The linear convolution model used in order to express the observation equations used in sLDSf are:

$$y_t = \beta\varphi z_t + Dv_t + \zeta_t,\ \zeta \sim \mathbb{N}(0, R), \tag{4.59}$$

$$z_t = [x_t, x_{t-\tau}, x_{t-2\tau}, x_{t-3\tau}, \dots, x_{t-(h-1)\tau}]. \tag{4.60}$$

Where h errorless lagged copies of the signals x from $x_{t-(h-1)\tau}$ to x_t are contained to the variables z_t and y_t is the observation which concerns an instantaneous linear function of z_t at any observation level input v_t and noise ζ_t with a diagonal covariance matrix $R^{ij}=0$ for $i \neq j$. The matrix Φ refers to an a priori known set of basic vectors that connect the possible variability in the hemodynamic impulse response function (hIRF) such as a canonical hemodynamic response and its derivatives with respect to time and dispersion. Certain weights of specific areas are contained to matrix β aiming to produce a unique hIRF $\beta^i\Phi$. Thus, an equivalent between linear output $\beta^i\Phi Z_t^i$ and the regionally specific hemodynamic response arises. The estimation of three additional parameters per region is required in order to obtain SLDSf output equations with basis vectors. An iterative Bayesian Expectation Maximization algorithm is used to calculate these parameters [102].

Psychophysiological interactions (PPI)

Linear regression methods such as PPI are on the border between functional and effective connectivity. Although PPI has been proposed as a method for effective connectivity analysis, its simplicity on the other hand includes several weaknesses. For instance, in SPM package, PPI is performed in order to estimate task-dependent changes in the relationship between a seed region of interest and other voxels. That renders PPI as a more appropriate method for task-based functional connectivity analysis, as it fails when implemented on effective connectivity analysis studies [88, 92, 103].

4.2.5 Network analysis and graph theory

In fMRI graph analysis, neural networks are a collection of nodes that refer to basic elements within the system of interest and edges which are related to the associations among those elements [104]. Graph theory is addressed in order to model dynamic processes and relationships in physical, biological, social and information systems [91]. The description of brain networks can be achieved at levels, in microscale, mesoscale and macroscale or large-scale. Due to the technical restrictions and computational requirements, the majority of studies utilize large-scale networks [104].

Generally, the representation of a complex network is $G(N, K)$, where N refers to the number of nodes and K the number of edges in a graph G. There is a basic classification on graphs which include information about directionality. Thus, the graphs can be characterized as directed or undirected. Given an equal weight of 1 in every edge of the graph, the graph is unweighted (binary) but when different strengths exist at every edge, the graph is characterized as weighted. These distinctions are illustrated in Fig. 4.11.

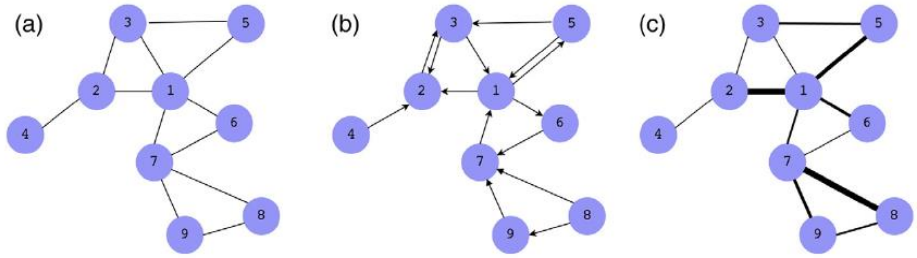

Figure 4.11: Types of a) undirected, b) directed and c) weighted networks [105].

The connectivity pattern of an undirected and unweighted graph $G(N, K)$, could be fully represented as an N×N symmetric square matrix, the adjacency matrix A. In the

case of edge existence between node i and j, the entry of α_{ij} (that ranges between 1 and N) is 1 and it takes the value of 0 in the opposite case [104].

There are some key properties of graph theory that define the topological patterns of the network. These are degree and degree distribution, small-world, network efficiency, nodal centrality, modularity and hierarchy. Below a short description of these notions follows.

The degree of node i in a graph is the number of edges that are connected to it. It can be calculated as $k_i = \sum_{j \in G} a_{ij}$, where a_{ij} is the i^{th} row and j^{th} column element of adjacency matrix A. The average degree which concerns the mean of degrees over all the nodes in G, estimates the size of the connected graph. The probability that refers to the fraction of nodes in the graph with degree k, is given by the degree distribution P(k). This degree distribution determines the classes of networks that features unique resilience concerning the removal of nodes.

The high local clustering that indicates high clustering coefficient C_p and the low minimum path length between any pair of nodes that indicates low characteristic path length, illustrate the small-worldness of a network. The clustering coefficient C_p, which estimates the length of local interconnectivity or cliquishness of a network, refers to the average of the clustering coefficients from all network nodes. For a given node i, its clustering coefficient C_i is calculated as:

$$C_i = 2E/k_i \times (k_i - 1), \tag{4.61}$$

where E is the number of connections among nodes neighbors and k_i is the degree of node i.

The characteristic path length refers to the average of the shortest path length between any pair of nodes. When the distance gets shorter, the routing efficiency is higher but in the case of multiple components, it generates problems as it becomes infinite. The 'harmonic mean' distance comes to solve this problem. It is worth noting that 'harmonic mean' distance corresponds to the inverse of global efficiency numerically.

The conditions that are satisfied in a real network taking into account its small-world properties are:

$$\gamma = {C_p}/{C_{p-rand}} > 1 \tag{4.62}$$

$$\lambda = {L_p}/{L_{p-rand}} \approx 1. \quad (4.63)$$

Where C_{p-rand} and L_{p-rand} are the mean clustering coefficient and characteristic path length of the mean random networks. Another representation in summary is:

$$\sigma = {\gamma}/{\lambda} > 1 \quad (4.64)$$

The low wiring cost renders small-world model attractive for complex brain networks description due to its modularized and integrated information processing.
Other measurements that are interwoven with graph analysis are the global and local efficiency, which measure the potential of model to transmit information at global and local scale. The global efficiency is described as:

$$E_{glob}(G) = \frac{1}{N(N-1)} \sum_{i \neq j \in G} \frac{1}{d_{ij}}, \quad (4.65)$$

where d_{ij} is the shorter path length between node i and j.

The local efficiency is described as:

$$E_{loc}(G) = \frac{1}{N} \sum_{i \in G} E_{glob}(G_i), \quad (4.66)$$

Where $E_{glob}(G_i)$ is the global efficiency of G_i the sub-graph composed of the neighbors of node i.

Another significant metric regarding the network efficiency is network cost, which estimates the expenses for its network construction.
In addition, nodal centrality evaluates the existence of the node into the network, by estimating its capability to transmit and share information with other nodes in a network. Degree centrality, nodal efficiency, closeness centrality and betweenness centrality are some of the metrics that are used through nodal centrality estimation. It can be expressed as:

$$E_i = \frac{1}{N-1} \sum_{j \neq i \in G} \frac{1}{d_{ij}}. \quad (4.67)$$

The nodal centrality, which assesses the average distance from a node to all the other nodes in a network, is given as:

$$C_i = \frac{N-1}{\sum_{j \neq i \in G} d_{ij}}. \quad (4.68)$$

The betweenness centrality defines the influence that one node exerts over the flow information between other nodes and its equation is:

$$B_i = \sum_{m \neq i \neq n \in G} \frac{\sigma_{mn}(i)}{\sigma_{mn}}, \quad (4.69)$$

Where σ_{mn} is the total number of the shorter paths from node m to node n and similarly $\sigma_{mn}(i)$ refers to those paths which pass through node i. It is common to use the characterization of hub to mention node which presents high centrality.

The description of the graph analysis measures becomes more robust with the use of notion modularity. It is related to the networks level ability to be coupled on modular or community structure. Mentioning modules, we refer to a set of nodes with thick connections among them but with weaker connections among the whole network. There are several optimization algorithms performing modularity through which localization and characterization of the modular structure in the brain is accomplished and thus the opportunity to understand the anatomical or functional components which are associated with specific biological functions is given.

Last, the concept of hierarchical networks is important to be mentioned. An hierarchical network contains hubs connected to nodes which in a different way are not connected to each other. This means that, the clustering coefficient value is lower if the degree is larger. The advantages of this organization are the better top-down relationships between nodes and it provides the minimization of the wiring cost. In contrast, it bears weaknesses regarding hubs attacking. This situation can be expressed with β value, an exponent of the power law relationship between clustering coefficient C and degree k, as:

$$C = k^{-\beta}. \tag{4.70}$$

A typical hierarchical structure is indicated by a large positive value of β [104, 106].

In the field of neuroimaging, graph theory is becoming a highly developing method that offers more graph operational and organizational measures into studies in order to investigate functional and structural connectivity [107], but there are also limitations. First of all, the nature of human brain consisting of neurons and physical elements renders the accurate estimation of the functional networks difficult. Taking into account that graph theory based on voxels or anatomically- or functionally-defined ROIs in order to draw conclusions, the analysis gets complicated when applied in a set of subjects, where nodes present differences. In conclusion, despite the careful selection of nodes in order to obtain accurate graphs, this seems to be impossible because of the inadequate knowledge concerning the brain field [91].

Chapter 5. Results

Imaging protocol

The fMRI data was acquired from MRI 1.5 Tesla (INTERA, Philips Medical System, Best, The Netherlands) of General University Hospital of Ioannina. The imaging protocol in both patients and control subjects included a T1-weighted high-resolution (0.86×0.86×1 mm) 3D spoiled gradient-echo sequence (TR/TE, 25/4.6ms), which was used for structural imaging and a single-shot multisection gradient EPI, which was used for BOLD functional images (TR/TE, 3000/50 ms; flip angle, 40°, matrix 64×64; section thickness, 5mm; gap, 0 mm). Each session consisted of 160 scans and lasted 480 seconds. The head of the subject was restrained with the use of cushions to minimize motion artifacts and the patients were advised to keep their eyes closed during the examination so as to minimize potential visual stimuli. Patients were awake during the examination, and they were instructed to remain still and avoid voluntary movements.

Study 1: Functional connectivity using data-driven method

In our study 13 late-onset RLS patients and 6 control healthy subjects took part. DICOM images received from MRI were transformed into image.img and image.hdr files with the use of SPM12 software package. Subjects with 4092 functional images produced 186 volume images and subjects with 3200 functional images produced 160 volume images, after having been transformed. The 150 anatomical DICOM images were transformed into 1 volume structural image. The fact that the produced number of volume functional images differed in some of the subjects was taken into consideration in the preprocessing stage, as the number of slices should be defined in slice-timing correction step.

The data preprocessing was carried out using SPM12 (http://www.fil.ion.ucl.ac.uk/spm/software/spm12/) and included the following steps:

1. slice-timing correction

   All the raw images were selected and the differences in image acquisition time between slices was corrected, prepending files with an ‘a’.

2. realignment (motion correction)

   All images were realigned according to the mean image of 186 functional images. The names of the realigned images have an extra ‘r’ as a prefix.

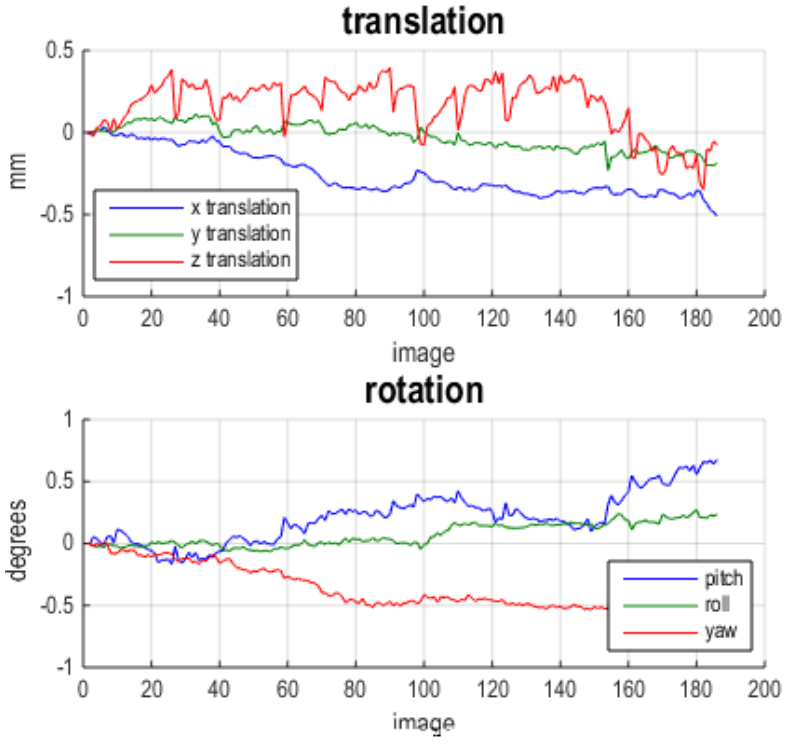

Figure 5.1: The estimated displacement and the rotation angles concerning BOLD fMRI time-series of an RLS patient.

3. Co-registration

   This step includes the implementation of co-registration between the structural and functional data that maximizes the mutual information. At the end of co-registration, the voxel-to-voxel affine transformation matrix is displayed, along with the histograms for the images in the original orientations and the final orientations. Also, the registered images are displayed.

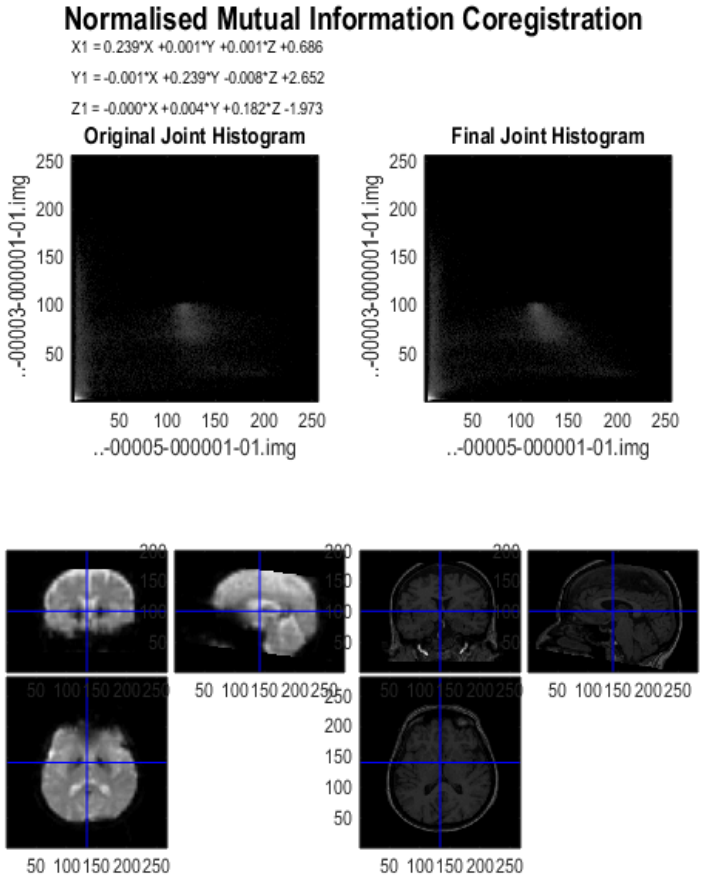

Figure 5.2: The co-registration step for an RLS subject.

4. Segmentation

   In this step, SPM12 produced gray and white matter images and a bias-field corrected structural image which is useful for the next preprocessing step.

5. Normalization

   In this step the previous realigned and resliced functional images and the preprocessed structural image are normalized in the MNI (Montreal Neurological Institute) space. The images have the prefix ‘w’.

6. Smoothing.

   This step includes the smoothing (or convolving) volume images with a Gaussian kernel of a specified width, which in this case is 8mm.

The fMRI analysis which aims to extract functional connectivity from data was accomplished following two different procedures, one based on data and another based on a model. In the first method, the Independent Component Analysis (ICA) was used, which is a widely used method particularly for studies which utilize resting-state fMRI data. The implementation of this method utilized the GroupICA/IVA of fMRI toolbox (GIFT) version 3.0b (http://mialab.mrn.org/software/gift). The ICA study of a group subjects requires the simultaneous analysis of all data. The dataset was divided into two separate databases, one for controls and another one for late-onset RLS patients, the analysis of which was done in a group context. In order to eliminate complicated computations, GIFT adopts the use of Principal Component Analysis. In the first step the data was reduced from 182 (the number of time points during experiment, after discarding the first four dummy volume images) into 36 principal components and afterwards into 24 components. The number of components was characterized as the most appropriate using the minimum description length algorithm indicating 25 independent components for the RLS group and 24 components for the group of controls. In the final dataset the infomax algorithm was used, which maximizes the information transfer from the input to the output of a network using a non-linear function (the most applications of ICA to fMRI use infomax since the sources of interest in this case are super gaussian in nature and the algorithm favors separation of super-gaussian sources) (Group ICA/IVA of fMRI Toolbox Manual). The final mixing matrix data was used in order to reconstruct spatial maps according to the courses of each participant and each component. For the 13 RLS subjects with one session, the GIFT program produced 325 spatial maps (13 participants × 25 Independent Components × 1 session = 325 spatial maps), respectively to ICA timepoints. Regarding control subjects the results were 144 spatial maps (6 participants × 24 Independent Components × 1 session = 144 spatial maps), respectively to ICA timepoints.

For each separate subject and component, the coordinates of the maximum voxel were recorded according to the z-score and afterwards a spatial sorting of components was achieved using maximum voxel criteria. This was also carried out in group context both of RLS and healthy subjects.

In order to estimate the spatial dependency of the automatic neuronal activity among different independent components, a functional connectivity network analysis was implemented using one-sample t-test of Mancovan toolbox v1.0 in order to produce the functional connectivity correlation matrices for patients and control groups.

Results

Studying the findings of each RLS subject, we found that the maximum voxel values exist in the superior temporal gyrus in the temporal lobe of the right cerebrum, the Declive in the posterior lobe of the left cerebellum, the cerebellar Tonsil in the posterior lobe of the left cerebellum as well as the cuneus in occipital lobe of the right cerebrum including Brodmann Area 18 (BA 18). Additional areas presenting important activations are the superior frontal gyrus in the frontal lobe of the left cerebrum including BA 6, the Nodule in anterior lobe of the right cerebellum, the sub-lobar areas of third and fourth ventricle of the right cerebrum and cerebellum respectively, the pons and midbrain in the left and right brainstem, the limbic lobe of both left and right cerebrum and Uncus of the left cerebrum, as well as the parahippocampal gyrus and BA 35.

In group level, the maximum z-score was located in voxels in the right cerebellum, particularly in Nodule in anterior lobe as well as in midbrain and pons in the left brainstem. Corpus Callosum which is located in extra-nuclear area in the left cerebrum and sub-lobar area in the third ventricle of the right cerebrum also revealed maximum activation (the table which includes in detail the coordinates and brain areas of each patient's components is in Table 7.2 in Appendix).

Concerning control subjects, the areas that are associated with great activation are in the right cerebrum and these are the cuneus and lingual gyrus in occipital lobe, fusiform gyrus in temporal lobe including BA 37, sub-lobar regions of lateral ventricle, Culmen and Nodule in anterior lobe and middle frontal gyrus in frontal lobe including BA 8. In the left cerebrum, the inferior frontal gyrus in the frontal lobe and corpus callosum are involved in maximum activation. Pons in both left and right brainstem present great activation as well as Medulla in the left brainstem. Additionally, it is necessary to record the regions Declive and fourth ventricle in the posterior lobe and sub-lobar regions of the right cerebellum respectively.

In group level similar findings were obtained while the significant areas are the Pons in the right Brainstem, the Declive in posterior lobe of right cerebellum, the lingual

gyrus in the occipital lobe and the parahippocampal gyrus in the limbic lobe of the left cerebrum as well as inter-hemispheric areas including the corpus callosum (table 7.1 in Appendix includes the maximum activations for each component of each healthy subject). It is worth noting that our study showed maximum activation also in inter-hemispheric areas in both RLS and controls group.

After implementing one sample t-test in two group datasets, T-maps, power spectra of each component and FNC (functional network connectivity) correlations among components were produced.

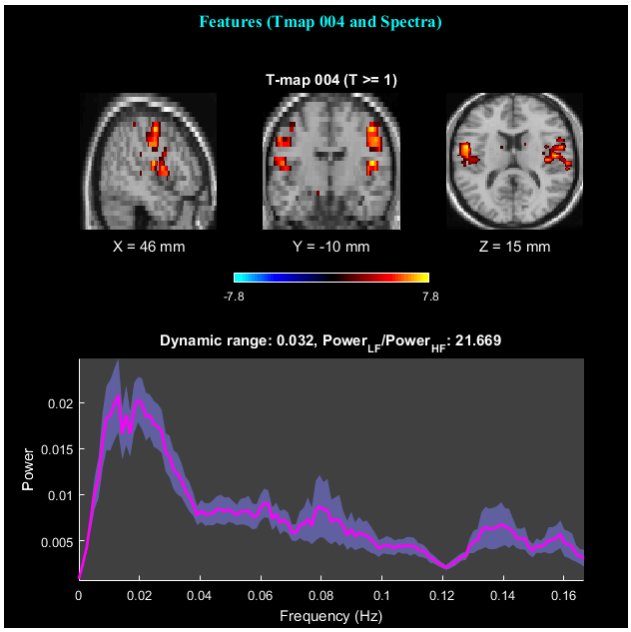

Figure 5.3: T-map and power spectra of the fourth component of RLS patients.

Concerning RLS subjects, the maximum correlation that is depicted in dark red in functional connectivity correlation matrix (Fig. 5.4) involves the components 7 [30, -76, 20] and 20 [6, -78, 5] which are the middle occipital and lingual gyrus in occipital lobe of the right cerebrum as well as the component 12 [6, -46, 0] and 18 [32, -68, -25] which are Culmen in anterior lobe and Uvula in posterior lobe of right cerebellum, respectively. Additional important functional connectivity was found between 22 [-6, -48, 35] and 15 [-30, 28, 50], 24 [6, -68, 55] with 21 [36, 20, 45] and 18 [32, -68, -25] with 20 [6, -78, 5] where the correlated areas are the precuneus in parietal lobe and superior frontal gyrus in frontal lobe of left cerebrum, middle frontal gyrus in frontal lobe of the right cerebrum and interhemispheric areas as well as the Uvula in posterior lobe and lingual gyrus in occipital lobe of right cerebrum.

Some of the areas that were found to have negative correlations were superior parietal lobule in parietal lobe and anterior cingulate in limbic lobe of right cerebrum involving the components 5 [12, -68, 65] and 2 [8, 44, 5] and the middle occipital gyrus in occipital lobe and the Insula in limbic Lobe of right cerebrum involving the components 7 [30, -76, 20] and 4 [46, -10, 15].

An important finding is the fact that the most significant positive correlation concerning controls were found between components 1 [48, 32, -10] with 5 [-18, -42, 5] and 3 [-28, 0, -25] with 14 [-36, -2, 65] which are the inferior frontal gyrus in frontal lobe of the right cerebrum and the parahippocampal gyrus in limbic lobe of the left cerebrum as well as the sub-gyral in temporal lobe of right cerebrum and middle frontal gyrus in frontal lobe of left cerebrum. The Tables 7.3 and Table 7.4 which include the regions of the components in the correlation matrix for both groups are in Appendix.

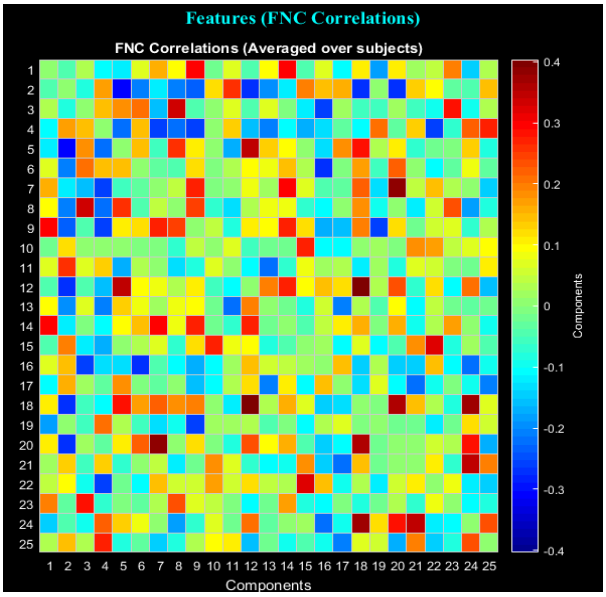

Figure 5.4: Functional connectivity correlation matrix of RLS subjects.

The following figure (Fig. 5.5) includes the functional connectivity correlation matrix of control subjects and depicts the correlation among their 24 components.

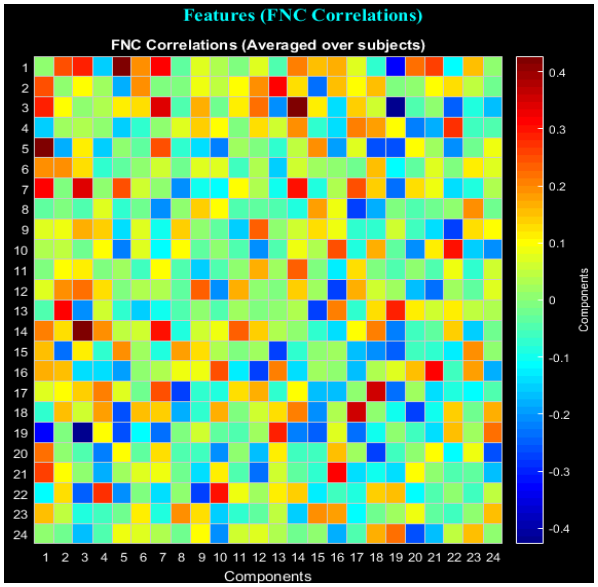

Figure 5.5: Functional connectivity correlation matrix of control subjects.

Discussion

After comparing the findings, we concluded that there are brain areas such as Pons in Brainstem or Cuneus in occipital lobe of the right cerebrum that always become active in resting state condition, regardless of disease existence, a fact that possibly renders them unrelated to RLS. In contrast, some areas such as cerebellar Tonsil in posterior lobe of the left cerebellum, Uncus in the limbic lobe of the right cerebrum, the third ventricle in sub-lobar area of the right cerebrum or amygdala in parahippocampal gyrus in the limbic lobe of the right cerebrum that appeared in the RLS group denoting their effect in the disease lead to a different understanding of the brain compared with healthy subjects'.

Functional connectivity analysis led to similar findings of previous studies which focused on the correlation of precuneus in the parietal lobe and the inferior frontal gyrus in the frontal lobe of the right cerebrum. It is also worth noting the positive correlation of the parahipocampal gyrus in limbic lobe of the left cerebrum with the Culmen in anterior lobe of the right cerebellum, as well as the higher correlation of precuneus in parietal lobe of left cerebrum with Insula in sub-lobar area of left cerebrum. This high correlation among these components does not occur in control subjects group.

These findings are in line with the bibliography that concerns the investigation of RLS.

Study 2: Functional connectivity using seed-based analysis

Following a different approach compared to the previous one, we implemented the CONN functional connectivity toolbox v17 (https://www.nitrc.org/projects/conn) in order to extract functional connectivity measures using seed-to-voxel correlation mapping. This approach calculates the temporal correlation between brain activity of a given region and all other regions using a General Linear Model approach [108]. Although we had already preprocessed data using SPM12 of the previous analysis, we added the raw structural and functional data in CONN. The aim was to follow the preprocessing pipeline of CONN so that its automated and simplified procedure would be established. Since the data undergoes a similar preprocess, as this software calls SPM12 to implement this step, its effectiveness is secured. In our study, we selected the default preprocessing pipeline for volume-based analyses which follows the following steps: functional realignment and unwarping (subject motion estimation and correction), functional center to (0, 0, 0) coordinates (translation), functional slice-timing correction, functional outlier detection (ART-based identification of outlier scans for scrubbing), functional direct segmentation and normalization (simultaneous GM/WM/CSF segmentation and MNI normalization), structural center to (0, 0, 0) coordinates (translation), structural segmentation and normalization (simultaneous GM/WM/CSF segmentation and MNI normalization), functional smoothing (spatial convolution with Gaussian kernel). Additionally, in order to remove physiological subject motion and other confounding effects from BOLD signal, a denoising clean up step followed.

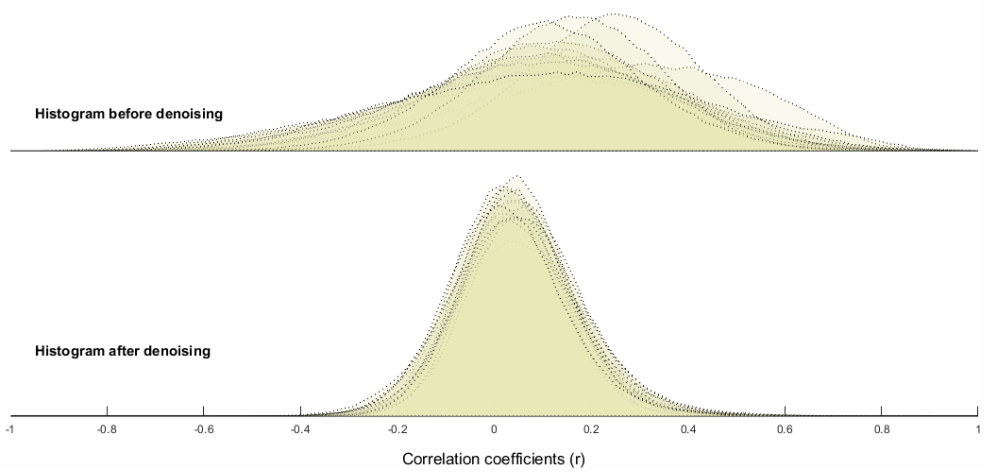

Figure 5.6: Histogram of functional connectivity between any pair of voxels of all subjects before and after denoising.

We compared the functional connectivity of the middle frontal gyrus in the frontal lobe, the occipital lobe and the thalamus in both left and right cerebrum as well as in the precuneus cortex (the tables with the results are in Appendix). The selection of seeds in seed-to-voxel analyses was based on previous knowledge as it has been proven that the regions involving these seeds are responsible for the RLS.

Results

Indicatively, the following Table (Table 5.1) presents the coordinates of the maximum voxel, the size of the cluster, the associated brain areas and their figures that resulted from a seed-to-voxel analysis considering as seed the middle frontal gyrus of the left cerebrum.

Table 5.1: The brain areas that are functionally connected with the middle frontal gyrus of the left cerebrum concerning RLS group.

MNI coordinates of maximum voxel	Cluster size (voxels)	Brain areas	Size p-FWE	Size p-unc	Peak p-FWE	Peak p-unc
[-38, 6, 42]	40754	R Cerebrum, Middle Frontal Gyrus	0.000000	0.000000	0.000000	0.000000
[52, -60, -28]	1545	R Cerebellum, Posterior Lobe, Declive, GM	0.000000	0.000000	0.613404	0.000008
[-60, -54, -16]	1330	L Cerebrum, Temporal Lobe, Inferior Temporal Gyrus, GM, BA 37	0.000000	0.000000	0.424448	0.000004
[-18, -90, -40]	1041	Left Cerebellum, Posterior Lobe, Tuner, GM	0.000000	0.000000	0.165311	0.000001
[-8, -6, 6]	657	L Cerebrum, Sub-lobar, Thalamus, GM	0.000000	0.000000	0.577960	0.000007
[66, -40, -16]	583	R Cerebrum, Temporal Lobe, Middle Temporal Gyrus	0.000001	0.000000	0.246651	0.000001
[16, 14, 12]	427	R Cerebrum, Sub-lobar, Caudate, GM, Caudate Body	0.000033	0.000001	0.488107	0.000005
[-18, -100, -6]	206	L Occipital Lobe, Occipital Lobe, Cuneus, WM	0.005853	0.000253	0.128142	0.000001
[-56, 0, -30]	165	L Cerebrum, Temporal Lobe, Fusiform Gyrus, GM, BA 20	0.018173	0.000789	0.963490	0.000048
[-38, -66, -22]	128	L Cerebrum, Occipital Lobe, Fusiform Gyrus	0.054265	0.002401	0.998160	0.000126
[-38, 18, -36]	124	L Cerebrum, Temporal Lobe, Inferior Temporal Gyrus	0.061343	0.002725	0.987170	0.000072

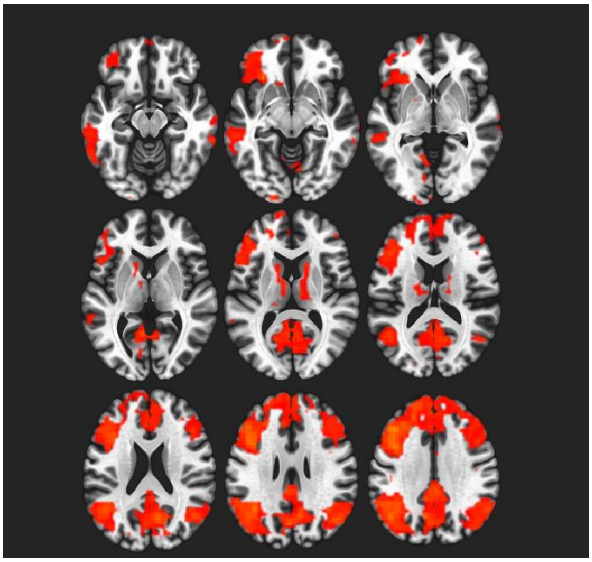

Figure 5.7: The activation in slices of RLS patients considering the left middle frontal gyrus as seed.

To make our study more robust, we assumed the middle frontal gyrus of the left cerebrum as seed in an additional seed-based analysis concerning the controls group.

Table 5.2: The functionally connected areas of the middle frontal gyrus of the left cerebrum in controls group.

MNI coordinates of maximum voxel	Cluster size (voxels)	Brain areas	Size p-FWE	Size p-unc	Peak p-FWE	Peak p-unc
[-36, 30, 32]	2199	L Cerebrum, Frontal Lobe, Middle Frontal Gyrus, GM, BA 9	0.000000	0.000000	0.222985	0.000001
[-42, -66, 54]	894	Left Cerebrum, Parietal Lobe, Superior Parietal Lobe, GM, BA 7	0.000000	0.000000	0.097323	0.000000
[40, 30, 38]	515	R Cerebrum, Frontal Lobe, Middle Frontal Gyrus	0.000000	0.000000	0.317282	0.000001
[-36, -76, -34]	494	L Cerebellum, Posterior Lobe, Uvula, GM	0.000000	0.000000	0.566713	0.000002
[-6, -64, 60]	465	L Cerebrum, Parietal Lobe, Precuneus, GM, BA 7	0.000000	0.000000	0.252949	0.000001
[42, -78, 38]	418	R Cerebrum, Parietal Lobe, Precuneus, GM, BA 19	0.000000	0.000000	0.999867	0.000009
[0, 24, 42]	337	Inter-Hemispheric	0.000000	0.000000	0.999035	0.000005
[22, -78, -46]	305	R Cerebellum, Posterior Lobe, Interior Semi-Lunar Lobule, GM	0.000000	0.000000	0.311366	0.000001
[-2, -36, 42]	256	L Cerebrum, Limbic Lobe, Cingulate Gyrus	0.000001	0.000000	0.999932	0.000011

[-24, 0, -30]	163	L Cerebrum, Limbic Lobe, Parahippocampal Gyrus, WM	0.000039	0.000004	0.999988	0.000017
[34, 6, 66]	105	Right Cerebrum, Frontal Lobe, Middle Frontal Gyrus, GM, BA 6	0.000868	0.000085	0.999992	0.000019

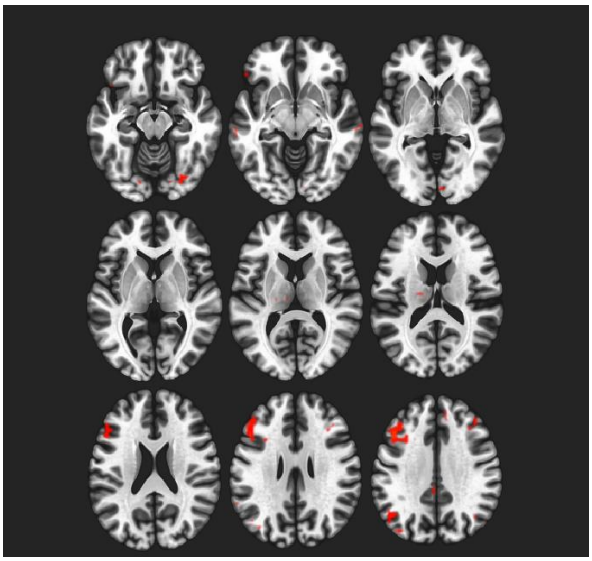

Figure 5.8: The activation in slices for controls considering the middle frontal gyrus of the left cerebrum as seed.

Discussion

Compared with ICA analysis, seed-based analysis presented similar findings. These results agree with the bibliography findings. Furthermore, it is obvious that this toolbox usage offers great visualization concerning activation maps giving the ability to switch among subjects. It is inferior to other methods when direct contact and intervention in code is needed.

Study 3: Effective connectivity using spectral Dynamic Causal Modeling

As already referred to a previous chapter, the effective connectivity analysis can be studied by model-based approaches including structural equation modeling (SEM) or dynamic causal modeling (DCM) and data-driven approaches including Granger causality analysis [108].

According to the first method we implement spectral DCM in order to investigate the endogenous effective connectivity in both RLS and control groups. The aim of this method is to model BOLD signal when there are no exogenous inputs (driving or

modulatory), a fact that renders it suitable for its implementation in resting-state fMRI data.

The spectral DCM analysis was performed using DCM12 routine implemented in SPM12. For each subject, eight regions of interest (ROIs) were selected. The ROIs of spectral DCM analysis (Table 5.3) were selected according to their increased level of involvement in RLS as long as both our and previous studies revealed either high activation or high functional connectivity. ROIs were defined as spheres with a radius of 8mm centered at the peak coordinate of the component map produced by the previous ICA study.

Time-series from the ROIs were created as the residuals of a general linear model (GLM). These regressors that were included in this model were the six rigid body realignment parameters to model the movement correlated effects, one contrast regressor to model the baseline that was used in the extractions to constrain the extraction of BOLD time-series within the brain, cosine basis functions to model possible signal drift and aliased respiratory and cardiac signals and a high-pass filter of 1/128 Hz to remove possible ultraslow fluctuations [107].

Table 5.3: ROIs selected for the spectra DCM analysis.

	ROIs	**Center of ROI[5]**
1	Right Cerebrum, Parietal Lobe, Precuneus, GM, BA 7 (RPP)	[6, -73, 56]
2	Right Cerebrum, Sub-lob, Thalamus, GM, Mammillary Body (RTM)	[13, -17, -5]
3	Right Cerebrum, Frontal Lobe, Inferior Frontal Gyrus, WM (RFI)	[36, 25, -16]
4	Left Cerebrum, Frontal Lobe, Middle Frontal Gyrus, GM, BA 46 (RFM)	[-46, 31, 20]
5	Right Cerebrum, Limbic Lobe, Parahippocampal Gyrus, GM, 35 (RLP)	[23, -21, -23]
6	Right Cerebrum, Anterior Lobe, Culmen, GM (RAC)	[6, -46, -5]
7	Right Cerebrum, Occipital Lobe, Middle Frontal Gyrus, WM (ROM)	[29, -79, 19]
8	Right Cerebrum, Temporal Lobe, Superior Temporal Gyrus (RTS)	[53, 11, -6]

[5] The coordinates were transformed from Talairach into MNI space.

After extracting the resting-state fMRI time-series from all eight ROIs (Fig. 5.9), a fully-connected model which has bi-directional connections between any pair of ROIs was specified for each subject (Fig. 5.10). The following table (Table 5.4) includes the effective connectivity parameters of the first RLS subject, where the matrix elements represent the effective influence between regions. The effective connectivity parameters of the other subjects are included in the Appendix.

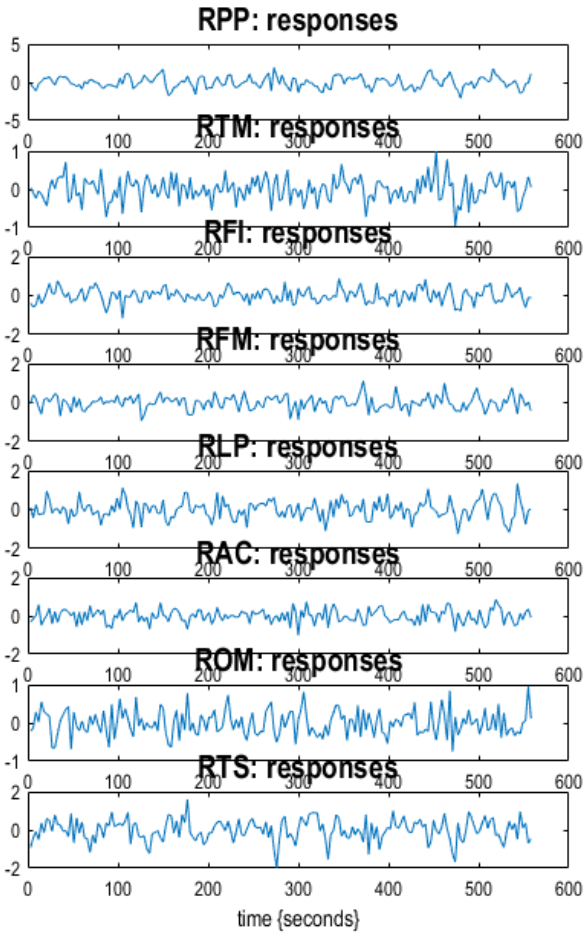

Figure 5.9: Time-series extraction of most significant ROIs of the first RLS patient.

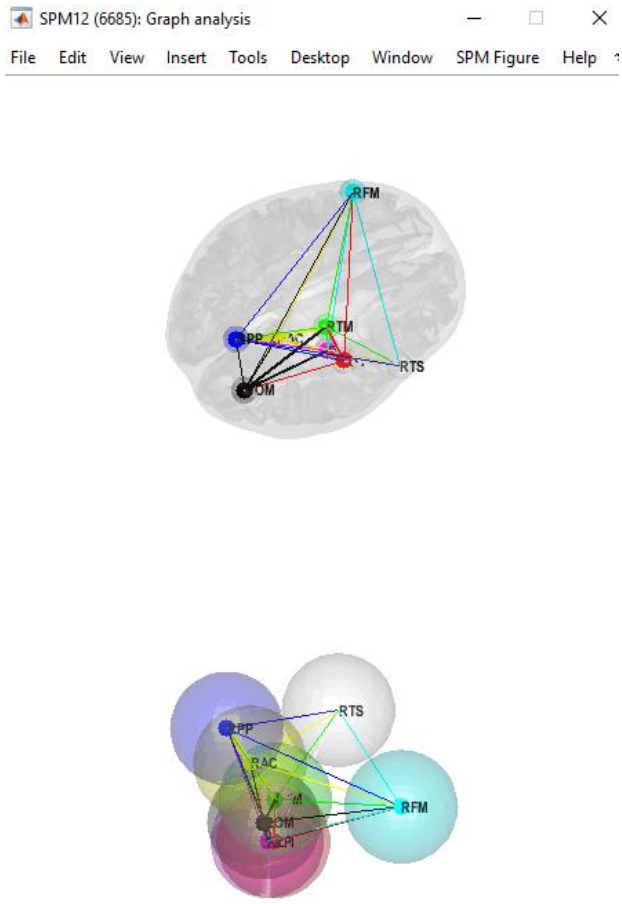

Figure 5.10: The fully-connected model with bi-directional connections between any pair of ROIs and effective connectivity parameters for the first RLS subject.

Table 5.4: Effective connectivity parameters of the first RLS subject.

	RPP	**RTM**	**RFI**	**RFM**	**RLP**	**RAC**	**ROM**	**RTS**
RPP	-0.9890	0.7336	-0.0422	0.1822	-0.4870	0.3665	0.0458	-0.0454
RTM	-0.0399	-0.8527	-0.0752	0.0118	-0.1920	-0.0336	-0.2775	-0.0080
RFI	-0.0390	0.1917	-0.8813	0.0729	-0.0024	-0.0801	0.4542	0.00460
RFM	-0.0142	-0.1228	0.0608	0.2077	0.2743	-0.1802	0.0448	-0.0026
RLP	-0.0046	0.9833	0.0327	0.0559	-0.9029	0.0299	-1.3031	-0.0977
RAC	-0.1492	0.7109	0.1707	0.0115	0.3804	-0.7155	-1.1320	-0.0695
ROM	-0.0763	-0.1307	-0.0384	-0.0277	0.2974	-0.0438	-0.5457	0.0364
RTS	-0.0262	0.1929	0.1842	0.0186	-0.1562	0.0321	0.2958	0.1465

The selection of the model expressing the data is a serious matter and it is necessary that the model fitting as well as the model's complexity are taken into consideration. After evaluating the effective connectivity parameters, a Bayesian Model Selection was chosen and fixed effects inference method (FFX) followed in order to compare the winning model that effectively describes the data. Observing the connectivity

parameters from tables, the most frequent appearing areas with the highest values were selected in order to construct the desirable combination of areas. As this results in a large number of models, researchers should decide on which areas they should focus on.

Indicatively, we relied on the first ROI (precuneus in parietal lobe of right cerebrum) and its highly associated areas as they appeared more often in the tables, in order to construct the first model and the third ROI (inferior frontal gyrus in frontal lobe of right cerebrum) with the associated areas in order to construct the second model (Fig. 5.11). The second one is obviously the winning model indicating that this network has greater influence over the other one concerning the first RLS subject (Fig. 5.12).

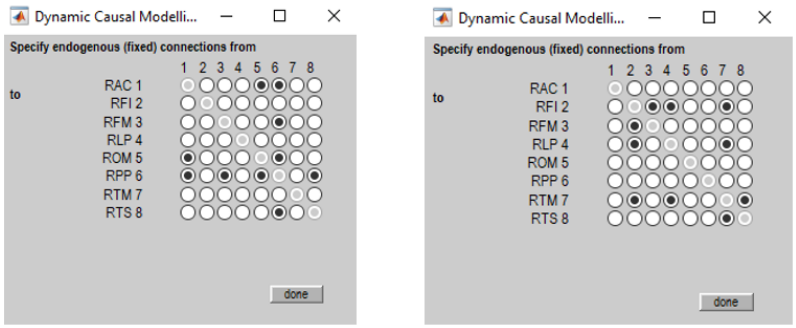

Figure 5.11: The desirable specification of endogenous (fixed) connections for the model comparison.

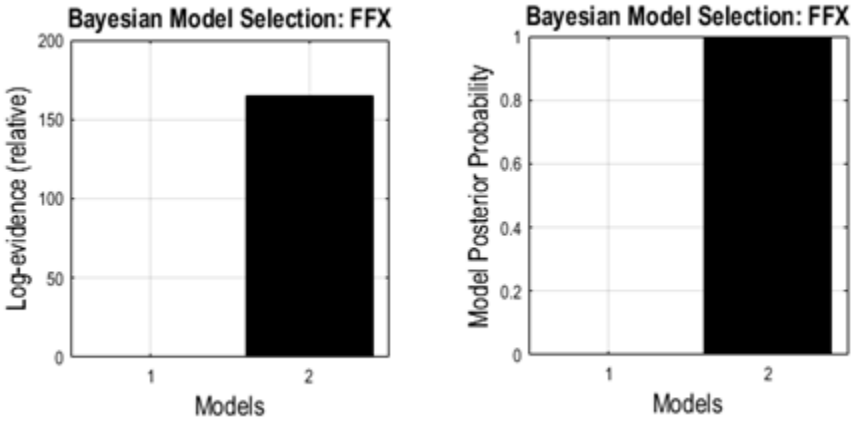

Figure 5.12: The 'winning' model is the second one using Fixed Effects inference method (FFX).

Chapter 6. Conclusions

6.1 Discussion

RLS is a common neurological disorder accompanied with annoying feelings during state of rest. The irresistible urge to move legs or sometimes arms in order to reduce the uncomofortable sensations affects the quality of life of patients. The pathophysiology of the disease has been formed after realizing that with the implementation of dopaminerging agents and iron supplements, the symptoms were improved, assuming that the possible source of problem is located in the central nervous system and in the levels of iron and dopamine.

MRI studies have led to results concerning low iron levels in specific brain areas as well as PET and SPECT studies focused on the amount of disturbunces in dopamine receptors. fMRI is a contemporary application of MRI which is used in ordrer to locate brain areas which are activated when the subject carries out a task or is in resting state. Subsequently, patterns with connected and disconnected brain areas can be formed in order to shed light on the pathology of a disease compared with connectivity patterns

of healthy subjects. The differentiation of brain network associations between healthy subjects and patients can lead to significant findings in diagnosis or therapy.

In this research work, we attempted to describe the sleep disorder of RLS from the perspective of brain connectivity using fMRI, searching the most appropriate analysis method. We utilized data from 13 RLS subjects with late-onset RLS without treatment and 6 healthy subjects. We first tried to find the activated areas in patients' brains as well as in controls' brains, using an already implemented method (ICA). This was a supporting attempt for us to verify the findings and be based on reliable results. Accompanied with the aforementioned data-driven method for functional connectivity analysis, a model-based analysis mehod was used and compared with the previous one. It was found that areas such as cerebellar Tonsil in posterior lobe of left cerebellum or Amygdala and parahippocampal gyrus in limbic lobe of left cerebrum showed greater activation than controls group. Concerning functional connectivity, there were areas that revealed a different correlation compared with controls. The model-based method provides results that aim to be more specific that data-driven methods giving greater visualization of brain. As far as effective connectivity is concerned, it was found that the possibility of implementing spectral Dynamic Causal Modeling on data provides useful information going beyond the restricted and much used methods.

6.2 Limitations

Concerning the proposed methodology of the current study, we concluded that in both functional and effective connectivity analysis, the methods that were followed have given reliable results. However, because of the fact that we implemented model-based analysis methods, the regions of interest were necessary to be defined and this is a limitation. Furthermore, the complexity of the effective connectivity models and the large number of areas and their combinations that are necessary in order to construct each model, render the determination of the best model a not simple matter.

6.3 Future work

The target of this work was not to prove that there is only one method describing the RLS data, as there is no such thing, but to present both advantages and disadvantages of each method. The selection of the most appropriate method depends on the researchers' incentives and the aim of each study. Since RLS has not been clarified yet, there will always be the need for further study and analysis.

References

[1] W. C. Dement, "Knocking on Kleitman's door: the view from 50 years later," *Sleep medicine reviews,* vol. 7, pp. 289-292, 2003.

[2] P. Margariti, "Functional Magnetic Resonance Imaging (fMRI) of the brain in patients with restless legs syndrome," *Doctoral Thesis, Medical School of University of Ioannina,* 2015.

[3] M. J. Thorpy, "Classification of sleep disorders," *Neurotherapeutics,* vol. 9, pp. 687-701, 2012.

[4] S. Ovallath and P. Deepa, "Restless legs syndrome," *Journal of Parkinsonism and Restless Legs Syndrome,* vol. 2, pp. 49-57, 2012.

[5] J. Ku, Y. S. Lee, H. Chang, C. J. Earley, R. P. Allen, and Y. W. Cho, "Default mode network disturbances in restless legs syndrome/Willis–Ekbom disease," *Sleep medicine,* vol. 23, pp. 6-11, 2016.

[6] J. Ku, Y. W. Cho, Y. S. Lee, H.-J. Moon, H. Chang, C. J. Earley, *et al.*, "Functional connectivity alternation of the thalamus in restless legs syndrome patients during the asymptomatic period: a resting-state connectivity study using functional magnetic resonance imaging," *Sleep medicine,* vol. 15, pp. 289-294, 2014.

[7] Y. Chang, H. W. Chang, H. Song, J. Ku, C. J. Earley, R. P. Allen, *et al.*, "Gray matter alteration in patients with restless legs syndrome: a voxel-based morphometry study," *Clinical imaging,* vol. 39, pp. 20-25, 2015.

[8] S. Guo, J. Huang, H. Jiang, C. Han, J. Li, X. Xu, *et al.*, "Restless Legs Syndrome: from pathophysiology to clinical diagnosis and management," *Frontiers in aging neuroscience,* vol. 9, p. 171, 2017.

[9] G. Rizzo, C. Tonon, D. Manners, C. Testa, and R. Lodi, "Imaging brain functional and metabolic changes in restless legs syndrome," *Current neurology and neuroscience reports,* vol. 13, p. 372, 2013.

[10] R. P. Allen and C. J. Earley, "Restless legs syndrome: a review of clinical and pathophysiologic features," *Journal of Clinical Neurophysiology,* vol. 18, pp. 128-147, 2001.

[11] R. P. Allen, D. L. Picchietti, D. Garcia-Borreguero, W. G. Ondo, A. S. Walters, J. W. Winkelman, *et al.*, "Restless legs syndrome/Willis–Ekbom disease

diagnostic criteria: updated International Restless Legs Syndrome Study Group (IRLSSG) consensus criteria–history, rationale, description, and significance," *Sleep medicine,* vol. 15, pp. 860-873, 2014.

[12] A. Salminen, "Peripheral Hypoxia and Autonomic Responses in Restless Legs Syndrome," *Academic dissertation, School of Medicine of the University of Tampere,* 2015.

[13] R. Jones and A. E. Cavanna, "The neurobiology and treatment of restless legs syndrome," *Behavioural neurology,* vol. 26, pp. 283-292, 2013.

[14] E. C. Schulte, "Genetic variants in restless legs syndrome and Parkinson´ s disease: the rare, the common and everything in between," Technische Universität München, 2013.

[15] R. E. Salas, C. E. Gamaldo, and R. P. Allen, "Update in restless legs syndrome," *Current opinion in neurology,* vol. 23, p. 401, 2010.

[16] B. B. Koo, K. Bagai, and A. S. Walters, "Restless legs syndrome: current concepts about disease pathophysiology," *Tremor and Other Hyperkinetic Movements,* vol. 6, 2016.

[17] Z. Gan-Or, S. Zhou, A. Johnson, J. Y. Montplaisir, R. P. Allen, C. J. Earley, *et al.,* "Case–Control and Family-Based Association Study of Specific PTPRD Variants in Restless Legs Syndrome," *Movement Disorders Clinical Practice,* vol. 3, pp. 460-464, 2016.

[18] J. Drgonova, D. Walther, K. J. Wang, G. L. Hartstein, B. Lochte, J. Troncoso, *et al.,* "Mouse model for protein tyrosine phosphatase D (PTPRD) associations with restless leg syndrome or Willis-Ekbom disease and addiction: reduced expression alters locomotion, sleep behaviors and cocaine-conditioned place preference," *Molecular Medicine,* vol. 21, p. 717, 2015.

[19] C. J. Earley, G. R. Uhl, S. Clemens, and S. Ferré, "Connectome and molecular pharmacological differences in the dopaminergic system in restless legs syndrome (RLS): plastic changes and neuroadaptations that may contribute to augmentation," *Sleep medicine,* vol. 31, pp. 71-77, 2017.

[20] A. Sehgal and E. Mignot, "Genetics of sleep and sleep disorders," *Cell,* vol. 146, pp. 194-207, 2011.

[21] H. Moore IV, J. Winkelmann, L. Lin, L. Finn, P. Peppard, and E. Mignot, "Periodic leg movements during sleep are associated with polymorphisms in

BTBD9, TOX3/BC034767, MEIS1, MAP2K5/SKOR1, and PTPRD," *Sleep*, vol. 37, pp. 1535-1542, 2014.

[22] P. J. P Matthews, "Functional magnetic resonance imaging," *Neurology, Neurosurgery & Psychiatry*, vol. 75, pp. 6-12, 2004.

[23] P. M. M. P. Jezzard, and Stephen M. Smith, "Functional MRI: An Introduction to Methods," 2001.

[24] C. Stippich, "Clinical functional MRI. Presurgical functional neuroimaging," 2007.

[25] S. A. Huettel, A. W. Song, and G. McCarthy, *Functional magnetic resonance imaging* vol. 1: Sinauer Associates Sunderland, MA, 2004.

[26] S. Ogawa, T.-M. Lee, A. R. Kay, and D. W. Tank, "Brain magnetic resonance imaging with contrast dependent on blood oxygenation," *Proceedings of the National Academy of Sciences*, vol. 87, pp. 9868-9872, 1990.

[27] N. K. Logothetis and B. A. Wandell, "Interpreting the BOLD signal," *Annu. Rev. Physiol.*, vol. 66, pp. 735-769, 2004.

[28] K. Li, L. Guo, J. Nie, G. Li, and T. Liu, "Review of methods for functional brain connectivity detection using fMRI," *Computerized Medical Imaging and Graphics*, vol. 33, pp. 131-139, 2009.

[29] R. A. Poldrack, J. A. Mumford, and T. E. Nichols, *Handbook of functional MRI data analysis*: Cambridge University Press, 2011.

[30] E. E. Tripoliti, "Automated analysis of brain function in patients with Alzheimer disease bases on random forests algorithm," *Doctoral Thesis, Department of Computer Science & Engineering, University of Ioannina*, 2012.

[31] J. A. Detre and T. F. Floyd, "Functional MRI and its applications to the clinical neurosciences," *The neuroscientist*, vol. 7, pp. 64-79, 2001.

[32] C. Mulert and L. Lemieux, *EEG-fMRI: physiological basis, technique, and applications*: Springer Science & Business Media, 2009.

[33] E. E. Tripoliti and D. I. Fotiadis, "Recent developments in computer methods for fMRI data processing," in *Biomedical Engineering*, ed: InTech, 2009.

[34] M. D. Fox and M. E. Raichle, "Spontaneous fluctuations in brain activity observed with functional magnetic resonance imaging," *Nature reviews neuroscience*, vol. 8, p. 700, 2007.

[35] J. E. Chen and G. H. Glover, "Functional magnetic resonance imaging methods," *Neuropsychology review*, vol. 25, pp. 289-313, 2015.

[36] O. Josephs and R. N. Henson, "Event-related functional magnetic resonance imaging: modelling, inference and optimization," *Philosophical Transactions of the Royal Society of London B: Biological Sciences,* vol. 354, pp. 1215-1228, 1999.

[37] M. H. Lee, C. D. Smyser, and J. S. Shimony, "Resting-state fMRI: a review of methods and clinical applications," *American Journal of Neuroradiology*, 2012.

[38] M. Daliri and M. Behroozi, "Advantages and disadvantages of resting state functional connectivity magnetic resonance imaging for clinical applications," *OMICS J Radiology,* vol. 3, p. e123, 2013.

[39] T. Takamura and T. Hanakawa, "Clinical utility of resting-state functional connectivity magnetic resonance imaging for mood and cognitive disorders," *Journal of Neural Transmission,* vol. 124, pp. 821-839, 2017.

[40] D. Orringer, D. R. Vago, and A. J. Golby, "Clinical applications and future directions of functional MRI," in *Seminars in neurology*, 2012, p. 466.

[41] G. H. Glover, "Overview of functional magnetic resonance imaging," *Neurosurgery Clinics,* vol. 22, pp. 133-139, 2011.

[42] N. K. Logothetis, "What we can do and what we cannot do with fMRI," *Nature,* vol. 453, p. 869, 2008.

[43] B. C. Dickerson, "Advances in functional magnetic resonance imaging: technology and clinical applications," *Neurotherapeutics,* vol. 4, pp. 360-370, 2007.

[44] G. Rizzo, X. Li, S. Galantucci, M. Filippi, and Y. W. Cho, "Brain imaging and networks in restless legs syndrome," *Sleep medicine,* vol. 31, pp. 39-48, 2017.

[45] F.-M. Lu and Z. Yuan, "PET/SPECT molecular imaging in clinical neuroscience: recent advances in the investigation of CNS diseases," *Quantitative imaging in medicine and surgery*, vol. 5, p. 433, 2015.

[46] C.-C. Lin, Y.-M. Fan, G.-Y. Lin, F.-C. Yang, C.-A. Cheng, K.-C. Lu, *et al.*, "99mTc-TRODAT-1 SPECT as a potential neuroimaging biomarker in patients with restless legs syndrome," *Clinical nuclear medicine,* vol. 41, pp. e14-e17, 2016.

[47] J. Haba-Rubio, L. Staner, C. Petiau, G. Erb, T. Schunck, and J. Macher, "Restless legs syndrome and low brain iron levels in patients with haemochromatosis," *Journal of Neurology, Neurosurgery & Psychiatry*, vol. 76, pp. 1009-1010, 2005.

[48] P. Margariti, L. Astrakas, S. Tsouli, G. Hadjigeorgiou, S. Konitsiotis, and M. Argyropoulou, "Investigation of unmedicated early onset restless legs syndrome by voxel-based morphometry, T2 relaxometry, and functional MR imaging during the night-time hours," *American Journal of Neuroradiology*, 2011.

[49] H.-J. Moon, Y. Chang, Y. S. Lee, H. J. Song, H. W. Chang, J. Ku, *et al.*, "T2 relaxometry using 3.0-tesla magnetic resonance imaging of the brain in early- and late-onset restless legs syndrome," *Journal of Clinical Neurology*, vol. 10, pp. 197-202, 2014.

[50] X. Li, R. P. Allen, C. J. Earley, H. Liu, T. E. Cruz, R. A. Edden, *et al.*, "Brain iron deficiency in idiopathic restless legs syndrome measured by quantitative magnetic susceptibility at 7 tesla," *Sleep medicine*, vol. 22, pp. 75-82, 2016.

[51] J. W. Winkelman, L. Schoerning, S. Platt, and J. E. Jensen, "Restless legs syndrome and central nervous system gamma-aminobutyric acid: preliminary associations with periodic limb movements in sleep and restless leg syndrome symptom severity," *Sleep medicine*, vol. 15, pp. 1225-1230, 2014.

[52] E. E. Tripoliti, D. I. Fotiadis, and K. Veliou, "Diffusion Tensor Imaging and Fiber Tractography," in *Handbook of Research on Advanced Techniques in Diagnostic Imaging and Biomedical Applications*, ed: IGI Global, 2009, pp. 229-246.

[53] Y. Chang, J. S. Paik, H. J. Lee, H. W. Chang, H.-J. Moon, R. P. Allen, *et al.*, "Altered white matter integrity in primary restless legs syndrome patients: diffusion tensor imaging study," *Neurological research*, vol. 36, pp. 769-774, 2014.

[54] C. Liu, Z. Dai, R. Zhang, M. Zhang, Y. Hou, Z. Qi, *et al.*, "Mapping intrinsic functional brain changes and repetitive transcranial magnetic stimulation neuromodulation in idiopathic restless legs syndrome: a resting-state functional magnetic resonance imaging study," *Sleep medicine*, vol. 16, pp. 785-791, 2015.

[55] J. W. Choi, M. H. Jeong, S. J. Her, B. U. Lee, K. S. Cha, K.-Y. Jung, *et al.*, "Abnormal Sleep Delta Rhythm and Interregional Phase Synchrony in Patients with Restless Legs Syndrome and Their Reversal by Dopamine Agonist Treatment," *Journal of Clinical Neurology*, vol. 13, pp. 340-350, 2017.

[56] Y. Zhuo, Y. Wu, Y. Xu, L. Lu, T. Li, X. Wang, *et al.*, "Combined resting state functional magnetic resonance imaging and diffusion tensor imaging study in

patients with idiopathic restless legs syndrome," *Sleep medicine,* vol. 38, pp. 96-103, 2017.

[57] M. A. Lindquist, "The statistical analysis of fMRI data," *Statistical science,* vol. 23, pp. 439-464, 2008.

[58] M. Könönen, "The mathematical backround of SPM99," *Academic Dissertation, Department of Applied Physics, University of Kuopio,* 2004.

[59] W. Liao, D. Mantini, Z. Zhang, Z. Pan, J. Ding, Q. Gong, *et al.*, "Evaluating the effective connectivity of resting state networks using conditional Granger causality," *Biological cybernetics,* vol. 102, pp. 57-69, 2010.

[60] R. Sladky, K. J. Friston, J. Tröstl, R. Cunnington, E. Moser, and C. Windischberger, "Slice-timing effects and their correction in functional MRI," *Neuroimage,* vol. 58, pp. 588-594, 2011.

[61] K. J. Friston, "Functional and effective connectivity in neuroimaging: a synthesis," *Human brain mapping,* vol. 2, pp. 56-78, 1994.

[62] K. J. Friston, "Functional and effective connectivity: a review," *Brain connectivity,* vol. 1, pp. 13-36, 2011.

[63] A. A. Elseoud, "EXPLORING FUNCTIONAL BRAIN NETWORKS USING INDEPENDENT COMPONENT ANALYSIS," *Academic Dissertation, Faculty of Medicine, University of Oulu,* 2013.

[64] E. W. Lang, A. M. Tomé, I. R. Keck, J. Górriz-Sáez, and C. G. Puntonet, "Brain connectivity analysis: a short survey," *Computational intelligence and neuroscience,* vol. 2012, p. 8, 2012.

[65] P. Hagmann, L. Jonasson, P. Maeder, J.-P. Thiran, V. J. Wedeen, and R. Meuli, "Understanding diffusion MR imaging techniques: from scalar diffusion-weighted imaging to diffusion tensor imaging and beyond," *Radiographics,* vol. 26, pp. S205-S223, 2006.

[66] C. Bougias and E. E. Tripoliti, "Theory of diffusion tensor imaging and fiber tractography analysis," *European Journal of Radiography,* vol. 1, pp. 37-41, 2009.

[67] M. Rosenbloom, E. V. Sullivan, and A. Pfefferbaum, "Using magnetic resonance imaging and diffusion tensor imaging to assess brain damage in alcoholics," *Alcohol Research and Health,* vol. 27, pp. 146-152, 2003.

[68] T. J. Whitford, M. Kubicki, and M. E. Shenton, "Diffusion tensor imaging, structural connectivity, and schizophrenia," *Schizophrenia research and treatment*, vol. 2011, 2011.

[69] P. Mukherjee, J. Berman, S. Chung, C. Hess, and R. Henry, "Diffusion tensor MR imaging and fiber tractography: theoretic underpinnings," *American journal of neuroradiology*, vol. 29, pp. 632-641, 2008.

[70] M. Maneshi, "Resting-state Functional Connectivity: Methods and Application in Epilepsy," McGill University, 2014.

[71] D. M. Cole, S. M. Smith, and C. F. Beckmann, "Advances and pitfalls in the analysis and interpretation of resting-state FMRI data," *Frontiers in systems neuroscience*, vol. 4, p. 8, 2010.

[72] D. Zhou, "Functional Connectivity Analysis of FMRI Time-Series Data," University of Pittsburgh, 2011.

[73] K. J. Friston, "Introduction: experimental design and statistical parametric mapping," *Human brain function*, 2004.

[74] V. D. Calhoun, J. Liu, and T. Adalı, "A review of group ICA for fMRI data and ICA for joint inference of imaging, genetic, and ERP data," *Neuroimage*, vol. 45, pp. S163-S172, 2009.

[75] D. Langlois, S. Chartier, and D. Gosselin, "An introduction to independent component analysis: InfoMax and FastICA algorithms," *Tutorials in Quantitative Methods for Psychology*, vol. 6, pp. 31-38, 2010.

[76] M. J. McKeown, L. K. Hansen, and T. J. Sejnowsk, "Independent component analysis of functional MRI: what is signal and what is noise?," *Current opinion in neurobiology*, vol. 13, pp. 620-629, 2003.

[77] V. D. Calhoun, T. Adali, G. D. Pearlson, and J. Pekar, "A method for making group inferences from functional MRI data using independent component analysis," *Human brain mapping*, vol. 14, pp. 140-151, 2001.

[78] E. B. Erhardt, S. Rachakonda, E. J. Bedrick, E. A. Allen, T. Adali, and V. D. Calhoun, "Comparison of multi-subject ICA methods for analysis of fMRI data," *Human brain mapping*, vol. 32, pp. 2075-2095, 2011.

[79] H. Wang and W. Zeng, "Fuzzy Cluster Method based on RV measure for functional MRI data analysis," in *Proceedings of the 2nd International Conference on Computer Science and Electronics Engineering*, 2013.

[80] Y. Wang and T.-Q. Li, "Analysis of whole-brain resting-state fMRI data using hierarchical clustering approach," *PLoS One*, vol. 8, p. e76315, 2013.

[81] K. J. F. a. C. Büchel, "Functional Connectivity: Eigenimages and multivariate analyses," *In: R. S. J Frackowiak, J. Ashburner, W. D. Penny, S. Zeki, K. J. Friston, C. Frith, R. Dolan, C. J. Price, Human Brain Function. San Diego: Academic Press*, 2003.

[82] A. Razi and K. J. Friston, "The connected brain: causality, models, and intrinsic dynamics," *IEEE Signal Processing Magazine*, vol. 33, pp. 14-35, 2016.

[83] K. R. Sreenivasan, "Connectivity analysis of functional MRI data in the latent neuronal space: Applications in science and medicine," 2014.

[84] P. Tarka, "An overview of structural equation modeling: its beginnings, historical development, usefulness and controversies in the social sciences," *Quality & quantity*, vol. 52, pp. 313-354, 2018.

[85] T. Kavallappa, S. Roys, A. Roy, J. Greenspan, R. Gullapalli, and A. McMillan, "Reliability of Structural Equation Modeling of the Motor Cortex in Resting State Functional MRI," in *26th Southern Biomedical Engineering Conference SBEC 2010, April 30-May 2, 2010, College Park, Maryland, USA*, 2010, pp. 481-484.

[86] X. Di and B. B. Biswal, "Identifying the default mode network structure using dynamic causal modeling on resting-state functional magnetic resonance imaging," *Neuroimage*, vol. 86, pp. 53-59, 2014.

[87] G. A. James, M. E. Kelley, R. C. Craddock, P. E. Holtzheimer, B. W. Dunlop, C. B. Nemeroff, *et al.*, "Exploratory structural equation modeling of resting-state fMRI: applicability of group models to individual subjects," *Neuroimage*, vol. 45, pp. 778-787, 2009.

[88] A. McIntosh, "Moving between functional and effective connectivity," *Analysis and function of large-scale brain networks*, p. 15, 2010.

[89] J. C. Rajapakse and J. Zhou, "Learning effective brain connectivity with dynamic Bayesian networks," *Neuroimage*, vol. 37, pp. 749-760, 2007.

[90] A. Roebroeck, E. Formisano, and R. Goebel, "Mapping directed influence over the brain using Granger causality and fMRI," *Neuroimage*, vol. 25, pp. 230-242, 2005.

[91] D. Goldenberg and A. Galván, "The use of functional and effective connectivity techniques to understand the developing brain," *Developmental cognitive neuroscience,* vol. 12, pp. 155-164, 2015.

[92] J. Ashburner, G. Barnes, C. Chen, J. Daunizeau, G. Flandin, K. Friston, *et al.*, "SPM12 manual," *Wellcome Trust Centre for Neuroimaging, London, UK,* 2014.

[93] A. Razi, J. Kahan, G. Rees, and K. J. Friston, "Construct validation of a DCM for resting state fMRI," *Neuroimage,* vol. 106, pp. 1-14, 2015.

[94] M. G. Sharaev, V. V. Zavyalova, V. L. Ushakov, S. I. Kartashov, and B. M. Velichkovsky, "Effective connectivity within the default mode network: dynamic causal modeling of resting-state fMRI data," *Frontiers in human neuroscience,* vol. 10, p. 14, 2016.

[95] L. Li, B. Li, Y. Bai, W. Liu, H. Wang, H. C. Leung, *et al.*, "Abnormal resting state effective connectivity within the default mode network in major depressive disorder: a spectral dynamic causal modeling study," *Brain and behavior,* vol. 7, p. e00732, 2017.

[96] J. D. Ramsey, S. J. Hanson, C. Hanson, Y. O. Halchenko, R. A. Poldrack, and C. Glymour, "Six problems for causal inference from fMRI," *neuroimage,* vol. 49, pp. 1545-1558, 2010.

[97] A. Łupińska-Dubicka, "Modeling dynamical systems by means of dynamic Bayesian networks," *Zeszyty Naukowe Politechniki Białostockiej. Informatyka,* pp. 77-92, 2012.

[98] H. Lähdesmäki and I. Shmulevich, "Learning the structure of dynamic Bayesian networks from time series and steady state measurements," *Machine Learning,* vol. 71, pp. 185-217, 2008.

[99] L. Zhang, M. Guindani, and M. Vannucci, "Bayesian models for functional magnetic resonance imaging data analysis," *Wiley Interdisciplinary Reviews: Computational Statistics,* vol. 7, pp. 21-41, 2015.

[100] J. F. Smith, A. S. Pillai, K. Chen, and B. Horwitz, "Effective connectivity modeling for fMRI: six issues and possible solutions using linear dynamic systems," *Frontiers in systems neuroscience,* vol. 5, p. 104, 2012.

[101] M. L. Seghier, P. Zeidman, N. H. Neufeld, A. P. Leff, and C. Price, "Identifying abnormal connectivity in patients using Dynamic Causal Modelling of fMRI responses," *Frontiers in systems neuroscience,* vol. 4, p. 142, 2010.

[102] J. F. Smith, K. Chen, A. S. Pillai, and B. Horwitz, "Identifying effective connectivity parameters in simulated fMRI: a direct comparison of switching linear dynamic system, stochastic dynamic causal, and multivariate autoregressive models," *Frontiers in neuroscience,* vol. 7, p. 70, 2013.

[103] J. X. O'reilly, M. W. Woolrich, T. E. Behrens, S. M. Smith, and H. Johansen-Berg, "Tools of the trade: psychophysiological interactions and functional connectivity," *Social cognitive and affective neuroscience,* vol. 7, pp. 604-609, 2012.

[104] J. Wang, X. Zuo, and Y. He, "Graph-based network analysis of resting-state functional MRI," *Frontiers in systems neuroscience,* vol. 4, p. 16, 2010.

[105] H. Onias, A. Viol, F. Palhano-Fontes, K. C. Andrade, M. Sturzbecher, G. Viswanathan, *et al.*, "Brain complex network analysis by means of resting state fMRI and graph analysis: Will it be helpful in clinical epilepsy?," *Epilepsy & Behavior,* vol. 38, pp. 71-80, 2014.

[106] F. Ferreira-Santos, "Complex network analysis of brain connectivity: An introduction," *University of Porto,* 2012.

[107] M. P. Van Den Heuvel and H. E. H. Pol, "Exploring the brain network: a review on resting-state fMRI functional connectivity," *European neuropsychopharmacology,* vol. 20, pp. 519-534, 2010.

[108] M. Schurz, H. Wimmer, F. Richlan, P. Ludersdorfer, J. Klackl, and M. Kronbichler, "Resting-state and task-based functional brain connectivity in developmental dyslexia," *Cerebral Cortex,* vol. 25, pp. 3502-3514, 2014.

Appendix

Table 7.1: The brain areas that showed activation in each control subject.

subject	component	maximum voxel	brain areas	z-score	spatial sorting using maxim voxel criteria
1	1	[15, -91, -10]	Right Cerebrum, Occipital Lobe, Inferior Occipital Gyrus, GM, BA 17	9,4760	24
	2	[24, -88, -16]	Right Cerebrum, Occipital Lobe, Fusiform Gyrus, WM	9,0859	8
	3	[51, -61, -16]	Right Cerebrum, Temporal Lobe, Fusiform Gyrus, GM, BA 37	14,5443	3
	4	[0, -61, 62]	Inter-Hemispheric	5,6401	19
	5	[6, 17, 2]	Right Cerebrum, Sub-lobar, Caudate, GM, GM, Caudate Head	9,5913	18
	6	[15, -91, -10]	Right Cerebrum, Occipital Lobe, Inferior Occipital Gyrus, GM, BA 17	11,4124	13
	7	[27, -88, -16]	Right Cerebrum, Occipital Lobe, Fusiform Gyrus, WM	10,7081	14
	8	[21, -91, -13]	Right Cerebrum, Occipital Lobe Fusiform Gyrus, WM	14,7544	21
	9	[45, -70, -19]	Right Cerebellum, Posterior Lobe, Declive, GM	7,1659	22
	10	[0, -10, 2]	Right Cerebrum, Sub-lobar, Third Ventricle, CSF	8,0295	6
	11	[33, 23, -22]	Right Cerebrum, Temporal Lobe, Superior Temporal Gyrus	8,9114	7
	12	[27, 44, 44]	Rigth Cerebrum, Frontal Lobe, Middle Frontal Gyrus	6,6038	5
	13	[0, -40, 5]	Inter-Hemispheric	14,4047	1
	14	[24, 35, 56]	Right Cerebrum, Frontal Lobe, Superior Frontal Gyrus, GM, BA 8	13,3764	16
	15	[12, 23, -1]	Right Cerebrum, Sub-lobar, Lateral Ventricle, CSF	8,0360	20
	16	[6, -94, 20]	Right Cerebrum, Occipital Lobe, Cuneus, GM, BA 18	9,4230	2
	17	[24, -91, -13]	Right Cerebrum, Occipital Lobe, Fusiform Gyrus, WM	5,6731	11
	18	[42, -70, -19]	Right Cerebellum, Posterior Lobe, Declive, GM	13,5454	15
	19	[21, -91, -13]	Right Cerebrum, Occipital Lobe, Fusiform Gyrus, WM	14,4608	10
	20	[-12, -1, 29]	Left Cerebrum, Limbic Lobe, Cingulate Gyrus, WM	9,3693	23
	21	[6, 14, 17]	Right Cerebrum, Sub-lobar, Lateral Ventricle, CSF	11,8349	9
	22	[-12, 32, 62]	Left Cerebrum, Frontal Lobe, Superior Frontal Gyrus, GM, BA 6	11,6978	12
	23	[6, 56, -1]	Right Cerebrum, Frontal Lobe, Superior Frontal Gyrus	7,3507	17

	24	[0 -10, 14]	Inter-Hemispheric	17,0271	4
2	1	[-9, -13, -19]	Left Brainstem, Pons	9,1826	7
	2	[33, -85, -25]	Right Cerebrum, Posterior Lobe, Uvula, GM	9,2931	11
	3	[15, -31, -46]	Left Brainstem, Pons	13,1553	3
	4	[-3, -67, 62]	Inter-Hemispheric	7,1411	16
	5	[21, -28, -31]	Left Brainstem, Pons	10,1552	22
	6	[-12, -34, -19]	Left Cerebellum, Anterior Lobe, Culmen, GM	8,6999	18
	7	[-9, -1, -22]	Left Cerebrum, Limbic Lobe, Uncus	19,9712	5
	8	[-27, -70, 53]	Left Cerebrum, Parietal Lobe, Precuneus, GM, BA 7	7,6453	9
	9	[39, 35, 38]	Right Cerebrum, Frontal Lobe, Middle Frontal Gyrus, GM, BA 8	9,7627	10
	10	[15, -28, -46]	Left Brainstem, Pons	9,6627	2
	11	[-9, -13, -22]	Left Brainstem, Pons	15,3003	1
	12	[-6, 44, 53]	Left Cerebrum, Frontal Lobe, Superior Frontal Gyrus, GM, BA 8	5,9738	19
	13	[0, -46, 11]	Inter-Hemispheric	8,7451	6
	14	[12, -28, -46]	Right Brainstem, Pons	7,0514	17
	15	[-36, 8, -16]	Left Cerebrum, Temporal Lobe, Superior Temporal Gyrus	7,3674	23
	16	[-12, 2, -16]	Left Cerebrum, Limbic Lobe	11,7087	13
	17	[0, -82, 14]	Inter-Hemispheric, Occipital Lobe, Cuneus	8,3202	20
	18	[39, -82, -13]	Right Cerebrum, Occipital Lobe, Inferior Occipital Gyrus, GM, BA 18	10,1900	8
	19	[-6, -22, 38]	Left Cerebrum, Limbic Lobe, Cingulate Gyrus	9,0360	15
	20	[0, -46, -28]	Right Cerebellum, Anterior Lobe, Nodule, GM	7,8973	24
	21	[0, -7, -1]	Right Cerebrum, Sub-lobar, Third Ventricle, CSF	6,1272	4
	22	[3, -43, 77]	Inter-Hemispheric	11,1879	14
	23	[15, -28, -43]	Right Brainstem, Pons	8,0756	12
	24	[0, -7, 11]	Inter-Hemispheric	7,1551	21
3	1	[0, -40, -16]	Left Brainstem, Midbrain	6,6010	9

	2	[21, -85, -16]	Right Cerebrum, Occipital Lobe, Fusiform Gyrus	6,3282	11
	3	[12, -91, -10]	Right Cerebrum, Occipital Lobe, Inferior Occipital Gyrus, GM, BA 17	6,5945	13
	4	[3, -76, 47]	Right Cerebrum, Posterior Lobe, Precuneus	6,8266	20
	5	[0, -46, -37]	Left Brainstem, Medulla	8,0276	16
	6	[0, -16, 2]	Right Cerebrum, Sub-lobar, Third Ventricle, CSF	6,4260	22
	7	[-9, -1, -19]	Left Cerebrum, Limbic Lobe, Uncus	9,4053	7
	8	[-42, 11, 44]	Left Cerebrum, Frontal Lobe, Middle Frontal Gyrus, WM	5,3044	14
	9	[0, -43, -25]	Left Cerebellum, Anterior Lobe, GM	13,8047	5
	10	[57, 11, 2]	Right Cerebrum, Temporal Lobe	6,3013	18
	11	[0, -13, -13]	Left Brainstem, Midbrain	13,6858	15
	12	[-42, -73, -19]	Left Cerebellum, Posterior Lobe, Declive, GM	6,3799	19
	13	[0, -46, 5]	Inter-Hemispheric	12,3271	4
	14	[-6, 44, 53]	Left Cerebrum, Frontal Lobe, Superior Frontal Gyrus, GM, BA 8	8,0512	24
	15	[0, 50, -4]	Inter-Hemispheric	7,4304	1
	16	[0, -46, -37]	Left Brainstem, Medulla	10,4295	3
	17	[6, -64, 14]	Right Cerebrum, LimbicLobe, Posterior Cingulate, WM	5,7312	6
	18	[0, -43, -25]	Left Cerebellum, Anterior Lobe, GM	7,9315	12
	19	[15, -25, -40]	Right Brainstem, Pons	6,9616	2
	20	[0, -40, -22]	Right Cerebellum, Sub-lobar, Fourth Ventricle, CSF	11,4022	10
	21	[-3, 2, 23]	Left Cerebrum, Sub-lobar, Extra-Nuclear, WM, Corpus Callosum	5,1144	23
	22	[0, -46, -28]	Right Cerebellum, Anterior Lobe, Nodule, GM	9,4262	17
	23	[-3, -55, 41]	Left Cerebrum, Parietal Lobe, Precuneus, GM, BA 7	6,1672	8
	24	[0, -16, 8]	inter-Hemispheric	6,7780	21
4	1	[-3, -73, 53]	Left Cerebrum, Parietal Lobe, Precuneus, GM, BA 7	6,8247	7
	2	[18, -25, -40]	Right Brainstem, Pons	15,0438	11
	3	[-12, -34, -43]	Left Brainstem, Pons	16,1048	3

	4	[-6, -67, 32]	Left Cerebrum, Occipital Lobe, Cuneus, WM	9,8201	2
	5	[0, -43, -37]	Left Brainstem, Medulla	10,1963	6
	6	[9, -91, -4]	Right Cerebrum, Occipital Lobe, Lingual Gyrus, WM	14,0847	13
	7	[-21, 14, -25]	Left Cerebrum, BA 38	19,1390	21
	8	[-45, 29, 32]	Left Cerebrum, Frontal Lobe, Middle Frontal Gyrus, WM	7,4406	15
	9	[42, 35, 35]	Right Cerebrum, Frontal Lobe, Middle Frontal Gyrus, WM	7,7381	4
	10	[33, 17, -22]	Right Cerebrum, Temporal Lobe, Superior Temporal Gyrus, GM BA 38	9,4191	5
	11	[-39, 14, -13]	Left Cerebrum, Frontal Lobe, Inferior Frontal Gyrus	17,9036	10
	12	[-42, 14, -16]	Left Cerebrum, Temporal Lobe, Superior Temporal Gyrus	6,6593	23
	13	[-12, -34, -43]	Left Brainstem, Pons	13,7083	24
	14	[-42, -16, 62]	Left Cerebrum, Frontal Lobe, Precentral Gyrus, GM, BA 6	7,7403	20
	15	[0, -43, -37]	Left Brainstem, Medulla	10,0485	14
	16	[42, 11, -1]	Right Cerebrum, Sub-lobar, Insula, WM	7,0168	9
	17	[-3, -88, 5]	Left Cerebrum, Occipital Lobe, Lingual Gyrus, GM, BA 17	7,3450	22
	18	[36, -70, -19]	Right Cerebellum, Posterior Lobe, Declive, GM	7,1130	8
	19	[9, -91, -1]	Right Cerebrum, Occipital Lobe, Lingual Gyrus, WM	7,3619	19
	20	[15, -19, -28]	Left Brainstem, Pons	7,8489	17
	21	[0, -46, -34]	Left Brainstem, Medulla	10,7870	18
	22	[-24, -28, 74]	Left Cerebrum, Parietal Lobe, Postcentral Gyrus, GM, BA 3	7,5659	16
	23	[0, -70, 41]	Inter-Hemispheric	9,3687	1
	24	[3, 5, 8]	Right Cerebrum, Sub-lobar, Lateral Ventricle, CSF	8,7340	12
5	1	[9, -97, 8]	Right Cerebrum, Occipital Lobe, Cuneus, WM	11,4505	11
	2	[30, -85, -19]	Right Cerebellum, Posterior Lobe, Declive, GM	16,3772	6
	3	[18, -28, -40]	Right Brainstem, Pons	8,9713	13
	4	[3, -67, 59]	Right Cerebrum, BA 7	8,0955	2
	5	[-15, -37, 14]	Left Cerebrum, Sub-lobar, Lateral Ventricle, CSF	8,6131	20

	6	[12, -94, 2]	Right Cerebrum, Occipital Lobe, Lingual Gyrus, GM, BA 17	19,9207	22
	7	[-12, -1, -19]	Left Cerebrum, Limbic Lobe, Parahippocampal Gyrus	9,9617	24
	8	[45, -73, -22]	Right Cerebellum, Posterior Lobe, Declive, GM	10,0963	10
	9	[6, 38, 56]	Right Cerebrum, Frontal Lobe, Superior Frontal Gyrus, GM, BA 8	6,7727	19
	10	[12, -31, -13]	Right Cerebellum, Anterior Lobe, Culmen, GM	11,5997	1
	11	[15, -28, -22]	Right Brainstem, Pons	27,0034	17
	12	[12, -94, -1]	Right Cerebrum, Occipital Lobe, Cuneus	9,1744	8
	13	[0, -49, 8]	inter-Hemispheric	19,4779	7
	14	[33, -37, 71]	Right Cerebrum, Parietal Lobe, Postecentral Gyrus	9,1795	18
	15	[18, -28, -22]	Right Brainstem, Pons	7,2226	21
	16	[18, 2, -13]	Right Cerebrum, Frontal Lobe, Subcallosar Gyrus	8,7838	14
	17	[6, -94, 14]	Right Cerebrum, Occipital Lobe, Cuneus, GM, BA 18	10,4588	12
	18	[45, -70, -19]	Right Cerebellum, Posterior Lobe, Declive, GM	9,9615	3
	19	[9, -94, 5]	Right Cerebrum, Occipital Lobe, Cuneus, GM, BA 17	11,5685	16
	20	[-6, -34, 77]	Left Cerebrum, Frontal Lobe, Paracentral Lobule, WM	12,8937	5
	21	[3, 8, 20]	Right Cerebrum, Sub-lobar, Extra-Nuclear, WM, Corpus Callosum	9,4312	4
	22	[-9, -34, 77]	Left Cerebrum, Frontal Lobe, Paracentral Lobule, WM	12,6223	15
	23	[-42, -76, 38]	Left Cerebrum, Parietal Lobe, Precuneus, GM, BA 19	6,8883	23
	24	[0, -7, 14]	Inter-Hemispheric	12,0446	9
6	1	[-24, 17, -25]	Left Cerebrum, Temporal Lobe, Superior Temporal Gyrus	7,2551	7
	2	[30, -85, -16]	Right Cerebellum, Posterior Lobe, Declive, GM	11,6114	13
	3	[-33, -13, 25]	Left Cerebrum, Sub-lobar, Extra-Nuclear, WM	11,0613	24
	4	[18, 68, 17]	Right Cerebrum, Frontal Lobe, Superior Frontal Gyrus, GM, BA 10	10,3015	21
	5	[-15, -37, 14]	Left Cerebrum, Sub-lobar, Lateral Ventricle, CSF	8,1332	2
	6	[-30, -7, 71]	Left Cerebrum, Frontal Lobe, Precentral Gyrus, GM, BA 6	7,7290	3
	7	[-12, -4, -19]	Left Cerebrum, Limbic Lobe, Parahippocampal Gyrus	26,1909	16

	8	[63, 17, 14]	Right Cerebrum, Frontal Lobe, Inferior Frontal Gyrus, GM, BA 44	7,2143	17
	9	[18, 35, 56]	Right Cerebrum, Frontal Lobe, Superior Frontal Gyrus	10,3108	18
	10	[24, 53, 38]	Right Cerebrum, Frontal Lobe, Superior Frontal Gyrus, GM, BA 9	8,1747	20
	11	[-30, 8, -28]	Left Cerebrum, Temporal Lobe, Sub-Gyral, WM	6,7219	9
	12	[18, 68, 17]	Right Cerebrum, Frontal Lobe, Superior Frontal Gyrus, GM, BA 10	7,7434	4
	13	[0, -46, 8]	Inter-Hemispheric	16,4463	14
	14	[15, 53, 47]	Right Cerebrum, Frontal Lobe, Superior Frontal Gyrus, GM, BA 8	9,4466	15
	15	[15, 65, 14]	Right Cerebrum, Frontal Lobe, Superior Frontal Gyrus, GM, BA 10	8,8994	19
	16	[18, 68, 14]	Right Cerebrum, Frontal Lobe, Superior Frontal Gyrus, GM, BA 10	10,8250	22
	17	[15, -28, -46]	Right Brainstem, Pons	10,6948	10
	18	[48, -55, -25]	Right Cerebellum, Posterior Lobe, Tuber, GM	10,5952	5
	19	[9, 65, 29]	Right Cerebrum, Frontal Lobe, Superior Frontal Gyrus, GM, BA 9	8,5660	12
	20	[12, 5, 26]	Right Cerebrum, LimbicLobe, Posterior Cingulate, WM	10,3915	6
	21	[-3, 14, 17]	Left Cerebrum, Sub-lobar, Extra-Nuclear, WM, Corpus Callosum	12,9219	23
	22	[-30, -4, 68]	Left Cerebrum, Frontal Lobe, Superior Frontal Gyrus	8,3035	1
	23	[12, 47, 53]	Right Cerebrum, Frontal Lobe, Superior Frontal Gyrus, GM, BA 8	7,5957	8
	24	[6, -4, 14]	Right Cerebrum, Sub-lobar, Lateral Ventricle, CSF	12,9711	11
group	1	[6, -94, 8]	Right Cerebrum, Occipital Lobe, Cuneus, WM	7,0656	7
	2	[30, -85, -19]	Right Cerebrum, Posterior Lobe, Declive, GM	12,9342	13
	3	[15, -28, -43]	Right Brainstem, Pons	10,6579	11
	4	[0, -67, 59]	Inter-Hemispheric	8,4151	24
	5	[-15, -37, 14]	Left Cerebrum, Sub-lobar, Lateral Ventricle, CSF	8,5388	2
	6	[9, -94, -1]	Right Cerebrum, Occipital Lobe, Lingual Gyrus, GM, BA 17	12,8032	6
	7	[-12, -1, -19]	Left Cerebrum, Limbic Lobe, Parahippocampal Gyrus	19, 8024	21
	8	[-45, 32, 32]	Left Cerebrum, Frontal Lobe, Middle Frontal Gyrus, GM, BA 9	6,0457	18
	9	[39, 35, 38]	Right Cerebrum, Frontal Lobe, Middle Frontal Gyrus, GM, BA 8	6,7031	3

	10	[0, -13, 2]	Right Cerebrum, Sub-lobar, Third Ventricle, CSF	9,0958	16
	11	[18, -28, -22]	Right Brainstem, Pons	16,0519	20
	12	[-42, 14, -16]	Left Cerebrum, Temporal Lobe, Superior Temporal Gyrus	5,4788	22
	13	[0, -43, 5]	Inter-Hemispheric	18,5596	14
	14	[24, 35, 56]	Right Cerebrum, Frontal Lobe, Superior Frontal Gyrus, GM, BA 6	9,1053	10
	15	[0, 50, -4]	Inter-Hemispheric	8,8042	15
	16	[-9, 2, -16]	Left Cerebrum	9,7818	5
	17	[3, -79, 14]	Right Cerebrum, Occipital Lobe, Cuneus, GM, BA 18	6,3961	4
	18	[42, -70, -19]	Right Cerebellum, Posterior Lobe, Declive, GM	11,7584	19
	19	[21, -91, -13]	Right Cerebrum, Occipital Lobe, Fusiform Gyrus, WM	7,5550	23
	20	[12, 2, 26]	Right Cerebrum, Limbic Lobe, Cingulate Gyrus, WM	9,4110	1
	21	[0, 5, 20]	inter-Hemispheric, WM, Corpus Callosum	12,7074	9
	22	[-21, -37, 77]	Left Cerebrum, Parietal Lobe, Postcentral Gyrus, WM	9,3764	17
	23	[0, -58, 32]	Left Cerebrum, Parietal Lobe, Precuneus	7,3192	8
	24	[0. -7, 14]	Inter-Hemispheric	14,2915	12

Table 7.2: The brain areas that showed activation in each RLS subject.

subject	component	maximum voxel	Brain areas	z-score	spatial sorting using maxim voxel criteria
1	1	[-3, -94, 11]	Left Cerebrum, Occipital Lobe, Cuneus, GM, BA 18	7,4208	12
	2	[0, -85, -19]	Right Cerebellum, GM	8,0339	23
	3	[33, 14, -19]	Right Cerebrum, Temporal Lobe, Superior Temporal Gyrus	9,0451	9
	4	[-3, -94, 11]	Left Cerebrum, Occipital Lobe, Cuneus, GM, BA 18	8,8319	14
	5	[0, -88, -13]	Inter-Hemispheric	6,5886	25
	6	[-15, -88, -19]	Left Cerebellum, Posterior Lobe, Declive, GM	7,306	3
	7	[-27, -88, -19]	Left Cerebellum, Posterior Lobe, Declive, GM	6,6735	4
	8	[33, 11, -28]	Right Cerebrum, Temporal Lobe, Superior Temporal Gyrus, WM	7,6464	18
	9	[12, -13, -25]	Right Brainstem, Pons	10,4789	21

	10	[0, -85, -19]	Right Cerebellum, GM	6,4978	16
	11	[-21, -28, -28]	Left Brainstem, Pons	7,1139	19
	12	[0, -46, 8]	Inter-Hemispheric	19,0215	22
	13	[0, -7, 11]	Inter-Hemispheric	7,4167	15
	14	[-15, 2, -19]	Left Cerebrum, Limbic Lobe, Uncus	9,7306	8
	15	[-12, 59, 35]	Left Cerebrum, Frontal Lobe, Superior Frontal Gyrus, GM, BA 9	7,6906	1
	16	[0, -46, 8]	Inter-Hemispheric	8,14	13
	17	[9, 8, 23]	Right Cerebrum, Frontal Lobe, Sub-Gyral, WM, Corpus Callosum	6,8012	6
	18	[-15, -25, -31]	Left Brainstem, Pons	8,7709	2
	19	[0, -28, 11]	Inter-Hemispheric, WM, Corpus, Callosum	8,0101	11
	20	[6, -73, 14]	Right Cerebrum, Occipital Lobe, Cuneus, WM	6,6708	24
	21	[-27, -88, -19]	Left Cerebellum, Posterior Lobe, Declive, GM	8,2012	17
	22	[0, -49, 29]	Left Cerebrum, Limbic Lobe, Cingulate Gyrus	7,9471	7
	23	[6, -7, -22]	Right Brainstem, Pons	15,7693	20
	24	[0, -70, 59]	Inter-Hemispheric	7,4211	5
	25	[0, -46, 8]	Inter-Hemispheric	9,3194	10
2	1	[-15, -37, -19]	Left Cerebellum, Anterior Lobe, Culmen, GM	8,0408	3
	2	[6, -49, -19]	Right Cerebellum, Anterior Lobe, Fastigium, GM	5,3325	11
	3	[-15, -34, -22]	Left Cerebellum, Anterior Lobe, Culmen, GM	11,804	23
	4	[51, 14, 32]	Right Cerebrum, Frontal Lobe, Middle Frontal Gyrus, WM	6,0403	16
	5	[42, -55, -25]	Right Cerebellum, Posterior Lobe, Tuber, GM	5,9787	8
	6	[51, 14, -10]	Right Cerebrum, Temporal Lobe, Superior Temporal Gyrus, GM, BA 38	7,2238	18
	7	[-39, -70, -19]	Left Cerebellum, Posterior Lobe, Declive, GM	7,707	19
	8	[6, -40, -34]	Right Brainstem, Pons	8,472	15
	9	[18, -10, -22]	Right Cerebrum, Limbic Lobe, Parahippocampal Gyrus, GM, BA 28	7,5012	1
	10	[-48, 17, 41]	Left Cerebrum, Frontal Lobe, Middle Frontal Gyrus, GM, BA 8	5,6253	12

	11	[36, 11, -19]	Right Cerebrum, Temporal Lobe, Superior Temporal Gyrus, GM, BA 38	9,8325	7
	12	[0, -46, 11]	Inter-Hemispheric	8,0496	13
	13	[9, -13, 20]	Right Cerebrum, Sub-lobar, Lateral Ventricle, CSF	7,6552	17
	14	[57, 17, -4]	Right Cerebrum, Temporal Lobe, Inferior Temporal Gyrus	7,1668	9
	15	[18, 59, 26]	Right Cerebrum, Frontal Lobe, Superior Frontal Gyrus	8,1015	6
	16	[51, 5, -10]	Right Cerebrum, Temporal Lobe, Superior Temporal Gyrus, WM	8,8013	14
	17	[12, -4, 26]	Right Cerebrum, Limbic Lobe, Cingulate Gyrus, WM	7,5157	24
	18	[-39, -79, -25]	Left Cerebellum, Posterior Lobe, Tuber, GM	8,3828	4
	19	[54, 8, -16]	Right Cerebrum, Temporal Lobe, Middle Temporal Gyrus, GM, BA 21	8,2985	5
	20	[3, -76, 47]	Right Cerebrum, Parietal Lobe, Precuneus	5,1556	21
	21	[57, 23, 29]	Right Cerebrum, Frontal Lobe, Middle Frontal Gyrus, GM, BA 9	5,6402	10
	22	[48, 20, 41]	Right Cerebrum, Frontal Lobe, Middle Frontal Gyrus, GM, BA 8	5,4198	22
	23	[-3, -4, -22]	Left Brainstem, Pons	9,6512	2
	24	[18, -67, 65]	Right Cerebrum, Parietal Lobe, Superior Parietal Lobule, GM, BA 7	6,7246	20
	25	[-30, -28, 71]	Left Cerebrum, Parietal Lobe, Postcentral Gyrus	4,5374	25
3	1	[-18, -31, -28]	Left Brainstem, Pons	12,9532	8
	2	[3, -49, -28]	Right Cerebellum, Anterior Lobe, Nodule, GM	6,9002	23
	3	[-18, -31, -25]	Left Brainstem, Pons	13,8937	17
	4	[-12, -31, -22]	Left Brainstem, Pons	6,8016	3
	5	[-39, -34, 68]	Left Cerebrum, Parietal Lobe, POstcentral Gyrus, WM	6,4248	19
	6	[-9, 59, 38]	Left Cerebrum, Frontal Lobe	6,6023	1
	7	[-30, -82, -13]	Left Cerebrum, Occipital Lobe, Fusiform Gyrus, GM, BA 19	6,1963	11
	8	[0, -46, -28]	Right Cerebellum, Anterior Lobe, Nodule, GM	24, 609	16
	9	[0, -52, 14]	Inter-Hemispheric, Limbic Lobe, Posterior Cingulate	10,7383	14
	10	[-21, 41, 50]	Left Cerebrum, Frontal Lobe, Superior Frontal Gyrus, GM, BA 8	7,1774	12
	11	[-21, -31, -25]	Left Cerebellum, Anterior Lobe, GM	12,7552	18

	12	[0, -46, 5]	Inter-Hemispheric	12,4525	25
	13	[-3, 5, 8]	Left Cerebrum, Sub-lobar, Lateral Ventricle, CSF	11,4843	9
	14	[-15, -31, -28]	Left Brainstem, Pons	11,6705	13
	15	[0, 44, 50]	Inter-Hemisheric	6,5891	22
	16	[-18, -28, -28]	Left Brainstem, Pons	12,7315	20
	17	[-6, -4, 23]	Left Cerebrum, Sub-lobar, Extra-Nuclear, WM, Corpus Callosum	14,8134	10
	18	[-18, -31, -25]	Left Brainstem, Pons	11,2961	24
	19	[-21, -31, -28]	Left Brainstem, Pons	13,0678	2
	20	[18, -58, 5]	Right Cerebrum, Occipital Lobe, Lingual Gyrus, WM	7,6618	4
	21	[-18, -31, -22]	Left Cerebellum, Anterior Lobe, Culmen, GM	5,9018	6
	22	[0, -49, 23]	Left Cerebrum, Limbic Lobe, Posterior Cingulate	8,8388	15
	23	[-9, -1, -19]	Left Cerebrum, Limbic Lobe, Uncus	16,2426	5
	24	[3, -76, 47]	Right Cerebrum, Parietal Lobe, Precuneus	7,0446	7
	25	[0, -4, -4]	Right Cerebrum, Sub-lobar, Third Ventricle, CSF	11,1887	21
4	1	[-33, -73, -10]	Right Cerebrum, Occipital Lobe, Lingual Gyrus, WM	12,5576	23
	2	[0, -85, -1]	Left Cerebrum, Occipital Lobe	6,9851	18
	3	[-36, 14, -16]	Left Cerebrum, Frontal Lobe, Inferior Frontal Gyrus	14,1204	14
	4	[-12, 59, 35]	Left Cerebrum, Frontal Lobe, Superior Frontal Gyrus, GM, BA 9	5,5181	3
	5	[42, -58, 59]	Right Cerebrum, Parietal Lobe, Superior Parietal Lobule, GM, BA 7	8,0121	11
	6	[36, 14, -25]	Right Cerebrum, Temporal Lobe, Superior Temporal Gyrus, WM	8,0374	1
	7	[12, -94, 2]	Right Cerebrum, Occipital Lobe, Lingual Gyrus, GM, BA 17	8,1154	13
	8	[36, 14, -25]	Right Cerebrum, Temporal Lobe, Superior Temporal Gyrus, WM	7,6918	12
	9	[33, -7, -34]	Right Cerebrum, Limbic Lobe, Uncus, GM, BA 20	7,7668	19
	10	[-36, 47, 32]	Left Cerebrum, Frontal Lobe, Superior Frontal Gyrus, GM, BA 9	5,7065	20
	11	[36, 14, -19]	Right Cerebrum, Temporal Lobe, Superior Temporal Gyrus, GM, BA 38	12,844	21
	12	[-6, -40, -1]	Left Cerebrum, Limbic Lobe, Parahippocampal Gyrus	9,6929	7

	13	[0, -16, 17]	Inter-Hemispheric	10,5441	5
	14	[-15, 5, -19]	Left Cerebrum, Frontal Lobe	14,936	9
	15	[-12, -4, -19]	Left Cerebrum, Limbic Lobe, Parahippocampal Gyrus	6,026	6
	16	[39, 14, -25]	Right Cerebrum, Temporal Lobe, Superior Temporal Gyrus, WM	7,2826	17
	17	[-3, 8, 17]	Left Cerebrum, Sub-lobar, Lateral Ventricle, CSF	7,598	16
	18	[-33, -73, -13]	Left Cerebrum, Occipital Lobe, Fusiform Gyrus, GM, BA 19	17,9655	8
	19	[0, -52, 20]	Left Cerebrum, Limbic Lobe, Posterior Cingulate	9,3382	22
	20	[21, -67, 11]	Left Cerebrum, Occipital Lobe, Cuneus	9,2021	2
	21	[39, -61, 56]	Right Cerebrum, Parietal Lobe, Superior Parietal Lobule, GM, BA 7	9,1682	24
	22	[0, -58, 20]	Left Cerebrum, Occipital Lobe, Precuneus	7,128	15
	23	[0, -13, -19]	Right Brainstem, Pons	21,2398	25
	24	[39, 14, -25]	Right Cerebrum, Temporal Lobe, Superior Temporal Gyrus, WM	6,4369	10
	25	[3, 23, 59]	Inter-Hemispheric	5,8885	4
5	1	[0, -40, -13]	Left Cerebellum, Anterior Lobe, Cerebellar Lingual, GM	7,6581	3
	2	[0, -22, -7]	Left Brainstem, Midbrain	7,9256	23
	3	[33, 17, -22]	Right Cerebrum, Temporal Lobe, Superior Temporal Gyrus, GM, BA 38	18, 0289	12
	4	[27, 11, -22]	Right Cerebrum, Temporal Lobe, Superior Temporal Gyrus, GM, BA 38	5,6325	6
	5	[-24, -61, 68]	Left Cerebrum, Parietal Lobe, Superior Parietal Lobule, WM	7,7684	19
	6	[0, -22, -4]	Left Brainstem, Midbrain	11,9947	24
	7	[9, -1, -22]	Right Cerebrum, Limbic Lobe, Uncus	7,5985	11
	8	[-6, -37, -34]	Left Brainstem, Pons	5,3943	14
	9	[30, 11, -22]	Right Cerebrum, Temporal Lobe, Superior Temporal Gyrus	8,6629	9
	10	[-30, -40, -37]	Left Cerebellum, Posterior Lobe, Cerebellar Tonsil, GM	5,369	13
	11	[0, -22, -4]	Left Brainstem, Midbrain	11,367	16
	12	[0, -43, 5]	Inter-Hemispheric	14,083	2
	13	[0, -22, -4]	Left Brainstem, Midbrain	8,654	22

	14	[0, -13, 2]	Right Cerebrum, Sub-lobar, Third Ventricle, CSF	10,6803	5
	15	[42, -4, 5]	Right Cerebrum, Sub-lobar, Insula, GM, BA 13	5,2376	1
	16	[33, 11, -22]	Right Cerebrum, Temporal Lobe, Superior Temporal Gyrus	8,0137	7
	17	[-6, 5, 23]	Left Cerebrum, Sub-lobar, Extra-Nuclear, WM, Corpus Callosum	6,3506	25
	18	[-3, -85, -16]	Left Cerebellum, GM	5,6954	20
	19	[0, -22, -4]	Left Brainstem, Midbrain	11,8686	17
	20	[30, 11, -19]	Right Cerebrum, Temporal Lobe, Superior Temporal Gyrus	6,7822	21
	21	[39, 50, -1]	Right Cerebrum, Frontal Lobe, Middle Frontal Gyrus, WM	5,9926	18
	22	[0, -16, -1]	Right Cerebrum, Sub-lobar, Third Ventricle, CSF	7,8679	4
	23	[3, -10, -22]	Right Brainstem, Pons	17,0691	8
	24	[0, -64, 62]	Inter-Hemispheric	11,5826	10
	25	[0, -13, -4]	Right Cerebrum, Sub-lobar, Third Ventricle, CSF	7,2733	15
6	1	[0, -37, -13]	Left Brainstem, Midbrain	17,1564	8
	2	[12, -85, -16]	Right Occipital Lobe, Libgual Lobe, GM, BA 18	15,3035	23
	3	[42, 8, -13]	Right Cerebrum, Temporal Lobe, Superior Temporal Gyrus, GM, BA 38	14,6842	18
	4	[0, -40, -22]	Right Cerebellum, Sub-lobar, Fourth Ventricle, CSF	9,7846	19
	5	[39, -79, -25]	Right Cerebellum, Posterior Lobe, Tuber, GM	10,1748	1
	6	[6, -94, 5]	Right Cerebrum, Occipital Lobe, Cuneus, WM	7,4142	11
	7	[27, -82, 35]	Right Cerebrum, Occipital Lobe, Cuneus, GM, BA 19	10,6307	2
	8	[0, -46, -31]	Left Brainstem, Pons	32,6353	3
	9	[-15, -25, -31]	Left Brainstem, Pons	9,3974	13
	10	[6, -82, -22]	Right Cerebellum, Posterior Lobe, Declive, GM	7,8708	14
	11	[-18, -25, -25]	Left Brainstem, Pons	15,6637	17
	12	[3, -43, 2]	Inter-Hemispheric	9,0007	7
	13	[12, -88, -16]	Right Cerebrum, Occipital Lobe, Lingual Gyrus, GM, BA 18	14,2859	5
	14	[-18, -31, -25]	Left Brainstem, Pons	12,9469	25

	15	[-18, -31, -25]	Left Brainstem, Pons	5,6143	4
	16	[-18, -31, -25]	Left Brainstem, Pons	8,9818	9
	17	[0, -85, -16]	Right Cerebellum, GM	12,4736	12
	18	[3, -85, -16]	Right Cerebellum, GM	20,3015	16
	19	[39, -79, -25]	Right Cerebellum, Posterior Lobe, Tuber, GM	17,1672	22
	20	[0, -82, 17]	Inter-Hemispheric, Occipital Lobe, Cuneus	8,6246	20
	21	[0, -88, -13]	Inter-Hemispheric	7,841	24
	22	[3, -85, -22]	Right Cerebellum, GM	8,9521	10
	23	[0, -10, -22]	Left Brainstem, Pons	24,4373	21
	24	[12, -91, -13]	Right Cerebrum, Occipital Lobe, Lingual Gyrus, WM	8,1837	6
	25	[0, -4, -1]	Right Cerebrum, Sub-lobar, Third Ventricle, CSF	9,795	15
7	1	[0, -40, -16]	Left Brainstem, Midbrain	12,8208	12
	2	[18, -28, -22]	Right Brainstem, Pons	9,2658	8
	3	[18, -28, -22]	Right Brainstem, Pons	13,6975	11
	4	[0, -43, 8]	Inter-Hemispheric	8,375	23
	5	[21, -28, -28]	Right Brainstem, Pons	9,3364	3
	6	[45, -7, -7]	Right Cerebrum, Temporal Lobe, Sub-Gyral, WM	6,5733	13
	7	[-33, -88, -16]	Left Cerebrum, Occipital Lobe, Fusiform Gyrus	10,0794	14
	8	[0, -46, -31]	Right Cerebellum, Anterior Lobe, Nodule, GM	28,5093	1
	9	[-15, -19, -25]	Left Brainstem, Pons	11,7685	9
	10	[-48, 20, -4]	Left Cerebrum, Frontal Lobe, Inferior Frontal Gyrus, WM	7,3065	19
	11	[-21, -28, -28]	Left Brainstem, Pons	18,0035	7
	12	[0, -43, 5]	Inter-Hemispheric	28,8548	5
	13	[0, -19, 5]	Inter-Hemispheric, CSF, Optic Tract	12,9913	24
	14	[-24, 5, -16]	Left Cerebrum, Limbic Lobe, Parahippocanpal Gyrus, GM, BA 34	12,9406	2
	15	[0, 2, 2]	Inter-Hemispheric	6,9129	18

	16	[0, -43, -25]	Left Cerebellum, Anterior Lobe, GM	8,4071	25
	17	[-6, -7, 26]	Left Cerebrum, Limbic Lobe, Cingulate Gyrus	6,9283	16
	18	[18, -28, -28]	Right Brainstem, Pons	8,8935	4
	19	[0, -25, 2]	Left Brainstem, Midbrain	11,8683	20
	20	[-21, -34, -31]	Left Brainstem, Pons	7,6238	10
	21	[-33, -88, -16]	Left Cerebellum, Posterior Lobe, Declive, GM	6,2756	17
	22	[0, -52, 23]	Inter-Hemispheric	6,8143	15
	23	[-9, -4, -22]	Left Cerebrum, Limbic Lobe, Uncus	17,6074	22
	24	[0, -70, 56]	Inter-Hemispheric	9,2945	6
	25	[-12, -28, -34]	Left Brainstem, Pons	8,4963	21
8	1	[0, -40, -13]	Left Cerebellum, Anterior Lobe, Cerebellar Lingual, GM	14,8449	8
	2	[12, -88, -16]	Right Cerebellum, Posterior Lobe, Uvuvla, GM	13,4321	18
	3	[12, -91, -13]	Right Cerebrum, Occipital Lobe, Lingual Gyrus, WM	9,8392	14
	4	[0, -43, -25]	Left Cerebellum, Anterior Lobe, GM	8,0724	13
	5	[-36, -82, -22]	Left Cerebellum, Posterior Lobe, Declive, GM	12,2664	23
	6	[-15, -88, -22]	Left Cerebellum, Posterior Lobe, Declive, GM	12,8836	1
	7	[-27, -88, -22]	Left Cerebellum, Posterior Lobe, Declive, GM	14,0449	22
	8	[0, -46, -28]	Right Cerebellum, Anterior Lobe, Nodule, GM	24,5202	7
	9	[30, -88, -16]	Right Cerebrum, Occipital Lobe, Fusiform Gyrus, GM, BA 18	8,6918	2
	10	[-33, -73, 47]	Left Ceerebrum, Parietal Lobe, Superior Parietal Lobule, GM, BA 7	6,8143	11
	11	[3, -85, -19]	Right Cerebellum, GM	13,0016	6
	12	[0, -43, 5]	Inter-Hemispheric	10,5552	5
	13	[-15, -88, -22]	Left Cerebellum, Posterior Lobe, Declive, GM	15,5973	20
	14	[-21, -1, -16]	Left Cerebrum, Limbic Lobe, Parahippocanpal Gyrus, GM, Amygdala	15,6947	12
	15	[-9, 38, 53]	Left Cerebrum, Frontal Lobe, Superior Frontal Gyrus, GM, BA 8	6,3004	3
	16	[0, -43, -25]	Left Cerebellum, Anterior Lobe, Culmen, GM	8,8862	21

	17	[-27, -88, -22]	Left Cerebellum, Posterior Lobe, Declive, GM	7,8452	19
	18	[-27, -88, -22]	Left Cerebellum, Posterior Lobe, Declive, GM	22,6638	16
	19	[0, -28, -1]	Left Brainstem, Midbrain	9,1177	24
	20	[0, -85, -16]	Right Cerebellum, GM	11,8091	9
	21	[27, -76, 50]	Right Cerebrum, Parietal Lobe, Precuneus, GM, BA 7	9,3057	4
	22	[-15, -88, -22]	Left Cerebellum, Posterior Lobe, Declive, GM	14,1548	25
	23	[-27, -88, -22]	Left Cerebellum, Posterior Lobe, Declive, GM	15,2753	17
	24	[-3, -64, 62]	Left Cerbrum, Parietal Lobe, Precuneus	8,7199	10
	25	[-30, -37, 68]	Left Cerebrum, Parietal Lobe, Postcentral Gyrus	8,0227	15
9	1	[-12, -28, -34]	Left Brainstem, Pons	10,2907	23
	2	[33, -85, -16]	Right Cerebellum, Posterior Lobe, Declive, GM	7,0709	3
	3	[-39, 14, -13]	Left Cerebrum, Frontal Lobe, Inferior Frontal Gyrus	14,1156	7
	4	[18, 59, 26]	Right Cerebrum, Frontal Lobe, Superior Frontal Gyrus	5,0435	11
	5	[-48, -46, 59]	Left Cerebrum, Parietal Lobe, Inferior Parietal Lobule, GM,BA 40	7,6112	12
	6	[6, -7, -22]	Right Brainstem, Pons	9,2857	14
	7	[-27, -88, -13]	Left Cerebrum, Occipital Lobe,Inferior Occipital Gyrus, GM, BA 18	14,0535	1
	8	[-15, -97, -10]	Left Cerebrum, Occipital Lobe, Lingual Gyrus, WM	7,6782	19
	9	[-30, 8, -19]	Left Cerebrum, Temporal Lobe, Superior Temporal Gyrus	6,1966	17
	10	[-3, 35, 53]	Inter-Hemispheric	5,251	6
	11	[33, 14, -19]	Right Cerebrum, Temporal Lobe, Superior Temporal Gyrus	13,8916	15
	12	[0, -43, 5]	Inter-Hemispheric	13,6652	8
	13	[3, -85, -4]	Right Cerebrum, Occipital Lobe, Lingual Gyrus, GM, BA 18	6,7431	5
	14	[-18, 5, -19]	Left Cerebrum, Limbic Lobe, Uncus, GM, BA 34	12,9905	2
	15	[-18, 59, 29]	Left Cerebrum, Frontal Lobe, Superior Frontal Gyrus	7,7025	16
	16	[-12, -28, -34]	Left Brainstem, Pons	7,0525	13
	17	[-6, -1, 23]	Left Cerebrum, Sub-lobar, Extra-Nuclear, WM, Corpus Callosum	9,3753	25

	18	[-45, -67, -25]	Left Cerebellum, Posterior Lobe, Tuber, GM	5,6584	20
	19	[12, -16, -19]	Right Brainstem, Pons	10,1916	9
	20	[0, -7, -13]	Left Brainstem, Midbrain	6,2031	24
	21	[-15, -97, -10]	Left Cerebrum, Occipital Lobe, Lingual Gyrus, WM	5,645	18
	22	[3, -64, 44]	Right Cerebrum, Parietal Lobe, Precuneus, GM, BA 7	5,6271	21
	23	[0, -10, -19]	Right Brainstem, Pons	22,7264	22
	24	[-39, -49, 65]	Left Cerebrum, Parietal Lobe, inferior Parietal Lobule, WM	5,7775	10
	25	[27, -43, 74]	Right Cerebrum, Parietal Lobe, Postcentral Gyrus, GM, BA 5	6,7041	4
10	1	[-12, 32, 56]	Left Cerebrum, Frontal Lobe, Superior Frontal Gyrus, GM, BA 6	8,0065	8
	2	[6, -91, 14]	Right Cerebrum, Occipital Lobe, Cuneus, WM	5,9329	15
	3	[63, 11, 17]	Right Cerebrum, Frontal Lobe, Inferior Frontal Gyrus	5,3858	23
	4	[-33, -64, -34]	Left Cerebellum, Posterior Lobe, Cerebellar Tonsil, GM	8,9226	12
	5	[21, -61, 71]	Right Cerebrum, Parietal Lobe, Superior Parietal Lobule, GM, BA 7	8,3466	7
	6	[-30, -64, -34]	Left Cerebellum, Posterior Lobe, Cerebellar Tonsil, GM	7,9543	4
	7	[-33, -64, -34]	Left Cerebellum, Posterior Lobe, Cerebellar Tonsil, GM	8,9326	5
	8	[-33, -64, -34]	Left Cerebellum, Posterior Lobe, Cerebellar Tonsil, GM	16,4299	1
	9	[-21, -1, -25]	Left Cerebrum, Limbic Lobe, Uncus, WM	5,7012	17
	10	[-15, 47, 50]	Left Cerebrum, Frontal Lobe, Superior Frontal Gyrus, GM, BA8	6,2609	13
	11	[-9, 14, 17]	Left Cerebrum, Sub-Lobar, Lateral Ventricle, CSF	5,7532	6
	12	[0, -43, 5]	Inter-Hemispheric	9,2717	18
	13	[-3, 41, 20]	Left Cerebrum, Frontal Lobe, Medial Frontal Gyrus	7,9662	14
	14	[9, 2, -13]	Right Cerebrum, Frontal Lobe, Subcallosal Gyrus	7,3227	22
	15	[-3, 44, 50]	Left Cerebrum, Frontal Lobe, Superior Frontal Gyrus, GM, BA 8	9,6009	21
	16	[-3, 47, 47]	Left Cerebrum, Frontal Lobe	6,4654	24
	17	[3, 8, 17]	Right Cerebrum, Sub-lobar, Lateral Ventricle, CSF	8,0059	16
	18	[-33, -64, -34]	Left Cerebellum, Posterior Lobe, Cerebellar Tonsil, GM	7,6754	10

	19	[3, -31, 5]	Right Cerebrum, Sub-lobar, Lateral Ventricle, CSF	7,062	19
	20	[-3, 44, 44]	Left Cerebrum, Frontal Lobe, Superior Frontal Gyrus, GM, BA 8	6,0114	25
	21	[-3, 44, 47]	Left Cerebrum, Frontal Lobe, Superior Frontal Gyrus, GM, BA 8	7,2246	20
	22	[18, -91, -16]	Right Cerebellum, Posterior Lobe, Declive, GM	7,3069	2
	23	[-6, -7, -22]	Left Brainstem, Pons	9,4522	11
	24	[18, -91, -16]	Right Cerebellum, Posterior Lobe, Declive, GM	7,2082	9
	25	[0, 47, 47]	Inter-Hemispheric	6,1527	3
11	1	[12, -91, -4]	Right Cerebrum, Occipital Lobe, Lingual Gyrus, WM	10,2171	23
	2	[15, -88, -19]	Right Cerebellum, Posterior Lobe, Declive, GM	13,7369	8
	3	[-36, 14, -16]	Left Cerebrum, Frontal Lobe, Inferior Frontal Gyrus	8,6798	12
	4	[9, -94, 5]	Right Cerebrum, Occipital Lobe, Cuneus, GM, BA 17	10,3102	13
	5	[9, -94, 5]	Right Cerebrum, Occipital Lobe, Cuneus, GM, BA 17	11,657	17
	6	[-54, 20, -1]	Left Cerebrum, Frontal Lobe, Inferior Frontal Gyrus, GM, BA 47	6,8525	9
	7	[42, -46, -16]	Right Cerebrum, Temporal Lobe, Fusiform, Gyrus, WM	8,6293	2
	8	[0, -43, -25]	Left Cerebellum, Anterior Lobe, GM	22,0848	18
	9	[9, -94, 8]	Right Cerebrum, Occipital Lobe, Cuneus, WM	14,5252	21
	10	[-33, -70, 53]	Left Cerebrum, Parietal Lobe, Superior Parietal Lobule, GM, BA 7	9,8313	5
	11	[0, -19, 5]	Inter-Hemispheric, CSF, Optic Tract	9,7126	24
	12	[-3, -40, 2]	Inter-Hemispheric	24,4186	20
	13	[9, -94, 5]	Right Cerebrum, Occipital Lobe, Cuneus, GM, BA 17	20,1843	4
	14	[-12, -4, -16]	Left Cerebrum, LimbicLobe, Parahippocampal Gyrus	8,2321	1
	15	[-3, 56, 35]	Left Cerebrum, Frontal Lobe, Medial Frontal Gyrus	7,1921	10
	16	[33, -82, -25]	Right Cerebellum, Posterior Lobe, Uvuvla, GM	7,8031	11
	17	[9, -94, 5]	Right Cerebrum, Occipital Lobe, Cuneus, GM, BA 17	15,4128	22
	18	[15, -85, -19]	Right Cerebellum, Posterior Lobe, Declive, GM	13,525	3
	19	[15, -88, -16]	Right Cerebellum, Posterior Lobe, Declive, GM	8,3222	7

	20	[-3, -88, 29]	Right Cerebrum, Occipital Lobe, Cuneus, GM, BA 19	10,5871	19
	21	[9, -94, 8]	Right Cerebrum, Occipital Lobe, Cuneus, WM	12,5754	14
	22	[3, -55, 14]	Right Cerebrum, Limbic Lobe, Posterior Cingulate, GM, BA 23	8,8464	16
	23	[0, -4, -22]	Left Braintsem, Pons	25,2282	15
	24	[0, -61, 62]	Inter-Hemispheric	11,4983	6
	25	[0, -22, 50]	Left Cerebrum, Frontal Lobe, Medial Frontal Gyrus	5,4296	25
12	1	[0, -40, -16]	Left Brainstem, Midbrain	31,6729	8
	2	[0, -13, -4]	Right Cerebrum, Sub-lobar, Third Ventricle, CSF	7,6692	1
	3	[-21, -31, -31]	Left Brainstem, Pons	18,4593	19
	4	[0, -40, -22]	Right Cerebellum, Sub-lobar, Fourth Ventricle, CSF	12,83	3
	5	[-48, -37, 62]	Left Cerebrum, Parietal Lobe, Inferior Parietal Lobule, GM,BA 40	7,3235	11
	6	[0, -40, -13]	Left Cerebellum, Anterior Cerebellum, Cerebellar Lingual, GM	6,669	12
	7	[0, -19, 5]	Inter-Hemispheric, CSF, Optic Tract	12,4677	23
	8	[0, -46, -28]	Right Cerebellum, Anterior Lobe, Nodule, GM	39,5873	14
	9	[0, -43, -19]	Right Cerebellum, Sub-lobar, Fourth Ventricle, CSF	8,5616	4
	10	[-54, 20, 2]	Left Cerebrum, Frontal Lobe, Inferior Frontal Gyrus, GM, BA 47	8,6901	13
	11	[0, -22, 5]	Inter-Hemispheric, CSF, Optic Tract	18,2984	7
	12	[3, -40, 2]	Inter-Hemispheric	17,7229	25
	13	[0, -19, 5]	Inter-Hemispheric, CSF, Optic Tract	12,7471	20
	14	[-15, 5, -19]	Left Cerebrum, Frontal lobe	14,1057	24
	15	[0, -40, -22]	Right Cerebellum, Sub-lobar, Fourth Ventricle, CSF	7,4182	16
	16	[-3, -43, -25]	Left Cerebellum, Anterior Lobe, GM	9,8502	21
	17	[9, -1, 26]	Right Cerebrum, Limbic Lobe, Cingulate Gyrus, WM	9,0432	17
	18	[-39, -67, -19]	Left Cerebellum, Posterior Lobe, Declive, GM	8,6073	10
	19	[0, -28, 5]	Inter-Hemispheric	23,2108	18
	20	[-3, -52, -31]	Left Cerebellum, Posterior Lobe, Cerebellar Tonsil, GM	10,4833	9

	21	[0, -4, -4]	Right Cerebrum, Sub-lobar, Third Ventricle, CSF	9,6748	22
	22	[0, -64, 35]	Left Cerebrum, Parietal Lobe, Precuneus	7,8884	2
	23	[3, -7, -22]	Right Brainstem, Pons	15,9875	15
	24	[0, -43, -28]	Right Cerebellum, Anterior Lobe, GM	10,2993	5
	25	[0, -49, -34]	Right Cerebellum, Sub-lobar, Fourth Ventricle, CSF	12,2752	6
13	1	[-3, -43, -13]	Left Cerebellum, Anterior Lobe, Cerebellar Lingual, GM	8,9098	18
	2	[0, -46, -19]	Right Cerebellum, Sub-lobar, Fourth Ventricle, CSF	8,4836	4
	3	[-42, -4, -4]	Left Cerebrum, Insula, GM, BA 13	11,8388	3
	4	[21, -82, -22]	Right Cerebellum, Posterior Lobe, Declive, GM	12,1192	4
	5	[-21, -70, 62]	Left Cerebrum, Parietal Lobe, Superior Parietal Lobule, GM, BA 7	5,3953	24
	6	[-39, -22, 8]	Left Cerebrum, Temporal Lobe, Superior Temporal Gyrus	9,4261	12
	7	[36, -49, -25]	Right Cerebellum, Anterior Lobe, Culmen, GM	6,0733	23
	8	[0, -46, -22]	Right Cerebellum, Sub-lobar, Fourth Ventricle, CSF	8,8147	14
	9	[45, -73, -16]	Right Cerebellum, Posterior Lobe, Declive, GM	5,7133	6
	10	[-54, 38, 11]	Left Cerebrum, Frontal Lobe, Inferior Frontal Gyrus, GM, BA 46	6,323	1
	11	[-39, -19, 11]	Left Cerebrum, Sub-lobar, Insula, GM, BA 13	10,9563	8
	12	[0, -43, 2]	Inter-Hemispheric	10,5668	2
	13	[-42, -10, 2]	Left Cerebrum, Sub-lobar, Insula	7,4355	17
	14	[24, -82, -22]	Right Cerebellum, Posterior Lobe, Declive, GM	9,5528	15
	15	[0, 59, 26]	Inter-Hemispheric	7,5807	22
	16	[36, 17, -25]	Right Cerebrum, Temporal Lobe, Superior Temporal Gyrus, GM, BA 38	6,1653	13
	17	[9, -7, 26]	Right Cerebrum, Limbic Lobe, Cingulate Gyrus, WM	8,427	20
	18	[24, -82, -22]	Right Cerebellum, Posterior Lobe, Declive, GM	18,6552	19
	19	[-15, -31, -10]	Left Cerebrum, Limbic Lobe	6,998	25
	20	[6, -88, 5]	Right Cerebrum, Occipital Lobe, Lingual Gyrus	7,392	10
	21	[0, -46, 11]	Inter-Hemispheric	5,8418	16

	22	[21, -85, -19]	Right Cerebellum, Posterior Lobe, Declive, GM	7,5283	7
	23	[-15, -31, -16]	Left Cerebellum, Anterior, Lobe, Culmen, GM	9,774	9
	24	[0, -64, 56]	Inter-Hemispheric	10,5887	5
	25	[0, -37, 71]	Inter-Hemispheric	6,9602	21
group	1	[0, -40, -16]	Left Brainstem, Midbrain	20,4335	8
	2	[12, -88, -16]	Right Cerebrum, Occipital Lobe, Lingual Gyrus, GM, BA 18	10,4907	23
	3	[42, 11, -13]	Right Cerebrum, Temporal Lobe, Superior Temporal Gyrus	13,0399	12
	4	[0, -40, -25]	Left Cerebellum, Anterior Lobe, GM	8,8913	1
	5	[15, -67, 68]	Right Cerebrum, Parietal Lobe, Superior Parietal Lobule	7,2967	11
	6	[57, 14, -1]	Right Cerebrum, Frontal-Temporal Space	6,2738	19
	7	[-27, -88, -19]	Left Cerebellum, Posterior Lobe, Declive, GM	7,5999	14
	8	[0, -46, -28]	Right Cerebellum, Anterior Lobe, Nodule, GM	30,9428	3
	9	[-15, -25, -31]	Left Brainstem, Pons	10,4626	24
	10	[-33, -73, 50]	Left Cerebrum, Parietal Lobe, Superior Parietal Lobule, GM, BA 7	5,9358	17
	11	[-18, -28, -25]	Left Brainstem, Pons	14,8655	13
	12	[0, -43, 5]	Inter-Hemispheric	22,7752	2
	13	[-3, -1, 11]	Left Cerebrum, Sub-lobar, Lateral CSF	10,8362	18
	14	[-18, 5, -19]	Left Cerebrum, Limbic Lobe, Uncus, GM, BA 34	13,6002	9
	15	[0, 44, 47]	Inter-Hemispheric	5,9436	4
	16	[0, -43, -25]	Left Cerebellum, Anterior Lobe, GM	8,5626	16
	17	[-6, -1, 23]	Left Cerebrum, Sub-lobar, Extra-Nuclear, WM, Corpus Callosum	10,9215	22
	18	[6, -85, -19]	Right Cerebellum, Posterior Lobe, Declive, GM	10,463	25
	19	[0, -25, -1]	Right Cerebrum, Sub-lobar, Third Ventricle, CSF	14,3136	7
	20	[0, -79, 14]	Inter-Hemispheric, Occipital Lobe, Cuneus	7,1435	5
	21	[45, 20, 41]	Right Cerebrum, Frontal Lobe, MiddleFrontal Gyrus, WM	5,6248	20
	22	[0, -64, 32]	Left Cerebrum, Occipital Lobe, Cuneus	8,0612	6

	23	[0, -7, -22]	Left Braintsem, Pons	24,1209	15
	24	[0, -64, 59]	Inter-Hemispheric	11,3618	10
	25	[0, -4, -4]	Right Cerebrum, Sub-lobar, Third Ventricle, CSF	7,7661	21

Table 7.3: The components with their coordinates and the related figured areas for the RLS group depicted in functional correlation matrix.

components	coordinates	brain areas
1	[10, -36, -15]	Right Cerebellum, Anterior Lobe, Culmen, GM
2	[8, 44, 5]	Right Cerebrum, Limbic Lobe, Anterior Cingulate, GM, BA 32
3	[-42, 2, 5]	Left Cerebrum, Sub-lobar, Insula, WM
4	[46, -10, 15]	Right Cerebrum, Parietal Lobe, Insula, WM
5	[12, -68, 65]	Right Cerebrum, Parietal Lobe, Superior Parietal Lobule
6	[50, 26, -5]	Right Cerebrum, Frontal Lobe, Inferior Frontal Gyrus, WM
7	[30, -76, 20]	Right Cerebrum, Occipital Lobe, Middle Occipital Gyrus, WM
8	[0, -54, -30]	Right Cerebellum, Anterior Lobe, Nodule, GM
9	[-20, -8, -20]	Left Cerebrum, Limbic Lobe, Parahippocampal Gyrus, WM
10	[-46, 28, 20]	Left Cerebrum, Frontal Lobe, Middle Frontal Gyrus, GM, BA 46
11	[34, 16, -25]	Right Cerebrum, Temporal Lobe, Superior Temporal Gyrus, GM, BA 38
12	[6, -46, 0]	Right Cerebellum, Anterior Lobe, Culmen, GM
13	[-6, 20, 0]	Right Cerebrum, Sub-lobar, Lateral Ventricle, CSF
14	[16, -4, -15]	Right Cerebrum, Limbic Lobe, Parahippocampal Gyrus, GM, BA 34
15	[-30, 28, 50]	Left Cerebrum, Frontal Lobe, Superior Frontal Gyrus, WM
16	[12, -34, 15]	Right Cerebrum, Sub-lobar, Lateral Ventricle, CSF
17	[8, 8, 20]	Right Cerebrum, Sub-lobar, Lateral Ventricle, CSF
18	[32, -68, -25]	Right Cerebellum, Posterior Lobe, Uvula, GM
19	[-8, -24, 15]	Left Cerebrum, Sub-lobar, Extra-Nuclear, WM
20	[6, -78, 5]	Right Cerebrum, Occipital Lobe, Lingual Gyrus, WM

21	[36, 20, 45]	Right Cerebrum, Frontal Lobe, Middle Frontal Gyrus, GM, BA 8
22	[-6, -48, 35]	Left Cerebrum, Parietal Lobe, Precuneus, GM, BA 31
23	[-6, -10, -20]	Left Brainstem, Pons
24	[6, -68, 55]	Inter-Hemispheric
25	[-16, -46, 65]	Left Cerebrum, Parietal Lobe, Postcentral Gyrus, WM

Table 7.4: The components with their coordinates and the related figured areas for the group of controls depicted in functional correlation matrix.

components	coordinates	brain areas
1	[48, 32, -10]	Right Cerebrum, Frontal Lobe, Inferior Frontal Gyrus, WM
2	[18, -82, -25]	Right Cerebellum, Posterior Lobe, Uvula, GM
3	[-28, 0, -25]	Left Cerebrum, Temporal Lobe, Sub-Gyral, WM
4	[-8, -58, 50]	Right Cerebrum, Parietal Lobe, Precuneus, GM, BA 7
5	[-18, -42, 5]	Left Cerebrum, Limbic Lobe, Parahippocampal Gyrus, WM
6	[0, -46, 50]	Left Cerebrum, Parietal Lobe, Precuneus
7	[-30, -32, -10]	Left Cerebrum, Limbic Lobe, Parahippocampal Gyrus, WM
8	[-42, -40, 35]	Left Cerebrum, Parietal Lobe, Supramarginalis Gyrus, GM, BA 40
9	[36, 56, 20]	Right Cerebrum, Frontal Lobe, Middle Frontal Gyrus, GM, BA 10
10	[-50, 12, -5]	Left Cerebrum, Temporal Lobe, Superior Temporal Gyrus, GM, BA 22
11	[-48, 32, 30]	Left Cerebrum, Frontal Lobe, Middle Frontal Gyrus, GM, BA 9
12	[-2, 38, 50]	Left Cerebrum, Frontal Lobe, Superior Frontal Gyrus
13	[0, -40, 15]	Inter-Hemispheric, WM, Corpus Callosum
14	[-36, -2, 65]	Left Cerebrum, Frontal Lobe, Middle Frontal Gyrus
15	[-18, 26, 10]	Left Cerebrum, Sub-lobar, Extra-Nuclear, WM
16	[-26, -4, -15]	Left Cerebrum, Limbic Lobe, Parahippocampal Gyrus, GM, Amygdala
17	[-12, -64, -5]	Left Cerebrum, Occipital Lobe, Lingual Gyrus
18	[6, -40, 70]	Right Cerebrum, Parietal Lobe, Postcentral Gyrus, GM, BA 5
19	[-6, -4, 40]	Left Cerebrum, Limbic Lobe, Cingulate Gyrus, WM
20	[50, 38, -10]	Right Cerebrum, Frontal Lobe, Inferior Frontal Gyrus, WM
21	[8, 54, 20]	Right Cerebrum, Frontal Lobe, Medial Frontal Gyrus, WM

22	[12, -46, 80]	Right Cerebrum, Frontal Lobe, Superior Frontal Gyrus, WM
23	[18, 36, 40]	Right Cerebrum, Frontal Lobe, Superior Frontal Gyrus, WM
24	[0, 2, 10]	Inter-Hemispheric

Table 7.5: Functionally connected areas assuming the right middle frontal gyrus as seed for RLS group.

MNI coordinates of maximum voxel	Cluster size (voxels)	Brain areas	Size p-FWE	Size p-unc	Peak p-FWE	Peak p-unc
[48, 24, 32]	56571	Right Cerebrum, Frontal Lobe, Middle Frontal Gyrus	0.000000	0.000000	0.000001	0.000000
[24, -58, -24]	1083	Right Cerebellum, Posterior Lobe, Declive, GM	0.000000	0.000000	0.444681	0.000004
[-12, -6, 2]	858	Left Cerebrum, Sub-lobar, Thalamus, GM	0.000000	0.000000	0.167847	0.000001
[16, -4, 14]	787	Right Cerebrum, Sub-lobar, Extra-Nuclear, WM	0.000000	0.000000	0.275920	0.000002
[-56, -60, -12]	644	Left Cerebrum, Occipital Lobe, Middle Occipital Gyrus, GM, BA 19	0.000000	0.000000	0.633112	0.000008
[-56, -36, 8]	501	Left Cerebrum, Temporal Lobe, Superior Temporal Gyrus, WM	0.000003	0.000000	0.400471	0.000003
[30, -6, -42]	214	Right Cerebrum, Limbic Lobe Uncus, GM, BA 20	0.003168	0.000126	0.519575	0.000005
[-32, -42, -34]	163	Left Cerebellum, Anterior Lob, Culmen, GM	0.013978	0.000560	0.199487	0.000001
[16, -58, -48]	140	Right Cerebellum, Posterior Lobe, Cerebellar Tonsil, GM	0.028562	0.001153	0.881857	0.000022
[-56, -22, -34]	91	Left Cerebrum, Temporal Lobe, Fusiform Gyrus	0.145171	0.006242	0.240116	0.000001
[64, -18, 18]	90	Right Cerebrum, Parietal Lobe, Postcentral Gyrus, WM	0.150246	0.006479	0.928131	0.000031
[12, 14, -22]	85	Right Cerebrum, Frontal Lobe, Medial Frontal Gyrus, GM, BA 25	0.178450	0.007823	0.992606	0.000077
[40, -6, 18]	82	Right Cerebrum, Sub-lobar, Insula, GM, BA 13	0.197864	0.008775	0.993725	0.000080

Table 7.6: Functionally connected areas assuming the right middle frontal gyrus as seed for controls group.

MNI coordinates of maximum voxel	Cluster size (voxels)	Brain areas	Size p-FWE	Size p-unc	Peak p-FWE	Peak p-unc
[34, 14, 32]	2622	Right Cerebrum, Frontal Lobe, Middle Frontal Gyrus, WM	0.000000	0.000000	0.104722	0.000000
[16, -72, 56]	1593	Right Cerebrum, Parietal Lobe, Precuneus, WM	0.000000	0.000000	0.111911	0.000000

[-48, 8, 42]	968	Left Cerebrum. Frontal Lobe, Middle Frontal Gyrus, GM, BA 8	0.000000	0.000000	0.295646	0.000001
[-42, -60, 54]	940	Left Cerebrum, Parietal Lobe, Inferior Parietal Lobule	0.000000	0.000000	0.979886	0.000004
[-2, 30, 42]	769	Left Cerebrum, Frontal Lobe, Medial Frontal Gyrus, GM, BA 8	0.000000	0.000000	0.999776	0.000005
[-36, -60, -36]	455	Left Cerebellum, Posterior Lobe, Tuner, GM	0.000000	0.000000	0.999746	0.000005
[6, -42, 48]	280	Right Cerebrum, Parietal Lobe, Precuneus, WM	0.000000	0.000000	0.999993	0.000012
[70, -30, -12]	158	Right Cerebrum, Temporal Lobe, Middle Temporal Gyrus, GM, BA 21	0.000055	0.000001	1.000000	0.000036
[-24, -4, -36]	154	Left Cerebrum, Limbic Lobe, Uncus, WM	0.000070	0.000001	0.999971	0.000009
[24, -82, -18]	146	Right Cerebrum, Occipital Lobe, Lingual Gyrus, WM	0.000114	0.000002	0.267704	0.000001
[36, 60, 14]	144	Right Cerebrum, Frontal Lobe, Middle Frontal Gyrus, WM	0.000128	0.000002	0.999999	0.000018
[40, -70, 36]	128	Right Cerebrum, Parietal Lobe, Precuneus, GM, BA 39	0.000345	0.000005	1.000000	0.000084
[22, -6, 6]	123	Right Cerebrum, Sub-lobar, Lentiform Nucleus, GM, Lateral Globus Pallidus	0.000474	0.000007	1.000000	0.000033
[-54, -42, 14]	116	Left Cerebrum, Temporal Gyrus, Superior Temporal Gyrus, WM	0.000745	0.000012	0.263277	0.000001
[-12, -52, -42]	97	Left Cerebellum, Anterior Lobe, Culmen, GM	0.002666	0.000042	0.999998	0.000016
[-12, -16, 6]	91	Left Cerebrum, Sub-lobar, Thalamus, GM, Medial Dorsal Nucleus	0.004054	0.000064	0.999999	0.000020
[0, 48, 48]	90	Inter-Hemispheric	0.004351	0.000069	1.000000	0.000063
[-54, -60, -16]	88	Left Cerebrum, Temporal Lobe, Inferior Temporal Gyrus, WM	0.005016	0.000079	1.000000	0.000027
[68, -48, -6]	87	Right Cerebrum, Temporal Lobe, Middle Temporal Gyrus	0.005388	0.000085	0.171888	0.000001
[24, -10, -40]	77	Right Cerebrum, Limbic Lobe, Uncus	0.011177	0.000177	1.000000	0.000024
[46, -60, -46]	59	Right Cerebellum, Posterior Lobe, Inferior Semi-Lunar Lobule, GM	0.044780	0.000722	0.050978	0.000000
[12, 54, 8]	53	Right Cerebrum, Frontal Lobe, Medial Frontal Gyrus, WM	0.072692	0.001189	1.000000	0.000039
[-54, 28, -12]	53	Left Cerebrum, Frontal Gyrus, Inferior Frontal Gyrus, GM, BA 47	0.072692	0.001189	1.000000	0.000045
[22, -18, -18]	50	Right Cerebrum, Limbic Lobe, Parahippocampal Gyrus, WM	0.092939	0.001537	1.000000	0.000024
[50, 14, -44]	50	Right Cerebrum, Temporal Lobe, Middle Temporal Gyrus, GM, BA 21	0.092939	0.001537	1.000000	0.000152
[6, -46, 72]	42	Right Cerebrum, Parietal Lobe, Postcentral Gyrus, GM, BA 5	0.180103	0.003129	0.999777	0.000005

[0, -16, -18]	42	Left Brainstem, Midbrain	0.180103	0.003129	1.000000	0.000090
[-8, -90, -34]	41	Left Cerebellum, Posterior Lobe, Pyramis, GM	0.195627	0.003430	1.000000	0.000030
[-20, -76, 20]	40	Left Cerebrum, Occipital Lobe, Precuneus	0.212450	0.003763	1.000000	0.000377
[-26, -84, -16]	40	Left Cerebrum, Occipital Lobe, Middle Occipital Gyrus, GM, BA18	0.212450	0.003763	1.000000	0.000083
[16, -52, 38]	37	Right Cerebrum, Parietal Lobe, Precuneus, WM	0.271572	0.004993	0.999846	0.000006
[-38, -64, -18]	35	Left Cerebrum, Occipital Lobe, Sub-Gyral, WM	0.319022	0.006054	1.000000	0.000032
[-44, -76, 18]	34	Left Cerebrum, Temporal Lobe, Middle Temporal Gyrus, WM	0.345366	0.006675	1.000000	0.000021
[-38, 14, 54]	30	Left Cerebrum, Frontal Lobe, Superior Frontal Gyrus, WM	0.468845	0.009969	1.000000	0.000099
[-30, 38, 42]	29	Left Cerebrum, Frontal Lobe, Middle Frontal Gyrus, GM, BA 8	0.504077	0.011050	0.999997	0.000014
[-50, -24, 0]	29	Left Cerebrum, Temporal Lobe, Middle Temporal Gyrus, WM	0.504077	0.011050	1.000000	0.000074

Table 7.7: Functionally connected areas assuming the right thalamus as seed for RLS group.

MNI coordinates of maximum voxel	**Cluster size (voxels)**	**Brain areas**	**Size p-FWE**	**Size p-unc**	**Peak p-FWE**	**Peak p-unc**
[6, -22, 12]	20017	Right Cerebrum, Sub-lobar, Extra-Nuclear, WM	0.000000	0.000000	0.000002	0.000000
[10, 44, 42]	963	Right Cerebrum, Frontal Lobe, Medial Frontal Gyrus, WM	0.000000	0.000000	0.051319	0.000000
[66, 0, -6]	894	Right Cerebrum, Temporal Lobe, Superior Temporal Gyrus, GM, BA 22	0.000000	0.000000	0.145411	0.000001
[-18, -76, -34]	650	Left Cerebellum, Posterior Lobe, Uvula, GM	0.000000	0.000000	0.260587	0.000001
[-50, 26, 14]	515	Left Cerebrum, Frontal Lobe, Inferior Frontal Gyrus, WM	0.000000	0.000000	0.850226	0.000015
[58, -34, 14]	394	Left Cerebrum, Temporal Lobe, Superior Temporal Gyrus, WM	0.000008	0.000000	0.310173	0.000001
[-54, -12, 30]	312	Left Cerebrum, Frontal Lobe, Precentral Gyrus, WM	0.000068	0.000002	0.779401	0.000011
[4, 24, 18]	261	Right Cerebrum, Sub-lobar, Extra-Nuclear, WM, Corpus Callosum	0.000291	0.000010	0.047124	0.000000
[42, -66, 42]	250	Right Cerebrum, Parietal Lobe, Inferior Parietal Lobe, Inferior Parietal Lobule, GM, BA39	0.000403	0.000014	0.375673	0.000002
[-54, -16, 2]	222	Left Cerebrum, Temporal Lobe, Superior Temporal Gyrus, WM	0.000946	0.000032	0.383343	0.000002

[6, 6, 54]	161	Right Cerebrum, Frontal Lobe, Superior Frontal Gyrus, GM, BA 6	0.006947	0.000234	0.782565	0.000011
[58, -4, 20]	142	Right Cerebrum, Frontal Lobe, Precentral Gyrus, WM	0.013549	0.000459	0.787013	0.000011
[66, -22, -4]	116	Right Cerebrum, Temporal Lobe, Superior Temporal Gyrus, WM	0.035333	0.001209	0.602354	0.000005
[24, 8, -36]	115	Right Cerebrum, Limbic Lobe, Uncus, GM, BA 28	0.036700	0.001257	0.988666	0.000052
[-56, -46, -4]	108	Left Cerebrum, Temporal Lobe, Middle Temporal Gyrus, WM	0.047980	0.001653	0.997206	0.000078
[-12, -64, 56]	107	Left Cerebrum, Parietal Lobe, Precuneus, GM, BA 7	0.049869	0.001720	0.577250	0.000005
[10, 60, -16]	104	Right Cerebrum, Frontal Lobe, Medial Frontal Gyrus, WM	0.056021	0.001938	0.928631	0.000023
[-32, -12, 8]	101	Left Cerebrum, Sub-lobar, Claustrum, GM	0.062977	0.002187	0.928631	0.000024
[24, -48, -48]	94	Right Cerebellum, Posterior Lobe, Cerebellar Tonsil, GM	0.086332	0.002912	0.733901	0.000009
[-56, 26, -4]	93	Left Cerebrum, Frontal Lobe, Inferior Frontal Gyrus, GM	0.086332	0.003035	0.151376	0.000001
[46, -70, -10]	93	Right Cerebrum, Occipital Lobe, Middle Occipital Gyrus, WM	0.097283	0.003035	0.992488	0.000059
[-54, 8, 20]	90	Left Cerebrum, Frontal Lobe, Inferior Frontal Gyrus, WM	0.097283	0.003440	0.992690	0.000060
[-38, -12, -16]	90	Left Cerebrum, Temporal Lobe, Sub-Gyral WM	0.134095	0.003440	0.552131	0.000004
[-50, 20, -24]	82	Left Cerebrum, Temporal Lobe, Superior Temporal Gyrus, WM	0.134095	0.001840	0.978226	0.000041

Table 7.8: Functionally connected areas assuming the right thalamus as seed for controls group.

MNI coordinates of maximum voxel	Cluster size (voxels)	Brain areas	Size p-FWE	Size p-unc	Peak p-FWE	Peak p-unc
[16, -12, 12]	1290	Right Cerebrum, Sub-lobar, Thalamus, GM, Ventral Lateral Nucleus	0.000000	0.000000	0.136704	0.000001
[-26, 38, 48]	423	Left Cerebrum, Frontal Lobe, Middle Frontal Gyrus	0.000000	0.000000	0.999627	0.000007
[46, 20, 48]	296	Right Cerebrum, Frontal Lobe, Middle Frontal Gyrus, GM, BA 8	0.000000	0.000000	0.471483	0.000002
[0, -58, 24]	184	Inter-hemispheric	0.000052	0.000001	0.999999	0.000030
[0, -90, -6]	179	Inter-hemispheric, Occipital Lobe	0.000066	0.000001	0.999101	0.000005
[-20, -72, 60]	123	Left Cerebrum, Parietal Lobe, Superior Parietal Lobule, GM, BA 7	0.001350	0.000025	0.999999	0.000025
[36, -22, 6]	105	Right Cerebrum, Sub-lobar, Claustrum, GM	0.003896	0.000072	0.999988	0.000016

[-44, 20, -34]	94	Left Cerebrum, Temporal Lobe, Superior Temporal Gyrus, GM, BA 38	0.007665	0.000142	0.999428	0.000006
[52, 32, -10]	78	Right Cerebrum, Frontal Lobe, Inferior Frontal Gyrus, WM	0.021464	0.000399	1.000000	0.000033
[52, 8, -42]	71	Right Cerebrum, Temporal Lobe, Middle Temporal Gyrus	0.034308	0.000642	1.000000	0.000045
[42, -58, 24]	68	Right Cerebrum, Temporal Lobe, Middle Temporal Gyrus, GM, BA 39	0.042094	0.000791	1.000000	0.000053
[36, 24, 26]	59	Right Cerebrum, Frontal Lobe, Middle Frontal Gyrus, WM	0.078698	0.001507	1.000000	0.000103
[4, 62, -6]	56	Right Cerebrum	0.097294	0.001882	0.521546	0.000002
[-8, -18, -24]	53	Left Brainstem, Midbrain	0.120441	0.002360	0.999996	0.000020
[46, -18, -18]	42	Right Cerebrum, Temporal Lobe, Sub-Gyral, WM	0.263621	0.005628	1.000000	0.000087
[-42, 36, -22]	42	Left Cerebrum	0.263621	0.005628	1.000000	0.000077

Table 7.9: Functionally connected areas assuming the left thalamus as seed for RLS group.

MNI coordinates of maximum voxel	**Cluster size (voxels)**	**Brain areas**	**Size p-FWE**	**Size p-unc**	**Peak p-FWE**	**Peak p-unc**
[-8, -28, -4]	12204	Left Brainstem, Midbrain	0.000000	0.000000	0.000001	0.000000
[-30, 12, 48]	10975	Left Cerebrum, Frontal Lobe, Middle Frontal Gyrus, GM, BA 6	0.000000	0.000000	0.003900	0.000000
[42, -28, 44]	1017	Right Cerebrum, Parietal Lobe, Postcentral Gyrus, GM, BA 2	0.000000	0.000000	0.352472	0.000002
[-26, -82, -28]	797	Left Cerebellum, Posterior Lobe, Declive, GM	0.000000	0.000000	0.152065	0.000001
[60, -64, 6]	718	Right Cerebrum, Temporal Lobe, Middle Temporal Gyrus, GM, BA 39	0.000000	0.000000	0.567643	0.000005
[-38, -12, -16]	407	Left Cerebrum, Temporal Lobe, Sub-lobar, WM	0.000011	0.000000	0.179451	0.000001
[52, -10, -34]	342	Right Cerebrum, Temporal Lobe, Fusiform Gyrus, WM	0.000053	0.000002	0.164688	0.000001
[-44, 24, -18]	253	Left Cerebrum, Frontal Lobe, Inferior Frontal Gyrus, GM, BA 47	0.000584	0.000021	0.911514	0.000023
[4, 66, -18]	178	Inter-hemispheric	0.005526	0.000199	0.847536	0.000016
[60, -46, -10]	156	Right Cerebrum, Temporal Lobe, Middle Temporal Gyrus, WM	0.011291	0.000409	0.975877	0.000044
[46, 2, -42]	98	Right Cerebrum, Temporal Lobe, Middle Temporal Gyrus	0.086831	0.003269	0.916537	0.000024

Table 7.10: Functionally connected areas assuming the left thalamus as seed for controls group.

MNI coordinates of maximum voxel	Cluster size (voxels)	Brain areas	Size p-FWE	Size p-unc	Peak p-FEW	Peak p-unc
[-2, -16, 8]	1274	Inter-hemispheric, Sub-lobar, Extra-Nuclear, WM	0.000000	0.000000	0.021608	0.000000
[10, -60, 68]	279	Right Cerebrum, Parietal Lobe, Precuneus, WM	0.000000	0.000000	0.999987	0.000014
[-36, -66, 38]	244	Left Lobe, Precuneus, GM, BA 39	0.000002	0.000000	0.999958	0.000011
[-42, 12, 56]	236	Left Cerebrum, Frontal Lobe, Middle Frontal Gyrus, GM, BA 6	0.000003	0.000000	0.999999	0.000026
[40, 30, 44]	178	Right Cerebrum, Frontal Lobe, Middle Frontal Gyrus, GM, BA 8	0.000047	0.000001	0.999438	0.000005
[-32, 20, -40]	101	Left Cerebrum, Temporal Lobe, Superior Temporal Gyrus, WM	0.003869	0.000068	0.999539	0.000006
[34, -18, 2]	96	Right Cerebrum, Sub-lobar, Extra-Nuclear, WM	0.005321	0.000094	0.999581	0.000086
[24, 12, 6]	84	Right Cerebrum, Sub-lobar, Lentiform Nucleus, GM, Putamen	0.011686	0.000207	1.000000	0.000086
[6, -60, 18]	78	Right Cerebrum, Limbic Lobe, Posterior Cingulate, GM, BA 23	0.017539	0.000311	1.000000	0.000060
[-8, 56, 38]	73	Left Cerebrum, Frontal Lobe, Superior Frontal Gyrus, GM, BA 9	0.024770	0.000441	1.000000	0.000032
[42, -54, 38]	68	Right Cerebrum, Parietal Lobe, Supramarginal Gyrus, WM	0.035207	0.000630	1.000000	0.000074
[24, 48, 42]	66	Right Cerebrum, Frontal Lobe, Superior Frontal Gyrus, GM, BA 8	0.040597	0.000729	1.000000	0.000094
[48, -58, 18]	49	Right Cerebrum, Temporal Lobe, Superior Temporal Gyrus, WM	0.141205	0.002676	0.999993	0.000016
[-26, -70, 54]	48	Left Cerebrum, Parietal Lobe, Superior Parietal Lobule, GM, BA 7	0.152145	0.002901	0.999982	0.000013
[-50, 8, -24]	45	Left Cerebrum, Temporal Lobe, Middle Temporal Gyrus, WM	0.190297	0.003711	0.999981	0.000013
[46, -52, -40]	45	Right Cerebellum, Posterior Lobe, Tuner, GM	0.190297	0.003711	1.000000	0.000036

Table 7.11: Functionally connected areas assuming the precuneus cortex as seed for RLS group.

MNI coordinates of maximum voxel	Cluster size (voxels)	Brain areas	Size p-FWE	Size p-unc	Peak p-FEW	Peak p-unc
[0, -70, 38]	63257	Left Cerebrum, Parietal Lobe, Precuneus	0.000000	0.000000	0.000000	0.000000
[-30, 30, 2]	5558	Left Cerebrum, Frontal Gyrus, Sub-lobar, WM	0.000000	0.000000	0.011784	0.000000

[-54, -30, 2]	235	Left Cerebrum, Temporal Lobe, Superior Temporal Gyrus, GM, BA 22	0.001859	0.000075	0.852401	0.000019
[-6, 68, -16]	191	Left Cerebrum, Frontal Lobe, Medial Frontal Gyrus, GM, BA 11	0.006324	0.000254	0.818506	0.000016
[16, 6, 8]	188	Right Cerebrum, Sub-lobar, Extra-Nuclear, WM	0.006896	0.000278	0.631498	0.000008
[42, 18, -22]	181	Right Cerebrum, Temporal Lobe, Superior Temporal Gyrus	0.008455	0.000341	0.886716	0.000023
[10, 14, -22]	151	Right Cerebrum, Frontal Lobe, Medial Frontal Gyrus, GM, BA 25	0.020846	0.000845	0.719499	0.000011
[-14, 12, -22]	142	Left Cerebrum, Frontal Lobe	0.027598	0.001123	0.348847	0.000002
[-6, -46, -48]	112	Left Cerebellum, Posterior Lobe, Cerebellar Tonsil, GM	0.072827	0.003033	0.997855	0.000109
[-44, 26, -32]	88	Left Cerebrum, Temporal Lobe, Superior Temporal Gyrus, GM, BA 38	0.163804	0.007175	0.904850	0.000026
[-2, 24, -10]	85	Left Cerebrum, Limbic Lobe, Anterior Cingulate	0.181486	0.008033	0.001287	0.000000

Table 7.12: Functionally connected areas assuming the precuneus cortex as seed for controls group.

MNI coordinates of maximum voxel	Cluster size (voxels)	Brain areas	Size p-FWE	Size p-unc	Peak p-FWE	Peak p-unc
[-38, -78, 32]	7020	Left Cerebrum, Temporal Lobe, Angular Gyrus, GM, BA 39	0.000000	0.000000	0.028368	0.000000
[40, -72, 48]	354	Right Cerebrum, Parietal Lobe, Inferior Parietal Lobule, GM, BA 7	0.000000	0.000000	0.999997	0.000019
[28, -18, -16]	215	Right Cerebrum, Limbic Lobe, Parahippocampal Gyrus, WM	0.000001	0.000000	0.591580	0.000002
[30, 32, 54]	194	Right Cerebrum, Frontal Lobe, Superior Frontal Gyrus	0.000019	0.000000	0.095627	0.000000
[-50, -48, 36]	167	Left Cerebrum, Parietal Lobe, Supramarginal Gyrus, WM	0.000079	0.000001	0.999995	0.000017
[-30, -40, -16]	131	Left Cerebrum, Limbic Lobe, Parahippocampal Gyrus, WM	0.000595	0.000010	0.999450	0.000005
[-32, -82, -40]	118	Left Cerebellum, Posterior Lobe, Tuner, GM	0.001288	0.000022	1.000000	0.000006
[24, 26, 30]	117	Right Cerebrum, Frontal Lobe Sub-Gyral, WM	0.001368	0.000024	0.999991	0.000015
[18, -58, -46]	89	Right Cerebellum, Posterior Lobe, Cerebellar Tonsil, GM	0.008039	0.000141	1.000000	0.000056
[-6, 44, 24]	81	Left Cerebrum, Frontal Lobe, Medial Frontal Gyrus, BA 9	0.013752	0.000241	1.000000	0.000030
[-42, 24, 36]	80	Left Cerebrum, Frontal Lobe, Precentral Gyrus, GM, BA 9	0.014723	0.000259	0.999952	0.000010
[10, -24, 8]	75	Right Cerebrum, Sub-lobar, Thalamus, GM, Pulvinar	0.020784	0.000366	0.053671	0.000000

[10, 68, -4]	75	Right Cerebrum, Frontal Lobe, Medial Frontal Gyrus, WM	0.020784	0.000366	0.999966	0.000011
[10, 50, 48]	61	Right Cerebrum, Frontal Lobe, Superior Frontal Gyrus, GM, BA 8	0.056479	0.001014	0.700242	0.000003
[34, 20, -42]	59	Right Cerebrum, Temporal Lobe, Superior Temporal Gyrus, WM	0.065411	0.001179	1.000000	0.000100
[10, 44, 32]	58	Right Cerebrum, Frontal Lobe, Medial Frontal Gyrus, WM	0.070418	0.001273	1.000000	0.000029
[-42, -28, 60]	47	Left Cerebrum, Parietal Lobe, Postcentral Gyrus, WM	0.160247	0.003045	0.999851	0.000007
[-20, 44, 48]	45	Left Cerebrum, Frontal Lobe, Superior Frontal Gyrus, GM, BA 8	0.186244	0.003593	1.000000	0.000030
[-30, -40, -40]	41	Left Cerebellum, Posterior Lobe, Cerebellar Tonsil, GM	0.251119	0.005042	1.000000	0.000082
[-54, -22, -18]	39	Left Cerebrum, Temporal Lobe, Middle Temporal Gyrus, WM	0.291036	0.005997	1.000000	0.000327

Table 7.13: Functionally connected areas assuming the right occipital lobe as seed for RLS group.

MNI coordinates of maximum voxel	Cluster size (voxels)	Brain areas	Size p-FWE	Size p-unc	Peak p-FWE	Peak p-unc
[6, -94, 12]	15512	Right Cerebrum, Occipital Lobe, Cuneus, WM	0.000000	0.000000	0.000173	0.000000
[6, -6, 74]	404	Right Cerebrum, Frontal Lobe, Superior Frontal Gyrus, GM, BA 6	0.000008	0.000000	0.412680	0.000003
[58, -18, -12]	398	Right Cerebrum, Temporal Lobe, Middle Temporal Gyrus, WM	0.000009	0.000000	0.588603	0.000005
[46, 24, -10]	293	Right Cerebrum, Frontal Lobe, Inferior Frontal Gyrus, WM	0.000141	0.000005	0.807652	0.000013
[-48, -76, -36]	180	Left Cerebellum, Posterior Lobe, Tuner, GM	0.004182	0.000145	0.784344	0.000011
[18, -48, -18]	173	Right Cerebellum, Anterior Lobe, Culmen, GM	0.005264	0.000182	0.489990	0.000003
[-26, 56, 12]	151	Left Cerebrum, Frontal Lobe, Middle Frontal Gyrus, WM	0.011073	0.000384	0.287695	0.000001
[-38, 30, 6]	133	Left Cerebrum, Frontal Lobe, Inferior Frontal Gyrus, WM	0.020856	0.000727	0.830202	0.000014
[-36, 12, 30]	125	Left Cerebrum, Frontal Lobe, Middle Frontal Gyrus, WM	0.027850	0.000974	0.803689	0.000012
[-62, -32, 2]	116	Left Cerebrum, Temporal Lobe, Middle Temporal Gyrus, GM, BA 22	0.038790	0.001365	0.994087	0.000066
[36, -58, 60]	114	Right Cerebrum, Parietal Lobe, Superior Parietal Lobule, GM, BA 7	0.041789	0.001473	0.993956	0.000066
[-18, -40, -28]	106	Left Cerebellum, Anterior Lobe, Culmen, GM	0.056471	0.002005	0.623279	0.000006
[36, -4, 68]	102	Right Cerebrum, Frontal Lobe, Middle Frontal Gyrus	0.065767	0.002347	0.357408	0.000002
[-36, 2, 66]	85	Left Cerebrum, Middle Frontal Gyrus, WM	0.127186	0.004693	0.977973	0.000043

Table 7.14: Functionally connected areas assuming the right occipital lobe as seed for controls group.

MNI coordinates of maximum voxel	Cluster size (voxels)	Brain areas	Size p-FWE	Size p-unc	Peak p-FWE	Peak p-unc
[10, -96, 6]	1229	Right Cerebrum, Occipital Lobe, Cuneus, WM	0.000000	0.000000	0.369500	0.000002
[0, -82, 32]	742	Left Cerebrum, Occipital Lobe	0.000000	0.000000	0.999890	0.000006
[42, -72, -16]	602	Right Cerebrum, Occipital Lobe, Middle Occipital Gyrus, GM, BA 18	0.000000	0.000000	0.896725	0.000004
[-24, -72, -22]	574	Left Cerebellum, Posterior Lobe, Declive, GM	0.000000	0.000000	0.697325	0.000003
[-26, 36, 48]	120	Left Cerebrum, Frontal Lobe, Middle Frontal Gyrus	0.000424	0.000006	1.000000	0.000029
[24, -48, -22]	118	Right Cerebellum, Anterior Lobe, Culmen, GM	0.000485	0.000007	0.418135	0.000002
[-18, -100, -10]	113	Left Cerebrum, Occipital Lobe, Lingual Gyrus, WM	0.000679	0.000010	0.999994	0.000011
[-20, -82, 6]	112	Left Cerebrum, Occipital Lobe, Lingual Gyrus, GM, BA 18	0.000726	0.000011	0.272768	0.000001
[-8, -42, 2]	111	Left Cerebellum, Culmen, GM	0.000778	0.000012	0.999999	0.000016
[10, 54, 44]	72	Right Cerebrum, Frontal Lobe, Superior Frontal Gyrus, GM, BA 9	0.013299	0.000202	0.694901	0.000003
[42, -60, 20]	62	Right Cerebrum, Temporal Lobe, Middle Temporal Gyrus, GM, BA 39	0.029562	0.000453	1.000000	0.000055
[36, -70, 50]	58	Right Cerebrum, Parietal Lobe, Superior Parietal Lobule, GM, BA 7	0.041074	0.007337	1.000000	0.000072
[-26, -76, 48]	56	Left Cerebrum, Parietal Lobe, Superior Parietal Lobule, GM, BA 7	0.048511	0.008030	1.000000	0.000019
[-24, -94, 20]	42	Left Cerebrum, Occipital Lobe, Middle Occipital Gyrus, GM, BA 18	0.160140	0.026170	1.000000	0.000186

Table 7.15: Functionally connected areas assuming the left occipital lobe as seed for RLS group.

MNI coordinates of maximum voxel	Cluster size (voxels)	Brain areas	Size p-FWE	Size p-unc	Peak p-FWE	Peak p-unc
[-8, -96, -16]	18824	Left Cerebrum, Occipital Lobe, Lingual Gyrus, WM	0.000000	0.000000	0.000279	0.000000
[52, 26, -10]	1240	Right Cerebrum, Frontal Lobe, Inferior Frontal Gyrus, WM	0.000000	0.000000	0.120211	0.000000
[-60, -16, -4]	577	Left Cerebrum, Temporal Lobe, Superior Temporal Gyrus, WM	0.000000	0.000000	0.686523	0.000009

[12, 36, -16]	350	Right Cerebrum, Frontal Lobe, Medial Frontal Gyrus, WM	0.000060	0.000002	0.928775	0.000028
[54, 32, 14]	276	Right Cerebrum, Frontal Lobe, Inferior Frontal Gyrus	0.000405	0.000015	0.706881	0.000009
[-36, 60, 0]	212	Left Cerebrum, Frontal Lobe, Middle Frontal Gyrus, WM	0.002423	0.000091	0.984758	0.000055
[-20, -42, -30]	208	Left Cerebellum, Anterior Lobe, Culmen, GM	0.002725	0.000102	0.276521	0.000001
[54, 32, 14]	198	Right Cerebrum, Frontal Lobe, Inferior Frontal Gyrus	0.003665	0.000138	0.836073	0.000016
[36, -72, 54]	149	Right Cerebrum, Parietal Lobe, Superior Parietal Lobule, GM, BA 7	0.016900	0.000639	0.788660	0.000013
[-14, 24, 50]	143	Left Cerebrum, Frontal Lobe, Superior Frontal Gyrus, WM	0.020579	0.000779	0.859373	0.000018
[10, 44, 38]	134	Right Cerebrum, Frontal Lobe, Medial Frontal Gyrus, WM	0.027776	0.001056	0.831449	0.000016
[48, 6, -12]	112	Right Cerebrum, Sub-lobar, Insula, GM, BA 22	0.059159	0.002285	0.980625	0.000051
[-38, -64, 44]	111	Left Cerebrum, Parietal Lobe, Inferior Parietal Lobule, WM	0.061274	0.002369	0.992183	0.000069
[40, -4, 56]	108	Right Cerebrum, Frontal Lobe, Middle Frontal Gyrus, GM, BA 6	0.068113	0.002643	0.337195	0.000002
[-24, -18, 0]	107	Left Cerebrum, Sub-lobar, Extra-Nuclear, WM	0.070567	0.002742	0.220617	0.000001
[-18, 12, -22]	103	Left Cerebrum, Frontal Lobe, Inferior Frontal Gyrus	0.081349	0.003179	0.743984	0.000011

Table 7.16: Functionally connected areas assuming the left occipital lobe as seed for controls group.

MNI coordinates of maximum voxel	Cluster size (voxels)	Brain areas	Size p-FWE	Size p-unc	Peak p-FWE	Peak p-unc
[-8, -84, 18]	1318	Left Cerebrum, Occipital Lobe, Cuneus, WM	0.000000	0.000000	0.367967	0.000002
[30, -90, 20]	510	Right Cerebrum, Occipital Lobe, Middle Occipital Gyrus, GM BA 19	0.000000	0.000000	0.844837	0.000003
[18, -78, 44]	130	Right Cerebrum, Parietal Lobe, Precuneus, GM, BA 7	0.000375	0.000006	1.000000	0.000029
[42, -72, -10]	129	Right Cerebrum, Occipital Lobe, Inferior Occipital Gyrus, BA 19	0.000399	0.000006	1.000000	0.000030
[-2, 56, 36]	118	Left Cerebrum, Frontal Lobe, Superior Frontal Gyrus, GM, BA 9	0.000795	0.000013	1.000000	0.000026
[24, -58, -12]	70	Right Cerebrum, Limbic Lobe, Parahippocampal Gyrus, WM	0.021543	0.000353	1.000000	0.000225
[-12, -48, -10]	69	Left Cerebellum, Anterior Lobe, Culmen, GM	0.023222	0.000381	1.000000	0.000166
[54, 0, 48]	67	Right Cerebrum, Frontal Lobe, Precentral Gyrus, GM, BA 6	0.027006	0.000444	0.999998	0.000017
[-30, 30, 50]	46	Left Cerebrum, Frontal Lobe, Middle Frontal Gyrus, WM	0.140720	0.002458	1.000000	0.000217

[36, -64, 56]	44	Right Cerebrum, Parietal Lobe, Superior Parietal Lobule, WM	0.165352	0.002929	1.000000	0.000026
[4, 18, -28]	43	Right Cerebrum	0.179231	0.003201	1.000000	0.000110
[-24, 44, -22]	41	Left Cerebrum, Frontal Lobe, Superior Frontal Gyrus	0.210499	0.003831	1.000000	0.000283
[-56, -72, 14]	40	Left Cerebrum, Occipital Lobe, Middle Temporal Gyrus, GM, BA 19	0.228049	0.004195	1.000000	0.000050
[28, -52, 54]	39	Right Cerebrum, Parietal Lobe, Precuneus, GM, BA 7	0.246983	0.004597	1.000000	0.000073
[22, -94, 12]	39	Right Cerebrum, Occipital Lobe, Middle Occipital Gyrus, WM	0.246983	0.004597	1.000000	0.000137
[48, 30, -10]	39	Right Cerebrum, Frontal Lobe, Inferior Frontal Gyrus, WM	0.246983	0.004597	1.000000	0.000083
[28, -42, -24]	35	Right Cerebellum, Anterior Lobe, Culmen, GM	0.338056	0.006687	1.000000	0.000073
[-56, 2, 42]	34	Left Cerebrum, Frontal Lobe, Middle Frontal Gyrus	0.364964	0.007359	1.000000	0.000034
[-42, -64, -6]	34	Left Cerebrum, Occipital Lobe, Sub-lobar, WM	0.364964	0.007359	1.000000	0.000155

Table 7.17: Effective connectivity parameters of the first RLS subject.

	RPP	**RTM**	**RFI**	**RFM**	**RLP**	**RAC**	**ROM**	**RTS**
RPP	-0.8434	-0.1212	-0.0177	0.0429	0.2316	1.5059	0.1639	0.0291
RTM	-0.0868	-0.4148	0.6209	-0.0659	0.1385	0.9816	-0.7887	0.0447
RFI	0.0681	-0.3163	-0.5521	-0.1068	-0.0759	0.3895	-0.0585	0.0955
RFM	-0.0416	0.2793	0.2786	0.1051	-0.0548	-0.1449	-0.1612	-0.0088
RLP	-0.1180	-0.2315	0.8982	0.1644	-0.5724	-0.1721	0.7401	-0.1252
RAC	-0.1604	-0.1654	0.3415	0.0168	0.0937	-0.4972	-0.4203	-0.0270
ROM	-0.0285	0.0670	-0.1422	-0.0161	5.6312e-04	0.2471	-1.0540	0.0325
RTS	-0.0391	-0.3477	-0.0337	0.0520	0.0613	0.2303	-0.0044	0.0438

The model could not be implemented in the second RLS patient, the white matter time-series could not be extracted!

Table 7.18: Effective connectivity parameters of the third RLS subject.

	RPP	**RTM**	**RFI**	**RFM**	**RLP**	**RAC**	**ROM**	**RTS**
RPP	-1.4335	-0.0157	0.1477	0.8049	0.5607	-0.1143	0.1249	0.1692
RTM	0.0530	-0.8569	0.1646	0.7827	0.2989	0.1445	-0.4660	-0.2999
RFI	-0.0105	0.4199	-0.8289	-0.7043	0.0607	-0.0408	0.1639	0.6506
RFM	-0.1260	-0.0382	0.2683	-0.8067	-0.1811	0.0104	-0.7336	0.1200
RLP	-0.0937	-0.4566	-0.3415	-0.3113	-0.8489	0.0880	0.6986	-0.2288
RAC	0.1118	-1.4943	-0.7576	0.0067	-0.8055	-0.9268	-0.3245	0.7819
ROM	0.0035	0.1973	0.0526	0.2653	-0.1220	-0.0204	-0.1735	0.2568
RTS	-0.0088	-0.2728	-0.1946	0.4244	0.2315	-0.2139	-0.2446	-0.8182

Table 7.19: Effective connectivity parameters of the fourth RLS subject.

	RPP	RTM	RFI	RFM	RLP	RAC	ROM	RTS
RPP	-0.9909	0.8951	0.2884	0.7600	0.6839	-0.9943	0.1522	-0.1937
RTM	0.0081	-0.1682	0.1453	0.0421	0.0877	-0.1057	-0.5163	0.4837
RFI	-0.0115	0.2699	-0.8953	-0.1755	1.3243	0.1749	-0.0136	-0.5405
RFM	0.0016	-0.1565	0.2203	-0.9802	-0.2134	-0.3757	-0.0139	0.2683
RLP	-0.1478	-0.2910	-0.1240	0.1115	-0.9238	-0.1952	0.3628	-0.0598
RAC	0.1075	-0.2290	0.1722	0.1241	0.5131	-0.5565	0.3545	0.0090
ROM	0.1217	-0.1430	0.2582	-0.1275	-0.3225	-0.7542	-0.1238	0.4885
RTS	-0.3835	-0.9354	0.5366	0.5448	-0.0192	-0.1122	0.9430	-0.7678

Table 7.20: Effective connectivity parameters of the fifth RLS subject.

	RPP	RTM	RFI	RFM	RLP	RAC	ROM	RTS
RPP	-0.7512	-0.2108	0.0360	0.2045	0.0408	-0.1123	0.9512	-0.1233
RTM	0.0597	-0.5342	-0.1015	0.0898	0.0242	-0.3396	-0.0462	-0.0438
RFI	-0.0504	1.2477	-0.9157	1.1675	-0.4785	0.2569	-0.3603	0.0569
RFM	-0.0687	-0.2472	-0.0671	-0.4377	0.0197	-0.0422	0.2112	-0.0711
RLP	0.0065	0.3467	0.1063	-0.0066	-0.6019	-0.1628	0.1666	-0.0461
RAC	-0.0428	0.8246	0.2166	0.5968	0.0457	-1.1119	0.2689	-0.0407
ROM	-0.0534	0.1705	0.0302	-0.0170	-0.0693	-0.0671	-0.8493	0.0230
RTS	5.2208e-04	0.4212	0.1861	1.1196	0.1537	-0.0192	-0.3310	-1.0116

Table 7.21: Effective connectivity parameters of the sixth RLS subject.

	RPP	RTM	RFI	RFM	RLP	RAC	ROM	RTS
RPP	-0.3308	-0.0646	0.2433	0.6211	-0.0235	0.5695	0.3054	-0.7034
RTM	0.0112	-0.9090	-0.3582	-0.0227	-0.0859	-0.1907	-0.0593	-0.0610
RFI	0.0924	0.5629	-0.2428	0.1639	0.0635	-0.2058	0.0819	0.2183
RFM	-0.0228	0.3014	-0.0512	-0.8081	0.3368	-0.0124	0.0166	0.0261
RLP	0.0566	0.1895	0.1307	-1.6986	-1.0668	0.1280	0.0833	0.3471
RAC	0.0566	0.1895	0.1307	-1.6986	-1.0688	0.1280	0.0833	0.3471
ROM	0.0168	0.5721	-0.1744	0.2752	0.0524	-0.0619	-0.8248	0.3769
RTS	0.0193	0.7913	0.2782	0.2682	0.0891	0.2777	-0.2636	-0.4675

Table 7.22: Effective connectivity parameters of the seventh RLS subject.

	RPP	RTM	RFI	RFM	RLP	RAC	ROM	RTS
RPP	-0.3497	0.0339	-0.5171	-0.0518	0.0339	-0.4264	0.4665	0.6250
RTM	0.0393	-0.1283	0.3697	-0.3057	-0.0910	-0.1587	-0.2095	0.5030
RFI	0.1060	-0.0416	-0.5332	0.4526	-0.0153	-0.3641	-0.0414	-0.3485
RFM	0.0083	-0.2047	-0.0495	-0.3680	0.0162	-0.0076	-0.0243	0.2329
RLP	0.2756	0.7878	-0.0849	-0.3693	-0.8598	-1.5066	-0.5847	0.0681
RAC	0.0295	0.4702	-0.0755	-0.5382	0.1881	-0.5137	0.1167	0.4244
ROM	-0.0699	-0.4973	0.1465	-0.2664	0.0326	0.0937	-0.6178	0.3840
RTS	0.0090	-0.0247	0.3479	-0.4711	0.0212	-0.1610	0.2203	-0.2574

Table 7.23: Effective connectivity parameters of the eighth RLS subject.

	RPP	RTM	RFI	RFM	RLP	RAC	ROM	RTS
RPP	-0.6231	0.1263	1.0902	0.0198	0.0173	-0.0257	-0.2705	1.4624
RTM	-0.031	-0.5616	-0.2165	0.0869	-0.3018	-0.0041	0.1031	0.4510
RFI	-0.2255	0.4523	-0.7706	0.0204	-0.0824	0.2567	0.0777	0.0578
RFM	0.1475	-0.1528	0.0762	-0.8907	-0.1254	0.1668	-1.2659	0.2154
RLP	0.0447	0.4273	-0.4799	0.0959	-0.7425	-0.1098	-0.2272	0.1800
RAC	-0.1114	0.0707	-1.1192	0.1186	-0.3174	-0.9549	-0.1140	0.8350
ROM	-0.0074	0.2318	0.0858	0.2478	0.0202	0.0119	-0.2664	0.2335
RTS	-0.1629	-0.0319	-0.0300	0.0903	0.1049	-0.1929	-0.1568	-0.6182

Table 7.24: Effective connectivity parameters of the ninth RLS subject.

	RPP	RTM	RFI	RFM	RLP	RAC	ROM	RTS
RPP	-0.7532	-0.4563	0.0322	0.9658	0.3285	0.0268	1.2887	-0.7428
RTM	0.0096	-0.6261	0.0685	-0.1253	0.1572	0.1637	0.0034	0.0174
RFI	0.0770	-0.6636	-0.3674	0.2553	-0.0089	-0.4841	-0.0268	-0.0525
RFM	-0.1429	-0.1655	-0.1239	-0.6444	0.1482	0.0094	-0.2815	0.0263
RLP	-0.0861	-0.6454	-0.2208	-0.2942	-0.0318	-0.0675	-0.0401	0.3354
RAC	-0.0439	-0.1730	0.0067	0.2002	0.0654	-1.1265	0.3226	-0.2129
ROM	-0.1356	-0.0180	0.1498	0.7134	0.0039	0.0786	-0.5712	-0.0536
RTS	-0.0066	0.0458	0.0305	0.6848	-0.1161	0.4154	-0.4796	-0.7613

Table 7.25: Effective connectivity parameters of the tenth RLS subject.

	RPP	RTM	RFI	RFM	RLP	RAC	ROM	RTS
RPP	-0.9953	-0.9911	0.1340	1.6205	-0.3058	0.5551	0.7328	-0.0213
RTM	0.0344	-0.8746	-0.2605	-0.0810	0.1193	-0.0544	-0.3089	0.0716
RFI	0.1629	0.4159	-0.8846	0.2008	0.1445	-0.6871	-0.3946	-0.1066
RFM	-0.2168	0.3643	-0.2845	-0.6952	0.1368	-0.2941	-0.0317	-0.0573
RLP	0.1009	0.0186	0.0116	0.0308	-0.7696	-0.9431	0.4703	-0.0298
RAC	-0.0275	-0.2110	0.2196	0.1549	0.1477	-0.5827	0.3268	0.0217
ROM	-0.1005	-0.0343	0.2366	0.1285	-0.2634	0.2216	-0.9443	0.1359
RTS	0.1536	-0.1878	0.4544	0.4782	-0.2604	0.0371	-1.3753	-0.8076

Table 7.26: Effective connectivity parameters of the eleventh RLS subject.

	RPP	RTM	RFI	RFM	RLP	RAC	ROM	RTS
RPP	-01127	0.1370	0.2909	0.2448	0.1527	0.1024	-0.4841	0.1328
RTM	0.0803	-0.3667	0.1265	-0.5104	-0.1604	-0.2192	-0.4765	-0.0579
RFI	8.1637e-04	-0.1141	8.0399e-05	-0.0789	-0.0491	0.2717	-0.2144	0.0145
RFM	-0.0752	0.0195	0.0789	-0.6867	-0.0023	-0.1199	0.7925	-0.0823
RLP	0.0611	0.3936	0.2154	-0.4093	0.0587	-0.1580	-0.3782	0.0026
RAC	0.0797	0.2278	-0.2225	0.3456	0.2470	-0.6816	1.0062	0.0118
ROM	0.0603	0.2189	0.1709	-0.4011	-0.0204	0.0073	-0.8493	-0.0497
RTS	0.0013	0.3677	0.0748	0.4654	-0.3339	0.1944	0.2377	0.0646

Table 7.27: Effective connectivity parameters of the twelfth RLS subject.

	RPP	RTM	RFI	RFM	RLP	RAC	ROM	RTS
RPP	-0.7591	-0.8787	0.0011	-0.5130	-0.1455	0.0534	0.6336	0.0480
RTM	0.0181	-0.5871	0.3319	-0.1859	-0.0891	0.1297	0.2752	0.0885
RFI	0.2116	-1.2710	-0.5746	0.1615	0.0372	0.1104	-0.5221	-0.1084
RFM	-0.0184	0.2486	0.0431	-0.6654	0.2763	0.0397	0.0081	0.2427
RLP	-0.0140	-0.3034	-0.1971	-1.1461	-0.6487	-0.7757	-0.1534	-0.0638
RAC	0.0098	-0.0023	-0.1720	0.3078	0.2134	-0.6222	-0.0855	-0.2205
ROM	0.0920	0.0951	0.1057	-0.1399	0.0715	-3.4582e-04	-1.1430	0.0110
RTS	-0.0023	0.5137	0.0420	-0.7307	0.2023	0.4620	0.2699	-0.7217

Table 7.28: Effective connectivity parameters of the thirteenth RLS subject.

	RPP	RTM	RFI	RFM	RLP	RAC	ROM	RTS
RPP	0.1216	-0.4160	-0.0983	0.5502	-0.0383	0.0360	1.4179	-0.1070
RTM	-0.1631	-0.8103	-0.2540	0.4775	0.1386	0.1858	-0.1572	-0.0399
RFI	-0.0373	1.9053	-0.4124	-0.8788	0.0894	0.4810	0.3454	-0.6581
RFM	-0.2062	-0.5521	-0.0121	-0.6569	-0.0398	-0.0256	0.8395	-0.1664
RLP	-0.0594	0.3927	0.0992	-0.1375	0.2248	-0.0850	0.1931	-0.1392
RAC	-0.6144	1.4705	0.0629	1.5083	0.3693	-0.9185	-1.2445	-0.2908
ROM	-0.5337	0.5304	0.0438	0.6179	0.0395	-0.0810	-0.5895	0.0242
RTS	-0.0098	-0.6775	-0.295	0.6795	0.3497	1.4303	-0.8323	0.0408

Table 7.29: Effective connectivity parameters of the first control subject.

	RPP	RTM	RFI	RFM	RLP	RAC	ROM	RTS
RPP	-0.3790	0.2256	-0.1879	0.2194	0.0395	-0.6065	0.2424	0.5085
RTM	0.1857	-0.6564	-0.2340	0.5045	-0.0832	-0.4886	-1.3219	0.5143
RFI	0.4575	-0.6713	-0.5032	-0.3138	-7.4120e-04	-0.1538	0.4440	-0.2013
RFM	-0.5619	0.2146	0.4596	-0.8671	-0.1719	0.2590	0.6015	-0.0579
RLP	0.0336	-0.5623	0.1199	1.2505	-0.7220	0.7525	0.6220	-0.6411
RAC	-0.0765	0.1215	-0.0346	0.1954	-0.0162	-0.6937	0.2140	0.2189
ROM	0.0987	0.2158	-0.2517	0.1050	-0.1471	-0.4265	-0.4653	0.2223
RTS	-0.0845	0.0296	0.0704	-0.1655	0.1496	-0.1093	0.8187	-0.5730

Table 7.30: Effective connectivity parameters of the second control subject.

	RPP	RTM	RFI	RFM	RLP	RAC	ROM	RTS
RPP	0.1259	0.2037	0.1262	-0.0067	0.0082	0.1281	-0.2310	0.1534
RTM	0.0252	-0.0905	0.0406	-0.3640	-0.1044	-0.5006	-0.4789	-0.1757
RFI	-0.0972	0.1688	0.2791	-0.0299	-0.0161	-0.0452	-0.5194	0.0565
RFM	0.0997	0.2462	-0.1195	0.3136	-0.0724	-0.3428	0.3759	-0.5633
RLP	0.0480	0.4635	-0.0211	-0.2212	0.5140	0.0909	-0.1982	-0.3949
RAC	0.0253	0.2452	0.2757	0.5321	-0.0906	0.0013	0.0365	0.3036
ROM	0.0588	0.5381	0.1082	-0.1957	0.1266	0.2303	-0.3675	0.0561
RTS	-0.1517	-0.2012	0.1058	0.0822	-0.0714	0.2289	-0.7083	-0.6207

Table 7.31: Effective connectivity parameters of the third control subject.

	RPP	RTM	RFI	RFM	RLP	RAC	ROM	RTS
RPP	-0.4879	0.0049	-0.2050	0.4794	0.1215	1.3462	-0.4768	0.1879
RTM	-0.0342	-0.5923	0.3383	-0.0466	-0.3108	0.1711	-0.0407	0.1439
RFI	0.0182	-0.6213	-0.2125	0.0344	0.5820	-0.2749	0.6259	-0.0026
RFM	-0.1302	-0.1580	-0.3871	-1.0767	0.0208	-0.2228	0.0471	0.0732
RLP	0.0370	0.9124	-0.1573	1.1860	-0.9344	-0.2308	0.4637	-0.1074
RAC	-0.2796	0.1656	0.2771	0.0144	0.0537	-1.1599	0.2996	-0.2073
ROM	0.0419	-0.2224	0.1662	0.1208	-0.6222	0.1761	-0.6697	-0.0590
RTS	0.0298	-1.5738	0.0044	-0.0538	-0.6225	0.6291	0.4411	-0.9906

Table 7.32: Effective connectivity parameters of the fourth control subject.

	RPP	RTM	RFI	RFM	RLP	RAC	ROM	RTS
RPP	-0.2488	-0.9964	0.1354	-0.1212	-0.0764	-0.0206	0.5697	0.1287
RTM	-0.0073	-0.9243	0.0645	0.2727	-0.0031	0.1002	-0.0759	-0.0536
RFI	-0.0159	-0.5149	-0.8334	1.0277	0.0099	-0.2954	-0.1483	0.3412
RFM	0.0057	-0.1465	-0.0919	-0.6664	-0.0477	0.1429	-0.1472	-0.2784
RLP	0.1463	-0.0406	-0.2047	0.4794	-0.5370	-1.2991	0.7726	0.3090
RAC	-0.0408	-0.5495	0.0304	0.4275	0.2638	-0.9500	0.3062	-0.1727
ROM	-0.0768	0.1380	0.1037	0.6941	-0.0608	-0.1130	-0.6144	-0.0755
RTS	-0.1575	0.3071	-0.0746	1.0528	0.1154	0.4208	0.1396	-0.7337

Table 7.33: Effective connectivity parameters of the fifth control subject.

	RPP	RTM	RFI	RFM	RLP	RAC	ROM	RTS
RPP	-0.7097	0.8360	0.2040	0.1126	0.0227	0.2613	0.2009	-0.1970
RTM	-0.0532	-0.5273	-0.4237	0.0406	-0.0575	-0.1925	0.1145	0.0671
RFI	0.0697	1.0159	-0.4490	-0.4224	0.0235	-0.1694	-0.0046	-0.3231
RFM	-0.1145	0.3273	0.1233	-1.0676	-0.0127	0.0647	-0.0842	-0.1421
RLP	0.2840	0.8917	0.0665	0.7425	-1.2870	0.2622	-2.1940	-0.3468
RAC	-0.1625	-0.6720	0.5048	0.2915	0.0558	-0.6557	-0.1749	0.6044
ROM	-0.1220	0.0173	-0.0563	0.2149	0.2246	0.1255	-0.5323	-0.0069
RTS	0.1807	-0.6812	-0.4011	0.3425	-0.0808	-0.6449	0.3529	-0.3219

Table 7.34: Effective connectivity parameters of the sixth control subject.

	RPP	RTM	RFI	RFM	RLP	RAC	ROM	RTS
RPP	-0.1232	-0.3033	0.2535	-0.0150	0.1728	-0.3373	-0.1202	0.3255
RTM	-0.0325	-0.0391	-0.0694	0.0243	-0.1226	0.1327	0.1154	0.1845
RFI	-0.0666	0.4888	-0.3853	0.0269	-0.1198	-0.3389	-0.1329	-0.2246
RFM	0.1764	-0.4688	0.1627	-1.6596	0.1529	0.5321	-2.3416	0.0267
RLP	-0.2339	1.2351	0.7344	-0.0246	-0.9792	0.7966	-0.0418	-0.0819
RAC	0.0883	-0.2078	0.3824	-0.0883	-0.2331	-1.1759	-0.0795	0.0800
ROM	-0.0133	0.1174	0.1288	0.2016	-0.0077	0.0063	-0.7824	-0.0785
RTS	-0.3921	-1.6144	-0.3992	-0.0581	-0.3028	0.2827	0.5137	-0.8600